

# TECHNISCHE UNIVERSITÄT BERLIN

Fakultät V - Verkehrs- und Maschinensysteme  
Institut für Strömungsmechanik und Technische Akustik (ISTA)  
Fachgebiet Dynamik instabiler Strömungen  
Prof. Dr.-Ing. Kilian Oberleithner

---

## MRV and PIV of the Turbulent Flow Field inside a Swirl Combustor

vorgelegt von

Kevin Harry Lausch

im Studiengang

Physikalische Ingenieurwissenschaft (Engineering Science)

Matrikelnummer: 339256

Wissenschaftliche Betreuung:

Prof. Dr.-Ing. Kilian Oberleithner	<a href="mailto:oberleithner@tu-berlin.de">oberleithner@tu-berlin.de</a>
M.Sc. Finn Lückoff	<a href="mailto:finn.lueckoff@tu-berlin.de">finn.lueckoff@tu-berlin.de</a>

Prüfer:

Erstprüfer	Prof. Dr.-Ing. Kilian Oberleithner
Zweitprüfer	M.Sc. Finn Lückoff

Berlin, den 06.10.2019

# Eidesstattliche Erklärung

Hiermit erkläre ich, dass ich die vorliegende Arbeit selbstständig und eigenhändig sowie ohne unerlaubte fremde Hilfe und ausschließlich unter Verwendung der aufgeführten Quellen und Hilfsmittel angefertigt habe.

Berlin, den 08.10.2019

---

Kevin Harry Lausch

# Zusammenfassung

Die vorliegende Arbeit beschäftigt sich mit der experimentellen Untersuchung eines Drallstrahls mittels Particle Image Velocimetry (PIV) und Magnetic Resonance Velocimetry (MRV). Drallstrahlen haben ihre technische Bedeutung insbesondere im Bereich der Gasturbinen, weil sie in einer Brennkammer flammenstabilisierend und Mischungsfördernd wirken. Aber auch abseits der Verbrennung finden sich Drallströmungen in Natur und Technik, weshalb ihnen in den letzten Jahrzehnten viel Forschungsinteresse gegolten hat. Durch die im Regelfall komplexe Geometrie eines Drallgenerators (*swirler*) sehen sich Ingenieure einer erheblichen Herausforderung gestellt, experimentell an die Geschwindigkeitsfelder aus dem Inneren des Drallgenerators zu gelangen. Selbst der übliche Einsatz von PIV in Brennkammern erfordert zumindest einen optischen Zugang und liefert in den meisten Fällen nur Geschwindigkeitsfelder in einer Schnittebene. Mit der MRV können diese Mängel zu Teilen überwunden werden.

Diese Arbeit zielt auf das Erlangen, den Vergleich und die Verwertung von gemittelten Geschwindigkeitsdaten mittels MRV und PIV, um ein vollständigeres Bild der isothermen Strömungsstrukturen zu gewinnen und die Potentiale eines selten verwendeten Messverfahrens im Bereich der turbulenten Strömungen zu beleuchten.

Ein neuer Versuchsstand zur Durchführung der MRV-Experimente wird entworfen und aufgebaut. MRV-Daten werden hauptsächlich in einer zentralen Schicht in Strömungsrichtung durch die Mittelung einer großen Anzahl an Messungen gewonnen. Gemittelte PIV-Daten aus der dazugehörigen Schicht werden für die Validierung und den Vergleich herangezogen. Drei verschiedene Strömungskonfigurationen werden unter Modifizierung der Geometrie des Drallgenerators betrachtet. Der Basisfall ist gekennzeichnet durch die unveränderte Strömung im Drallgenerator, der im Wesentlichen aus einem Mischungsrohr und acht exzentrischen Leitöffnungen zur Drallerzeugung besteht. Die erste Modifikation beinhaltet eine zusätzliche Strahleindüsung entlang der Mittellinie, wohingegen die alleinige Strahleindüsung bei verschlossenen Leitöffnungen die zweite Modifikation darstellt. Weiterhin wird eine *Proper Orthogonal Decomposition* (POD) auf die PIV-Daten des Basisfalls angewendet, während die entsprechenden MRV-Daten für eine globale *lineare Stabilitätsanalyse* (LSA) verwendet werden.

Die Ergebnisse der drei Fälle und der jeweiligen modalen Zerlegungsverfahren zeigen insgesamt eine gute Übereinstimmung für die Bereiche, in denen sowohl PIV- als auch MRV-Daten vorliegen. Außerdem zeigen die MRV-Ergebnisse, dass eine vollständige, volumetrische Erfassung des Geschwindigkeitsfeldes sowohl im Inneren des Drallgenerators als auch in der gesamten Brennkammer mit annehmbarer Detailschärfe und ausreichender Genauigkeit gelingen kann. Besonders geeignet erscheint die Flexibilität der MRV für diese Art von Untersuchungen, da in beinahe beliebigen Schnittebenen beliebige Geschwindigkeitskomponenten bestimmt werden können. Damit steht eine experimentelle Validierungsmethode für schwer erreichbare Geometrieabschnitte zur Verfügung, die sich als wertvoll in Bezug auf numerische Studien und analytische Modellansätze erweisen kann.



# Abstract

The presented work addresses the experimental investigation of a swirling jet by means of Particle Image Velocimetry (PIV) and Magnetic Resonance Velocimetry (MRV). Especially in the field of gas turbines, swirling jets are of technical importance because of their positive impacts on flame stabilization and mixing enhancement in combustion chambers. But also apart from combustion, swirling flows are found in nature and technology, which is why they have been in the focus of increased research interest throughout the past decades.

Due to the usually complex geometry of a swirl generator, or *swirler*, engineers are facing a considerable challenge in the experimental acquisition of velocity fields inside of the swirl generator. Even the common application of PIV in combustion chambers requires at least optical access and is in the majority of cases restricted to velocity fields within a sectional plane. These shortcomings can be partially overcome by the use of MRV.

This work aims at the acquisition, the comparison and the further processing of averaged velocity data by applying MRV and PIV in order to obtain a more complete picture of the isothermal flow structures and to illuminate the potentials of a rarely used measurement technique in the field of turbulent flows.

To facilitate the MRV experiments, a new test rig is designed and constructed. MRV data are primarily acquired in a central streamwise slice by averaging high numbers of measurement samples. Averaged PIV data obtained within the corresponding slice are used for validation and comparison. Three different flow configurations are investigated by modifying the geometry of the swirler. The *base case* is characterized by the unaltered flow inside of the swirler, which is basically a cylindrical mixing tube equipped with eight eccentric vanes for swirl generation. The first modification involves an additional injector jet along the centerline, whereas the sole injector jet with sealed vanes provides the second modification. Furthermore, a *Proper Orthogonal Decomposition* is applied to PIV data of the base case, while corresponding MRV data are used for a global *linear stability analysis* (LSA).

The results of the three cases and the respective modal decomposition techniques show in overall terms a good agreement in the regions where both MRV and PIV data are available. Moreover, MRV results indicate that a complete volumetric acquisition of the velocity field not only within the swirler but also within the entire combustion chamber can be achieved with acceptable resolution and sufficient precision. The flexibility of MRV acquisitions appears particularly appropriate for this type of investigations since all velocity components can be determined in almost any selected measurement slice. Considering geometry sections that are difficult to access, this feature also allows for an experimental validation technique that may prove valuable with respect to numerical studies and analytical modeling approaches.



# Contents

<b>List of Figures</b>	<b>VII</b>
<b>List of Tables</b>	<b>IX</b>
<b>Nomenclature</b>	<b>X</b>
<b>1 Introduction</b>	<b>1</b>
<b>2 Physical and Mathematical Essentials</b>	<b>3</b>
2.1 Definitions and Notation . . . . .	3
2.2 Atomic Structure of Matter . . . . .	4
2.3 Magnetism . . . . .	4
2.4 Spins, NMR and Signal Acquisition . . . . .	6
2.4.1 Spins and Magnetic Moments . . . . .	6
2.4.2 Effect of Magnetic Fields on Spin Ensembles . . . . .	8
2.4.3 Magnetic Resonance and Precession of Net Magnetization . . . . .	9
2.4.4 Signal Induction and Relaxation Times . . . . .	10
2.4.5 Signal Acquisition and Processing . . . . .	11
2.5 Fundamentals of Fluid Dynamics . . . . .	12
2.6 Flow Decomposition Based on Time Scales . . . . .	14
2.7 Proper Orthogonal Decomposition . . . . .	17
2.8 Global Linear Stability Analysis . . . . .	19
<b>3 Materials and Methods</b>	<b>22</b>
3.1 Experiment Design and Construction . . . . .	22
3.1.1 PIV Setup . . . . .	23
3.1.2 MRV Setup . . . . .	23
3.2 PIV Principle, Settings and Specifications . . . . .	25
3.2.1 PIV Principle . . . . .	25
3.2.2 PIV Settings and Specifications . . . . .	26
3.3 MRV Principle, Selected Methods and Specifications . . . . .	28
3.3.1 Signal Modification and Gradient Fields . . . . .	28
3.3.2 Spatial Encoding: Slice Selection . . . . .	29
3.3.3 The Concept of k-Space . . . . .	30
3.3.4 Spatial Encoding: Frequency Encoding . . . . .	33
3.3.5 Spatial Encoding: Phase Encoding . . . . .	34
3.3.6 Velocity Encoding . . . . .	36
3.3.7 MRV Specifications . . . . .	38
3.4 POD and LSA Specifications . . . . .	39

<b>4</b>	<b>Results</b>	<b>41</b>
4.1	Base Case: Swirling Flow without Injector Jet . . . . .	41
4.2	Swirling Flow with Injector Jet . . . . .	46
4.3	Sole injector jet . . . . .	50
4.4	Comparison of Through-Plane Velocities . . . . .	54
4.5	Comparison of Modes Obtained from POD and LSA . . . . .	56
<b>5</b>	<b>Discussion</b>	<b>58</b>
5.1	General Evaluation of the Results . . . . .	58
5.2	Limitations and Improvement Approaches . . . . .	61
5.3	Future Prospects and Potentials . . . . .	63
<b>6</b>	<b>Conclusion</b>	<b>65</b>
	<b>Bibliography</b>	<b>66</b>
	<b>Appendices</b>	<b>72</b>
<b>A</b>	<b>Technical Drawings</b>	<b>73</b>
<b>B</b>	<b>Illustrations of the Test Rigs</b>	<b>88</b>
<b>C</b>	<b>Additional MRV parameters</b>	<b>91</b>

# List of Figures

3.1	Simplified PIV principle. Adapted from <i>Optisches Geschwindigkeitsmesssystem zur vektoriellen Erfassung instationärer Strömungsprozesse</i> (p. 12), by R. Schlüßler, 2017, Dresden, Germany: Sächsische Landesbibliothek - Staats- und Universitätsbibliothek Dresden. Copyright 2017 by R. Schlüßler. Adapted with permission. . . . .	26
3.2	Simplified illustration of the gradient echo within $T_2^*$ -decay . . . . .	29
3.3	Relationship of wave numbers and level of detail using the example of cranial imaging. Reprinted from <i>Magnets, Spins, and Resonances: An introduction to the basics of Magnetic Resonance</i> (p. 118), by Siemens Healthcare GmbH, Erlangen, Germany: Siemens in-house publishing. Copyright 2015 by Siemens Healthcare GmbH. Reprinted with permission. . . . .	33
3.4	Simplified visualization of an exemplary GRE pulse sequence with a PEG rewinder and extended FEG duration. Reprinted from <i>The Essential Physics of Medical Imaging</i> (Third Edition, p. 454), by J.T. Bushberg and J.M. Boone, 2011, Philadelphia, USA: Wolters Kluwer Health. Copyright 2012 by Lippincott Williams & Wilkins. Reprinted with permission. . . . .	35
4.1	Axial velocity field comparison of the case: swirling flow without injector jet; (A) MRV, coronal plane (B) MRV, transverse plane (C) PIV, coronal plane (D)-(F) MRV and PIV velocity profiles from (A) and (C) at $\frac{x}{D} = 2.5$ , $\frac{x}{D} = 1.5$ and $\frac{x}{D} = 0.5$ . . . . .	43
4.2	Transverse velocity field comparison of the case: swirling flow without injector jet; (A) MRV, coronal plane (B) MRV, transverse plane (C) PIV, coronal plane (D)-(F) MRV and PIV velocity profiles from (A) and (C) at $\frac{x}{D} = 2.5$ , $\frac{x}{D} = 1.5$ and $\frac{x}{D} = 0.5$ . . . . .	45
4.3	Axial velocity field comparison of the case: swirling flow with injector jet; (A) MRV, coronal plane (B) MRV, transverse plane (C) PIV, coronal plane (D)-(F) MRV and PIV velocity profiles from (A) and (C) at $\frac{x}{D} = 2.5$ , $\frac{x}{D} = 1.5$ and $\frac{x}{D} = 0.5$ . . . . .	47
4.4	Transverse velocity field comparison of the case: swirling flow with injector jet; (A) MRV, coronal plane (B) MRV, transverse plane (C) PIV, coronal plane (D)-(F) MRV and PIV velocity profiles from (A) and (C) at $\frac{x}{D} = 2.5$ , $\frac{x}{D} = 1.5$ and $\frac{x}{D} = 0.5$ . . . . .	49
4.5	Axial velocity field comparison of the case: sole injector jet; (A) MRV, azimuthal average of 10 planes with differing angles of rotation $\phi$ (B) MRV, transverse plane (C) PIV, coronal plane (D)-(F) MRV and PIV velocity profiles from (A) and (C) at $\frac{x}{D} = 2.5$ , $\frac{x}{D} = 1.5$ and $\frac{x}{D} = 0.5$ . . . . .	51

4.6	Transverse velocity field comparison of the case: sole injector jet; (A) MRV, azimuthal average of 10 planes with differing angles of rotation $\phi$ (B) PIV, coronal plane (C)-(E) MRV and PIV velocity profiles from (A) and (B) at $\frac{x}{D} = 2.5$ , $\frac{x}{D} = 1.5$ and $\frac{x}{D} = 0.5$ . . . . .	53
4.7	Through-plane velocity field comparison of the cases: swirling flow without and with injector jet; (A) MRV, coronal plane, without injector jet (B) MRV, coronal plane, with injector jet . . . . .	55
4.8	POD and LSA mode comparison of the case: swirling flow without injector jet; (A) combined first two POD modes (B) mirrored global LSA mode, obtained from the azimuthal average of 12 bisected planes with differing angles of rotation $\phi$ (C) LSA eigenvalue spectrum, selected eigenvalue is highlighted in red . . . . .	57
A.1	Technical drawing of the upstream swirler component, including the frustum of a cone and the axial orifice . . . . .	74
A.2	Technical drawing of the downstream swirler component, including the eccentric vanes and the mixing tube . . . . .	75
A.3	Technical drawing of the removable, central swirler adapter for the test rig at the HFI water laboratory . . . . .	76
A.4	Technical drawing of the central socket, used for the phantom at the facilities of the PTB . . . . .	77
A.5	Technical drawing of the central mounting adapter for the test rig at the HFI water laboratory . . . . .	78
A.6	Technical drawing of the downstream pipe adapter, used for both test rigs	79
A.7	Technical drawing of the upstream pipe adapter, used for both test rigs	80
A.8	Technical drawing of the upstream transition nipple, used for both test rigs	81
A.9	Technical drawing of the upstream mounting adapter for the test rig at the HFI water laboratory . . . . .	82
A.10	Technical drawing of the downstream mounting adapter for the test rig at the HFI water laboratory . . . . .	83
A.11	Technical drawing of the downstream transition nipple, used for both test rigs . . . . .	84
A.12	Technical drawing of an exemplary axial orifice inset . . . . .	85
A.13	Technical drawing of an exemplary blocking ring . . . . .	86
A.14	Technical drawing of the removable, central pipe adapter for the test rig at the HFI water laboratory . . . . .	87
B.1	Simplified illustration of the test rig at the HFI water laboratory . . . . .	89
B.2	Simplified illustration of the test rig at the facilities of the PTB . . . . .	90

# List of Tables

3.1	Technical equipment used for the PIV experiments . . . . .	23
3.2	Technical equipment used for the MRV experiments . . . . .	24
3.3	PIV settings for the selected cases . . . . .	27
3.4	Boundary conditions of the global LSA specified for the three types <i>Symmetry axis, Inlet/Outlet</i> and <i>Walls</i> . . . . .	40
C.1	MRV acquisition parameters for the axial and transverse velocity fields of the swirling flow without injector jet . . . . .	92
C.2	MRV acquisition parameters for the axial and transverse velocity fields of the swirling flow with injector jet . . . . .	92
C.3	MRV acquisition parameters for the axial and transverse velocity fields of the sole injector jet . . . . .	93
C.4	MRV acquisition parameters for the through-plane velocity fields of the swirling flow with and without injector jet . . . . .	93
C.5	MRV acquisition parameters for the three velocity component fields used for the global LSA base flow . . . . .	94

# Nomenclature

## List of Greek Symbols

Symbol	Description	Unit
$\alpha$	flip angle	—
$\gamma$	gyromagnetic ratio	$A s kg^{-1}$
$\epsilon$	small perturbation factor	—
$\lambda$	first LAMÉ parameter	$kg m^{-1} s^{-1}$
$\mu$	dynamic viscosity	$kg m^{-1} s^{-1}$
$\mu_B$	BOHR magneton	$A m^2$
$\mu_N$	nuclear magneton	$A m^2$
$\mu_0$	vacuum permeability	$kg m A^{-2} s^{-2}$
$\boldsymbol{\mu}$	magnetic dipole moment	$A m^2$
$\boldsymbol{\mu}_N$	nuclear magnetic dipole moment	$A m^2$
$\boldsymbol{\mu}_s$	electron spin magnetic dipole moment	$A m^2$
$\nu$	kinematic viscosity	$m^2 s^{-1}$
$\nu_t$	eddy viscosity	$m^2 s^{-1}$
$\rho$	fluid density	$kg m^{-3}$
$\sigma_j$	j-th singular value	$m s^{-1}$
$\sigma_v$	velocity noise	—
$\overset{\langle 2 \rangle}{\boldsymbol{\sigma}}$	CAUCHY stress tensor	$kg m^{-1} s^{-2}$
$\boldsymbol{\tau}_N$	torque on nuclear magnetic moments	$kg m^2 s^{-2}$
$\overset{\langle 2 \rangle}{\boldsymbol{\tau}}$	REYNOLDS stress tensor	$kg m^{-1} s^{-2}$
$\overset{\langle 2 \rangle}{\hat{\boldsymbol{\tau}}}$	nondimensionalized interaction tensor	—
$\phi$	azimuthal angle	—
$\varphi$	phase accumulation	—
$\chi_v$	volume magnetic susceptibility	—
$\overset{\langle 2 \rangle}{\boldsymbol{\chi}}$	magnetic susceptibility tensor	—
$\omega$	angular frequency of coherent mode	$s^{-1}, -$
$\omega_i$	growth rate of the coherent mode	$s^{-1}, -$
$\omega_r$	eigenfrequency of the coherent mode	$s^{-1}, -$
$\omega_0$	angular LARMOR frequency	$s^{-1}$

Symbol	Description	Unit
$\Delta\omega_0$	angular frequency bandwidth	$s^{-1}$

## List of Latin Symbols

Symbol	Description	Unit
$a$	temporal coefficient of POD mode	$m s^{-1}$
$\mathbf{a}$	acceleration	$m s^{-2}$
$\alpha$	scaled temporal modes	$m s^{-1}$
$A$	atomic mass number	–
$\mathbb{A}$	left discretized linear operator	–
$\mathbf{b}$	specific body force	$m s^{-2}$
$B_0$	main field magnetic flux density norm	$kg A^{-1} s^{-2}$
$B_1$	RF-pulse magnetic flux density norm	$kg A^{-1} s^{-2}$
$\mathbf{B}$	magnetic flux density	$kg A^{-1} s^{-2}$
$\mathbf{B}_0$	main field magnetic flux density	$kg A^{-1} s^{-2}$
$\mathbf{B}_1$	RF-pulse magnetic flux density	$kg A^{-1} s^{-2}$
$\mathbb{B}$	right discretized linear operator	–
$c$	receiver coil sensitivity function	$A^{-1} m^{-2}$
$D$	mixing tube diameter	$m$
$D_c$	characteristic length	$m$
$e$	elementary charge	$A s$
$E_x$	$x$ -direction extent of imaging slice	$m$
$\Delta E_x$	$x$ -direction resolution of imaging slice	$m$
$E_y$	$y$ -direction extent of imaging slice	$m$
$\Delta E_y$	$y$ -direction resolution of imaging slice	$m$
$f_c$	characteristic linear frequency	$s^{-1}$
$f_0$	linear LARMOR frequency	$s^{-1}$
$g$	g-factor, dimensionless magnetic moment	–
$g_e$	electron spin g-factor	–
$g_N$	total nuclear spin g-factor	–
$\mathbf{g}$	gravitational acceleration	$m s^{-2}$
$G$	filter function	–
$\mathbf{G}$	$z$ -direction magnetic gradient field	$kg A^{-1} m^{-1} s^{-2}$
$\langle \mathbf{G} \rangle$	magnetic gradient field tensor	$kg A^{-1} m^{-1} s^{-2}$
$\hbar$	reduced PLANCK constant	$kg m^2 s^{-1}$
$\mathbf{H}$	magnetic field strength	$A m^{-1}$

Symbol	Description	Unit
$I$	nuclear spin angular momentum	$kg\ m^2\ s^{-1}$
$\overset{\langle 2 \rangle}{\mathbf{I}}$	identity tensor	—
$k_x$	$x$ -component of angular wave number	$m^{-1}$
$k_y$	$y$ -component of angular wave number	$m^{-1}$
$\Delta k$	angular wave number spacing	$m^{-1}$
$\mathbf{k}$	angular wave number vector	$m^{-1}$
$\overset{\langle 2 \rangle}{\mathbf{L}}$	velocity gradient tensor	$s^{-1}$
$m$	azimuthal wave number	—
$m_e$	electron rest mass	$kg$
$m_p$	proton rest mass	$kg$
$m_r$	particle rest mass	$kg$
$m_s$	magnetic spin quantum number	—
$m_0$	zeroth-order gradient moment	$kg\ A^{-1}\ m^{-1}\ s^{-1}$
$m_1$	first-order gradient moment	$kg\ A^{-1}\ m^{-1}$
$\Delta m_1$	first-order gradient moment difference	$kg\ A^{-1}\ m^{-1}$
$M_z$	longitudinal magnetization	$A\ m^{-1}$
$M_0$	longitudinal magnetization in equilibrium	$A\ m^{-1}$
$M_{\perp}$	transverse magnetization	$A\ m^{-1}$
$\mathbf{M}$	magnetization	$A\ m^{-1}$
$N$	neutron number	—
$N_m$	number of retained modes	—
$N_p$	number of spatial data points	—
$N_s$	number of samples	—
$p$	thermodynamic pressure	$kg\ m^{-1}\ s^{-1}, -$
$\bar{p}$	mean pressure	$kg\ m^{-1}\ s^{-1}$
$\hat{p}$	nondimensionalized pressure amplitude	—
$p_b$	nondimensionalized base flow pressure	—
$p'$	pressure fluctuation	$kg\ m^{-1}\ s^{-1}$
$p''$	nondimensionalized pressure perturbation	—
$q$	generalized instantaneous flow quantity	—
$\bar{q}$	generalized mean flow quantity	—
$\tilde{q}$	generalized coherent flow quantity	—
$q'$	generalized fluctuating flow quantity	—
$\hat{q}$	generalized state data vector	—
$\Delta \mathbf{r}$	PIV displacement vector	$m$
$\Re$	real part of a function	—

Symbol	Description	Unit
$Re$	REYNOLDS number	—
$Re_t$	turbulent REYNOLDS number	—
$Re^*$	effective REYNOLDS number	—
$s$	spin quantum number	—
$S$	norm of spin angular momentum	$kg\ m^2\ s^{-1}$
$S_g$	generic measurement signal	—
$S_R$	signal-to-noise ratio	—
$St$	STROUHAL number	—
$S_z$	z-projection of spin angular momentum	$kg\ m^2\ s^{-1}$
$\mathbf{S}$	spin angular momentum	$kg\ m^2\ s^{-1}$
$\mathbb{S}$	singular value data matrix	$m\ s^{-1}$
$\langle^2\rangle$		
$\bar{\mathbf{S}}$	mean rate-of-strain tensor	$s^{-1}$
$t$	time	$s$
$\Delta t$	time difference of PIV images	$s$
$t_i$	discrete point in time	$s$
$t_s$	start time, switch time	$s$
$T$	duration of process	$s$
$T_c$	period of coherent cycle	$s$
$T_1$	spin-lattice relaxation time	$s$
$T_2$	spin-spin relaxation time	$s$
$T_2^*$	effective spin-spin relaxation time	$s$
$\hat{u}$	nondim. axial velocity amplitude	—
$\mathbf{u}$	left singular vector, POD mode	—
$\mathbb{U}$	data matrix of left singular vectors	—
$\hat{v}$	nondim. radial velocity amplitude	—
$v_c$	characteristic velocity	$m\ s^{-1}$
$v_{enc}$	velocity encoding value	$m\ s^{-1}$
$v_i$	i-th velocity component	$m\ s^{-1}$
$v_0$	bulk velocity	$m\ s^{-1}$
$\mathbf{v}$	velocity	$m\ s^{-1}, -$
$\bar{\mathbf{v}}$	mean velocity	$m\ s^{-1}, -$
$\tilde{\mathbf{v}}$	nondimensionalized velocity amplitude	—
$\mathbf{v}_b$	nondimensionalized base flow velocity	—
$\mathbf{v}'$	velocity fluctuation	$m\ s^{-1}, -$
$\mathbf{v}''$	nondimensionalized velocity perturbation	—
$\mathbf{v}$	instantaneous velocity data vector	$m\ s^{-1}$

<b>Symbol</b>	<b>Description</b>	<b>Unit</b>
$\bar{v}$	mean velocity data vector	$m s^{-1}$
$\hat{w}$	nondim. azimuthal velocity amplitude	—
$w$	right singular vector	—
$W$	data matrix of right singular vectors	—
$\mathbf{x}$	spatial position	$m$
$x$	fluctuation velocity data vector	$m s^{-1}$
$X$	fluctuation velocity data matrix	$m s^{-1}$
$\Delta z$	slice thickness	$m$
$Z$	atomic number	—

## List of Acronyms

CCC	combustion chamber confinements
CRZ	central recirculation zone
FEG	frequency-encoding gradient
FFT	fast FOURIER transform
FID	free induction decay
FOV	field of view
FVE	FOURIER velocity encoding
GEVP	generalized eigenvalue problem
GRE	gradient echo
HFI	HERMANN-FÖTTINGER-INSTITUT
LSA	linear stability analysis
Nd:YAG	neodymium-doped yttrium aluminum garnet
NMR	nuclear magnetic resonance
NSE	NAVIER-STOKES equations
MRI	magnetic resonance imaging
MRV	magnetic resonance velocimetry
ORZ	outer recirculation zone
PA6	polyamide 6
PEG	phase-encoding gradient
PC	phase-contrast
PIV	particle image velocimetry
PMMA	polymethyl methacrylate
POD	proper orthogonal decomposition
PTB	PHYSIKALISCH-TECHNISCHE BUNDESANSTALT
PVC	polyvinyl chloride
RANS	REYNOLDS-averaged NAVIER-STOKES
RF	radiofrequency
ROI	region of interest
RST	REYNOLDS stress tensor
sCMOS	scientific complementary metal-oxide semiconductor
SNR	signal-to-noise ratio
SSG	slice selection gradient
SVD	singular value decomposition
TA	acquisition time
TE	echo time
TR	repetition time

# 1 Introduction

Swirling flows account for a vast number of phenomena both in nature and technical applications. One may be acquainted with swirl near bath tub drains, with dust devils and maelstroms or with large-scale meteorologic flow patterns in the atmosphere. Moreover, swirling, or helical, flow is of special interest in the examination of cardiovascular blood flow. The complex hemodynamic features in the ascending and descending aorta cause swirl whose direction and intensity could support the assessment whether the flow is physiological or pathological (Lorenz et al. [2014], Morbiducci et al. [2009], Liu et al. [2010]).

Technical applications include swirl diffusers in ventilation systems or swirl generators for combustion purposes. The latter have been studied in order to stabilize flames and enhance turbulent mixing since the 1960s (see e.g. Drake and Hubbard [1966], Robertson [1966], Morton [1968]). A few years later, BEÉR and CHIGIER devoted a whole chapter to swirling flows, whereas SYRED and BEÉR published an early yet comprehensive review (Beér and Chigier [1972], Syred and Beér [1974]). Since then advancing research on the mechanisms of mixing enhancement and flow stability has been leading to a more complete description of swirling jet flows, making it a widely studied case in fluid dynamics.

The flow studied in this thesis is generated by a swirler, which consists of a cylindrical mixing tube, eccentric vanes that induce tangential velocities and an axial orifice at the upstream end of the swirler. The choice of exchangeable orifice insets and blocking rings outside of the vanes modifies the swirl intensity.

Having reached a critical threshold, high swirl intensity causes a conversion of the flow regime. The tangential velocity distribution induces a radial pressure gradient in the swirling flow. Due to the expansion at the combustion chamber inlet, the jet diameter increases along the axial direction, leading to an axial decay of tangential velocities within the jet. This decay corresponds to an axially decreasing radial pressure gradient, which results in a negative axial pressure gradient in the vicinity of the axis (Syred [2006]). Eventually, fluid is transported from downstream to upstream regions close to the jet core. The reversed flow forms a *central recirculation zone* (CRZ). This phenomenon is known as *vortex breakdown* and closely related to instability mechanisms, which may dominate the flow in the near-field. In certain cases a *precessing vortex core* can be detected that potentially causes strong couplings between the flow dynamics, combustion and acoustics (Syred [2006]). The precessing vortex core appears as the *wavemaker* of a global mode, oscillating at a distinct frequency. Stability and control of this global mode continue to be a key subject of research.

The first substantial challenge in gaining insight in the underlying mechanisms is the acquisition of flow data that sufficiently depict the full region of interest (ROI) including complex geometries such as the inside of the swirl generator. *Magnetic Resonance Velocimetry* (MRV), also known as *4D-Flow Magnetic Resonance Imaging* (4D-Flow

## 1 Introduction

MRI) when temporal resolution is included, is capable of obtaining three-dimensional velocity vector fields without optical access or disturbing the flow and can be a promising approach to obtain the necessary data. The major drawback, apart from the availability and the price of MR systems, lies in the poor temporal resolution, since a single velocity encoded image takes several tenths of a second up to a few seconds, which is far beyond the turbulent time scales usually aimed at. Additionally, these images cannot be considered as proper snapshots due to their long acquisition periods. Therefore, mean velocity fields, constructed out of multiple MR images, appear to be applicable.

MRV studies of engineering flows have been conducted throughout the last three decades. A comprehensive overview of the first two, which covers the measurement principle, various applied methods and the different fields of application, can be found in Elkins and Alley [2007]. Since then, the developments in the different fields have been manifold. Studies that are particularly worth mentioning in the context of the given topic were conducted, for example, by GRUNDMANN et al. (Grundmann et al. [2012]), who investigated the flow within a generic swirl tube, and by WASSERMANN et al. (Wassermann et al. [2013]), who conducted phase-locked MRV experiments in a fluidic oscillator. The latter also used multiple measurements to acquire mean velocity fields for selected configurations. Furthermore, the work of FREUDENHAMMER shall be mentioned, which covered stationary, instationary but periodic and turbulent flow measurements for different application cases. Turbulent flow was investigated around a *backward facing step* and included the determination of REYNOLDS stresses on the basis of multiple acquisitions (Freudenhammer [2017]).

Nevertheless, MRV of turbulent flows is still rather uncommon, which is why this thesis primarily focuses on the applicability of this technique. For this purpose two test rigs have been constructed: firstly, at the water laboratory of the HERMANN-FÖTTINGER-INSTITUT (HFI) and secondly, at the facilities of the PHYSIKALISCH-TECHNISCHE BUNDESANSTALT BERLIN (PTB Berlin). In order to assess and compare the results, analogous mean fields are measured using *Particle Image Velocimetry* (PIV) and MRV. These mean fields are used on one hand for a *Proper Orthogonal Decomposition* (POD, for PIV data) and for a global *linear stability analysis* (LSA, for MRV data) on the other hand. Aside from the quantitative comparison of velocity profiles, the modes obtained from these decomposition techniques serve as adequate indicators of the applicability and reliability of turbulent flow measurements using MR techniques.

The thesis is structured as follows: At first, the physical and mathematical essentials of *nuclear magnetic resonance* (NMR) and of the applied data analysis techniques are explained in chapter 2. Following this, a description of the measurement setups, principles and specifications is given. The fourth chapter addresses the results of the MRV and PIV experiments for different swirler configurations in a comparative manner, which also involves the results of the applied modal decomposition techniques. At last, the results are discussed and evaluated with respect to measurement limitations and further potentials.

## 2 Physical and Mathematical Essentials

In order to clarify the underlying concepts used throughout the thesis, this chapter shall introduce and refresh the basic physics and crucial mathematical methods.

At first, a few remarks on notation and general definitions are given. Thereafter, a brief summary on the atomic structure of matter, magnetism, spins and especially NMR provides the basis for the understanding of MRI. Subsequently, fundamental fluid dynamics are covered with a particular focus on temporal decomposition techniques and on applied methods from modal analysis.

### 2.1 Definitions and Notation

In the following, a scalar (field), a number or a constant are all represented by standard Greek or Roman letters. This also applies for vector or tensor components. A vector or pseudovector (field) is represented by bold letters, second-order tensor fields are indicated by bold letters with a  $\langle 2 \rangle$  positioned above the variable.

Data vectors and matrices are emphasized as bold with a special font. Data vectors are given by Roman lower case letters, data matrices by Roman upper case letters, e.g.  $\boldsymbol{x}$  and  $\boldsymbol{X}$ , respectively.

Contractions are indicated by a dot, while multiplications with scalars lack any symbol. The outer product is expressed using  $\otimes$ . Consequently, the gradient of the velocity vector field  $\boldsymbol{v}$  is given by  $\text{grad } \boldsymbol{v} = \boldsymbol{v} \otimes \boldsymbol{\nabla}$ , i.e. the gradient shall act from the right. EINSTEIN summation convention is used, however, there will be no distinction between co- and contravariant indices such that only subscripts are used as indices, e.g.  $v_i$ .

Thereby, the gradient of  $\boldsymbol{v}$ ,  $\overset{\langle 2 \rangle}{\boldsymbol{L}}$ , could be expressed as:

$$\text{grad } \boldsymbol{v} = \overset{\langle 2 \rangle}{\boldsymbol{L}} = L_{ij} \boldsymbol{e}_i \otimes \boldsymbol{e}_j = \frac{\partial v_i}{\partial x_j} \boldsymbol{e}_i \otimes \boldsymbol{e}_j = v_{i,j} \boldsymbol{e}_i \otimes \boldsymbol{e}_j. \quad (2.1)$$

According to the similar setup in the two experiments a global, right-handed Cartesian coordinate system is defined where the basis vector at the origin  $\boldsymbol{e}_x$  points axially from upstream to downstream,  $\boldsymbol{e}_y$  radially from the origin to the right of the view plane and  $\boldsymbol{e}_z$  results as the through-plane orthogonal basis vector. Moreover, a cylindrical coordinate system  $(\rho, \phi, x)$  is defined where  $\boldsymbol{e}_\rho = \boldsymbol{e}_y$ ,  $\boldsymbol{e}_\phi = \boldsymbol{e}_z$  and  $\boldsymbol{e}_x = \boldsymbol{e}_x$  holds at the origin. The origin is the center of the inflow plane of the combustion chamber. The azimuthal angle  $\phi$  is defined counterclockwise.

The velocity components  $u$ ,  $v$  and  $w$  correspond to  $x$ ,  $y$  and  $z$  or  $x$ ,  $\rho$  and  $\phi$ , respectively.

## 2.2 Atomic Structure of Matter

Matter was long believed to consist of elementary components, the atoms, where the Greek word *ατομος* already implies their indivisibility. When THOMSON discovered the electron in 1897, this concept quickly crumbled, leading him to his plum pudding model (1904). BOHR and RUTHERFORD further developed the early ideas to their model (1913), which is now obligatory part of physics for school students, although suffering from several shortcomings with respect to the more accurate atomic orbital model.

Still, the modern concept assumes a *nucleus*, constituted out of (electrically) positively charged protons and uncharged neutrons (summarized as nucleons), surrounded by negatively charged electrons. The electrons are bound to orbitals, which may be imagined as a cloud or atmosphere, equipped with a probability density to be located at a certain position inside their respective clouds.

Two electrons may share a single atomic orbital, but following the PAULI exclusion principle they cannot share the exact same set of *quantum numbers*. In case two electrons occupy the same orbital, three of four quantum numbers are already equal. Therefore they must differ in the last one, which is the *spin quantum number*.

This principle, that one quantum state cannot be occupied by two identical particles simultaneously, can be generalized to all *fermions*, i.e. particles with *half-integer spin* such as electrons. These particles do not necessarily need to be elementary like electrons or quarks but can be composite (*baryons*) as it is for the nucleons, which are composed of three quarks.

In fact, even the quantum state of the combined nucleons, namely the nucleus, can be considered, although the set of applied quantum numbers markedly alters. For now, the question of what *spins* really are should be answered with an abstract perception of intrinsic quantum mechanical properties of matter. To enhance understanding, the topic will be revisited in section 2.4, taking into account the electromagnetic interactions and mathematical particularities.

## 2.3 Magnetism

Magnetism originates from the movement of electrical charges and the intrinsic *spin magnetic moments* of elementary particles. Both causes induce a magnetic field that interacts with external electrical currents and magnetic moments by exerting a force, which can be measured. This coupled *electromagnetic force* is one of the four fundamental interactions of nature and requires relativistic and quantum theoretical approaches to be completely explained.

Nevertheless, considering the simplified model of the atomic structure that involves orbiting electrons and spin-carrying particles, still leads to the implication that all materials may give rise to a magnetic field. On macroscopic scales, however, the resulting fields often vanish as the orbital and spin magnetic moments cancel out for different reasons. At first, one should consider that the magnetic moment of atoms is largely due to the electrons' contribution. This contribution only exists when there are *unpaired* electrons since pairs tend to occupy states with opposite magnetic orientation. Moreover,

the unpaired electrons produce magnetic moments with random orientations such that the net magnetic moment of most macroscopic materials is close to zero.

The explanation for the magnetic dipole moments of orbiting electrons can, to some extent, be transferred to the substantially weaker *nuclear magnetic moment*. Conceptually, the nuclear magnetic moment is referred to the nuclear spin in correspondence with the electron spin and its magnetic moment. This implies that a single nucleus has no exact equivalent to the electron orbital momentum. Rather the nuclear magnetic moment is the *total magnetic moment* of all nucleons, which in turn can possess an orbital magnetic moment in the reference frame of the nucleus.

All the aforementioned magnetic moments cooperatively contribute to the macroscopic magnetic properties of matter in an *external magnetic field*. That field can again be induced by electric currents, is denoted by  $\mathbf{H}$  and called *magnetic field strength*. In the presence of matter the magnetic field strength may change as the material is magnetized. To distinguish the fields inside the material, the *magnetization*  $\mathbf{M}$  and *magnetic flux density*  $\mathbf{B}$  are defined such that

$$\mathbf{B} = \mu_0(\mathbf{H} + \mathbf{M}), \quad (2.2)$$

where  $\mu_0$  is the *vacuum permeability*. Often,  $\mathbf{M}$  can be linearly expressed in terms of  $\mathbf{H}$  via

$$\mathbf{M} = \overset{\langle 2 \rangle}{\chi} \cdot \mathbf{H}, \quad (2.3)$$

where  $\overset{\langle 2 \rangle}{\chi}$  is the *magnetic susceptibility tensor* or, in the case of magnetic isotropy, via

$$\mathbf{M} = \chi_v \mathbf{H}, \quad (2.4)$$

where  $\chi_v$  is the *volume magnetic susceptibility*.

The simplified interpretation of the value of susceptibility is that in case  $\chi_v > 0$ , the magnetic flux density is amplified within the material, which means that the material is attracted by the magnetic field. This property is called *paramagnetism* and bases on a preferentially parallel, but still non-ordered, alignment of magnetic moments of atoms and molecules that constitute the microscopic structure. *Ferromagnetism* is the enhanced variant of paramagnetism with an additional spontaneous magnetization inside of small *magnetic domains*, where multiple magnetic moments align in an ordered manner.

In case  $\chi_v < 0$ , the magnetic field is repelled and the magnetic flux density is depleted within the material. This behavior is called *diamagnetism* and corresponds to an induced magnetic field inside the atomic structures that is opposed to its cause. Diamagnetism is the most common manifestation of magnetism as it occurs in all materials. However, the effects are usually either in orders of size that can be neglected or superposed by paramagnetic or ferromagnetic effects.

Susceptibility is of considerable interest in NMR applications because of its effect on the magnetic field's homogeneity (and its utilization in susceptibility-weighted imaging). The most unfavorable side effect of susceptibility is that the magnetic field undergoes distortion in the vicinity of material interfaces because these distortions come with a measurement inaccuracy.

An important feature to notice is that the magnetic moment arising from spins is often referred to as magnetic dipole moment. This is because higher order moments are commonly neglected in the expansion and there is no reliable evidence for the existence of magnetic monopoles in spite of a long-lasting search for the sake of symmetry in MAXWELL's equations. This implies that, for now, the magnetic dipole is the simplest origin of magnetism, which is why magnetic dipole moments corresponding to spins are often illustrated with tiny bar magnets. Both spins and bar magnets are irreducible, but apart from this common feature, the analogy reveals certain weaknesses as the following considerations of spins' distinctive features will show.

## 2.4 Spins, NMR and Signal Acquisition

At first, let us recall that spin is an intrinsic property of particles like electric charge or color charge (in quarks and gluons). The frequently used model to visualize spin is that of a rotating ball equipped with a vector arrow and resulting angular momentum. In fact, there is no actual rotating movement of spin-carrying particles. Electrons, for example, can be imagined as point particles, which is why any rotation would be ill-defined. Therefore, it seems reasonable to take a closer look at the property spin and its effects.

### 2.4.1 Spins and Magnetic Moments

When referring to spin in practice, one typically addresses the spin quantum number  $s$ . In the case of a nucleon or electron ( $s = \frac{1}{2}$ ), the quantized spin angular momentum  $S$  can be computed as

$$S = \sqrt{s(s+1)} \hbar = \frac{\sqrt{3}}{2} \hbar, \quad (2.5)$$

where  $\hbar$  is the reduced PLANCK constant (cf. Brown et al. [2014]). Here  $S = \|\mathbf{S}\|$  denotes the norm of the identically named spin angular momentum  $\mathbf{S}$ , which is a vector-like quantity. Although it has a magnitude and direction, the spin angular momentum is not a proper vector, because of its behavior under coordinate rotations, which is unfamiliar from a classical perspective. In simple words, rotating the reference system by  $360^\circ$  leads to a change in sign, i.e. a reversed orientation, while retaining the magnitude. In order to regain the initial state, a  $720^\circ$  rotation must be performed. A two-component element of a complex vector space showing this transformation behavior is called *spinor*. For simplicity, spinors are treated like vectors in the following chapters. An appropriate starting point to gain insight into the subject of spinors may be found in Pauli [1927] or Gori et al. [1999].

Regardless of the special underlying mathematical concept, projections can be defined on spin angular momenta. By convention, the axis, along which the quantum mechanical measurement is performed, is the  $z$ -axis. Thus, the projected spin  $S_z$  can be written as (see Brown et al. [2014])

$$S_z = m_s \hbar, \quad (2.6)$$

where  $m_s$  is the *secondary* or *magnetic spin quantum number* and holds  $m_s = \pm\frac{1}{2}$  in the case of nucleons and electrons.

Starting from the electron's spin angular momentum, the connection to magnetic moments can be drawn. For a DIRAC particle, a charged, elementary spin- $\frac{1}{2}$  particle, the spin magnetic (dipole) moment  $\boldsymbol{\mu}$  is given by

$$\boldsymbol{\mu} = \frac{g e}{2m_r} \mathbf{S}, \quad (2.7)$$

where  $g$  is the particle- and angular-momentum-specific *g-factor* or *dimensionless magnetic moment*,  $e$  is the elementary charge of the particle and  $m_r$  is the particle's rest mass. In the case of the electron spin, this leads to the equation

$$\boldsymbol{\mu}_s = \frac{g_e e}{2m_e} \mathbf{S} = \frac{g_e \mu_B}{\hbar} \mathbf{S}, \quad (2.8)$$

where  $\boldsymbol{\mu}_s$  denotes the magnetic moment resulting from the electron spin,  $g_e$  the electron spin g-factor,  $m_e$  the electron rest mass and  $\mu_B$  the BOHR *magneton*, respectively. In correspondence with the electron spin and its magnetic moment, the nuclear magnetic moment  $\boldsymbol{\mu}_N$ , depending on the *nuclear spin*  $\mathbf{I}$ , is defined via

$$\boldsymbol{\mu}_N = \frac{g_N e}{2m_p} \mathbf{I} = \frac{g_N \mu_N}{\hbar} \mathbf{I}, \quad (2.9)$$

where  $g_N$  is the (total) nuclear spin g-factor,  $\mu_N$  is the *nuclear magneton* and  $m_p$  is the proton rest mass. The three constants on the right-hand side are usually combined to the *gyromagnetic ratio*  $\gamma$  such that

$$\boldsymbol{\mu}_N = \gamma \mathbf{I}. \quad (2.10)$$

The gyromagnetic ratio is an important value in NMR applications. In general,  $\gamma$  is a particle- or nucleus-specific constant that relates angular momentum to magnetic moment.

Note at this point that the nucleus is essentially not a DIRAC particle, and the original equation 2.7 does not apply. Consequently, the reference mass for nuclei has to be modified to the proton rest mass, whereas nuclear spin and g-factor depend on all nucleons. For a specific nucleus the resulting nuclear magnetic moment is typically expressed in units of nuclear magnetons. But not all nuclei present magnetic moments. Paralleling the orbital model of electrons, the *nuclear shell model* partially explains and predicts the pairing of nucleons and the cancelling of their spin contributions. Nuclei with an odd *atomic mass number*  $A$  exhibit a nuclear magnetic moment because of an unpaired nucleon. That is, nuclei with either an odd number of protons (atomic number or proton number  $Z$ ) and an even number of neutrons (neutron number  $N$ ) or odd  $N$  and even  $Z$  always show magnetic moments. This also applies to *odd-odd nuclides* with an even mass number, although the prediction of the resulting nuclear magnetic moment is more complicated in this case.

The most important nuclide for MRI purposes is hydrogen,  $^1\text{H}$ , where the nucleus is basically a single proton. Hydrogen's particular importance for MRI is essentially due to its abundance in human tissue, water or fat, as MRI is a predominantly medical

application. Moreover,  $^1\text{H}$  is the biologically relevant nuclide with the largest nuclear magnetic moment (Bushberg and Boone [2011]). A single proton's magnetic moment, however, is too weak to be detected. It is the enormous number of hydrogen atoms in a typical measurement volume (approx.  $6.7 \cdot 10^{19}$  protons in  $1 \text{ mm}^3$ ) that allows for detection.

### 2.4.2 Effect of Magnetic Fields on Spin Ensembles

In order to detect the numerous, randomly orientated nuclear magnetic moments, they must be aligned first to obtain a *net magnetization*. This is achieved by applying a strong magnetic field,  $\mathbf{B}_0$ , on the *spin ensemble* inside the measurement probe. Again by convention, the direction of the applied field is denoted as the  $z$ -direction in a Cartesian coordinate system. The spin ensemble tends to align with the lines of the magnetic field, offering the two possible directions of parallel and anti-parallel alignment for each spin. The two possibilities are accounted for by the *energy splitting* of the quantum states (ZEEMAN effect) in the presence of a magnetic field. The quantum states are referred to as *spin parallel* and *spin anti-parallel*, with the parallel alignment providing a slightly lower energetic state. Therefore, a small excess of parallelly oriented spins occurs following the BOLTZMANN distribution. Given a magnetic flux density of 1 T, physiological temperatures and a thermal equilibrium, the excess would be as small as 3 ppm spins on average (Bushberg and Boone [2011]).

Some additional comments on spins in magnetic fields shall be noted. Firstly, the individual spins do not actually align with the magnetic field lines. Since spin is a form of angular momentum, which has to be conserved, the spins start a precessing motion about the  $z$ -axis instead, thereby evading the torque of the external magnetic field, while some spins change their orientation in favor of the lower energy state. This motion is where the analogy of the tiny bar magnet needs to fail as the classical compass needle without angular momentum would indeed align with the lines of the magnetic field.

Secondly, the projection of a spin ensemble's magnetic moment on the  $z$ -axis has a certain *expectation value* that corresponds to the (paramagnetic) net magnetization's magnitude, although there is no typical alignment. Up to now, there is no *transverse magnetization* since the precessing spins point in randomly distributed directions, i.e. they are not in phase.

Thirdly, the magnetic field affects all spin-carrying particles. Aside from that, the spins and their magnetic moments interact with each other and respond to the magnetic field. For simplicity, these effects are neglected in the given explanations, but spin interactions are revisited in the context of signal decay at the end of this section.

At last, it should be mentioned that, rather than being in a parallel or anti-parallel alignment, the spin state can be generally considered as a superposition of these two orientations. Moreover, the spins inside the external field may spontaneously change orientation from parallel to anti-parallel and vice versa. The fact of the matter is that the excess, which leads to a net magnetization, remains the same.

Precession is provoked, as mentioned before, by the magnetic field  $\mathbf{B}_0$  that exerts force

on the magnetic moments  $\boldsymbol{\mu}_N$  of the nuclear spins, which causes a torque  $\boldsymbol{\tau}_N$

$$\boldsymbol{\tau}_N = \boldsymbol{\mu}_N \times \mathbf{B}_0. \quad (2.11)$$

The precession frequency is referred to as (angular) LARMOR *frequency*,  $\omega_0$ , and linearly depends on the magnetic field strength along the axis of precession  $B_0 = \|\mathbf{B}_0\|$ . The proportionality constant is given by the gyromagnetic ratio of the nucleus  $\gamma$

$$\omega_0 = \gamma B_0. \quad (2.12)$$

Note that some authors use a slightly different definition following

$$f_0 = \frac{\gamma}{2\pi} B_0, \quad (2.13)$$

where  $f_0$  is the linear LARMOR frequency and  $\frac{\gamma}{2\pi}$  is defined as the gyromagnetic ratio (see e.g. Bernstein et al. [2004], Bushberg and Boone [2011]).

Recall that the principal interest lies in the net magnetization because the signal of a single spin is too weak to be detected. The net magnetization can be calculated as the expectation value of *spin operators* on an ensemble, e.g. within a volume element (*voxel*). Given a homogeneous, static external field, transverse net magnetization cancels out, while longitudinal magnetization  $M_z$  occurs along the static field direction in an energy equilibrium.

### 2.4.3 Magnetic Resonance and Precession of Net Magnetization

In order to detect a signal, one must interfere with the equilibrium state and move the net magnetization such that an effective transverse magnetization arises, which is followed up by a precessing motion due to the influence of the static field. This can be achieved by applying a radiofrequency pulse (RF pulse) whose frequency coincides with the LARMOR frequency. The pulse can be considered as a magnetic field  $\mathbf{B}_1$  perpendicular to the main magnetic field, where  $\mathbf{B}_1$  rotates with the angular frequency  $\omega_0$  in the  $xy$ -plane. Such a field can be decomposed into a co- and a counter-rotating wave component, of which only the co-rotating component affects the orientation of the net magnetization. Modern scanner systems usually generate *circularly polarized*  $\mathbf{B}_1$  fields by applying multiple, phase-shifted and circularly distributed *RF transmitter coils* such that the counter-rotating component cancels out due to superposition (see Brown et al. [2014], Vlaardingerbroek et al. [2013]). Observed from the rotating reference system of the precessing spins, the remaining co-rotating field  $\mathbf{B}_1$  appears static, causing a precessing motion of the entire net magnetization about the field's axis as described before for the case of the individual spins in the main magnetic field. In consequence, the net magnetization is tilted towards one side, yielding a transverse magnetization  $M_\perp$ .

This is the essence of *magnetic resonance*. The RF pulse interferes resonantly with the spin ensemble by transmitting energy and moving the net magnetization out of its energy equilibrium. The *flip angle*  $\alpha$  depends on the duration  $T$  of the net magnetization's

precessing motion and the magnitude of the co-rotating field  $B_1$  according to the equation

$$\alpha = \gamma \int_0^T B_1(\tau) d\tau, \quad (2.14)$$

where  $\tau$  is the time variable of the process.

#### 2.4.4 Signal Induction and Relaxation Times

At the end of the RF pulse, the net magnetization precesses about the static main field direction again. The time-dependent change of magnetic flux density thereby induces a current in the surrounding *receiver coils*, which can be the transmitter coils as well. This current, or rather the corresponding voltage, is the source of the measurement signal. Due to the non-equilibrium state of the net magnetization, this signal rapidly decays. The effect is known as *free induction decay* (FID) and serves as a basic MR-measurement principle. The decay corresponds to a loss in transverse magnetization while the system returns to its equilibrium and it is characterized by a time constant  $T_2$ , the *spin-spin* or *transverse relaxation time*. Spin-spin relaxation relies on local magnetic field inhomogeneities caused by the BROWNIAN motion of particles. The inhomogeneities are equivalent to a locally varying magnetic flux density, which affects the locally effective LARMOR frequency and thus leads to a dephasing of the spins in an ensemble that has been statistically phase-coherent at the end of the RF pulse. The envelope of (idealized) magnetization loss after a  $90^\circ$  pulse can be modelled as an exponential decay following

$$M_\perp(\tau) = M_\perp(0) e^{\frac{-\tau}{T_2}}. \quad (2.15)$$

That is, the transverse magnetization decreases approximately 63% within the first  $T_2$ -time unit.

Obviously, there should be another time constant  $T_1$  for the sake of reasonable numbering. It represents the *longitudinal* or *spin-lattice relaxation time* and characterizes the recovery time of longitudinal magnetization, which is independent of the transverse magnetization's decay. The process of recovery is quite different from the spin-spin relaxation. At first, one should imagine the *lattice* as the molecular environment of nuclei in an ensemble, which is capable of storing energy of the ensemble's components. The spin components that left the energetically favorable state due to the RF pulse tend to return to the equilibrium state by transferring energy to nearby atoms and molecules. This is in contrast to the aforementioned spin-spin interactions, where energy is not necessarily transferred in the course of relaxation (Currie et al. [2013]). This transfer of energy needs to proceed on a stimulated basis, e.g. in the presence of a field fluctuating in resonance. The effect is comparable to the RF excitation flip but is restricted to a local scale and caused by the fluctuating field generated by dipole moments of particles. Having passed their energy, the spins return to their initial equilibrium with a small excess in the expectation value of parallelly orientated states. The longitudinal relaxation can be modelled by the equation

$$M_z(\tau) = M_0 - (M_0 - M_z(0)) e^{\frac{-\tau}{T_1}}, \quad (2.16)$$

where  $M_0$  is the longitudinal magnetization before applying the RF pulse (see Brown et al. [2014]). Thus, the longitudinal magnetization recovers to approximately 63% within the first  $T_1$ -time unit. Typically, the longitudinal relaxation times of a material are considerably longer than the transverse relaxation times. This especially holds true when the external inhomogeneities are taken into account. Those can be a consequence of imperfections in the main magnetic field generated by the coils or result from susceptibility variations in the probe that distort the magnetic field lines. In such cases, the decay of transverse magnetization proceeds more rapidly, thereby reducing  $T_2$ . The diminished time constant is then denoted  $T_2^*$ .

It is worth noting that the energy transfer of longitudinal relaxation also affects  $T_2$  because the spins receiving energy lose their phase-coherence. Therefore, transverse relaxation can be interpreted as not strictly free of energy transfer and weakly coupled to the longitudinal relaxation.

The time-dependent evolution of magnetization and relaxation processes can be summarized by the phenomenologically derived BLOCH equations that link the time derivatives of the magnetization components to the exerted torque and to the aforementioned relaxation times  $T_1$  and  $T_2$ . However, BLOCH's original denotation differs from that of modern textbooks, which is adapted here, in that, for example, the magnetic field strength  $\mathbf{H}$  is used instead of  $\mathbf{B}$  (see Bloch [1946]). Maintaining consistent notation, the equations of the magnetization components in a stationary laboratory system would read

$$\dot{M}_x = \gamma (M_y B_z - M_z B_y) + \frac{1}{T_2} M_x, \quad (2.17)$$

$$\dot{M}_y = \gamma (M_z B_x - M_x B_z) + \frac{1}{T_2} M_y, \quad (2.18)$$

$$\dot{M}_z = \gamma (M_x B_y - M_y B_x) + \frac{1}{T_1} (M_0 - M_z). \quad (2.19)$$

Note that the components of  $\mathbf{M}$  and  $\mathbf{B}$  are generally dependent on time and location, which will prove to be of crucial importance under the aspect of *spatial encoding* in section 3.3.

### 2.4.5 Signal Acquisition and Processing

The transverse magnetization induces the signal in the coils, which can be used for imaging purposes. In fact, the pulse generation and signal processing within the coils is significantly more complex than depicted before and exceeds the scope of this thesis. The interested reader may be referred to Fukushima and Roeder [1981] or Brown et al. [2014]. Nevertheless, a few technical remarks can help to point out illustrative features of the mode of operation.

To begin with, the RF excitation cannot be applied as a single-frequency pulse, but rather takes the form of a distribution with a certain bandwidth  $\Delta\omega_0$  around  $\omega_0$ . Since the precession frequency depends linearly on the main field magnetic flux density, which in turn is inhomogeneous for various reasons, the precession frequency varies locally. Therefore, irradiating the spin ensembles in resonance has to account for these small

variations. This approach is also especially expedient in tackling spatial encoding. Furthermore, the typical LARMOR frequency is in the range of hundreds of megahertz for the most common MR systems. Given a magnetic flux density of 3 T and  $^1\text{H}$  as the element of interest, the frequency would amount to  $\omega_0 \approx 127.74$  MHz (Bushberg and Boone [2011]). Sampling precise data at these frequencies—or rather at least at twice these frequencies following the NYQUIST-SHANNON sampling theorem—is hardly feasible, which is why the measurement signal is demodulated with the LARMOR frequency such that the difference frequency is close to zero for an ideally homogeneous magnetic field. However, in order to account for the frequency range induced by *gradient fields* a sampling rate of several kHz is customary.

The coils applied in clinical use are chosen to match the requirements of the examination performed. *Body coils* are the built-in coils for practically all general applications. Specifically designed *volume* or *surface coils* are used to produce volumetrically homogeneous fields or high signal-to-noise ratios (SNR) close to the surface, respectively. Volume coils often come in a *birdcage* design and may serve as both transmitter and receiver, while surface coils commonly serve as a sole receiver system (Bushberg and Boone [2011]).

At last, scanner systems with circularly polarized RF pulses mostly also use *quadrature* as a means to enhance SNR. That is, two coils independently detect signals of an identical field but phase-shifted by  $90^\circ$ . The two outputs of a certain point in time are assigned to a real and an imaginary part of a complex measurement value, whose *magnitude* and *phase* can thereafter be computed. The magnitude data show an enhanced SNR due to uncorrelated white noise in the two measurements, the phase data will be of special interest for flow measurements.

Based on the physical principles of signal generation and acquisition outlined up to this point, the methodical procedure of the conducted MR measurements will be thoroughly addressed in section 3.3. In particular, the process of spatial encoding and obtaining flow information from phase data will be explained in the context of measurement techniques deployed throughout the experiments. In order to systematically discuss and compare measurement data, the theoretical basis has to be complemented by fundamental fluid dynamics and its modal analysis approaches that are utilized in this thesis.

## 2.5 Fundamentals of Fluid Dynamics

In the very center of fluid dynamics the NAVIER-STOKES-equations (NSE) describe the momentum transport of *viscous fluids* under the *continuum hypothesis*. The NSE can be derived from the CAUCHY momentum equation

$$\frac{D(\rho\mathbf{v})}{Dt} = \langle \mathbf{\sigma} \rangle \cdot \nabla + \rho\mathbf{b}, \quad (2.20)$$

where  $\rho$  is the (fluid) density,  $\mathbf{b}$  is the *specific body force*,  $\langle \mathbf{\sigma} \rangle$  is the CAUCHY *stress tensor* and  $\frac{D(\bullet)}{Dt}$  denotes the *material derivative*. The specific body force is typically caused by gravity, but contributions of (electro)magnetic forces should also be considered in the presence of strong fields. Assuming that the fluid element only experiences gravitational acceleration  $\mathbf{g}$ , rewriting the material derivative in the form of the EULERIAN *derivative*

and using the conservation of mass

$$\frac{\partial \rho}{\partial t} + (\rho \mathbf{v}) \cdot \nabla = 0, \quad (2.21)$$

leads to

$$\rho \frac{\partial \mathbf{v}}{\partial t} + \rho (\mathbf{v} \otimes \nabla) \cdot \mathbf{v} = \langle \boldsymbol{\sigma} \rangle \cdot \nabla + \rho \mathbf{g}. \quad (2.22)$$

Further assuming that the CAUCHY stress tensor for a NEWTONIAN fluid only depends on thermodynamic pressure  $p$ , on the divergence of the velocity and linearly on the symmetric part of the velocity gradient tensor  $\langle \mathbf{L} \rangle = \mathbf{v} \otimes \nabla$ , also called the *rate-of-strain tensor*, one arrives at the isotropic, linearly viscous ansatz

$$\langle \boldsymbol{\sigma} \rangle = (-p + \lambda (\mathbf{v} \cdot \nabla)) \langle \mathbf{I} \rangle + \frac{\mu}{2} (\mathbf{v} \otimes \nabla + \nabla \otimes \mathbf{v}), \quad (2.23)$$

where  $\langle \mathbf{I} \rangle$  is the identity tensor,  $\mu$  and  $\lambda$  denote the *dynamic viscosity* and the *first LAMÉ parameter* of fluid dynamics, respectively, and  $\nabla \otimes \mathbf{v} = \langle \mathbf{L}^T \rangle$  is the transpose of the velocity gradient tensor. In general, both  $\lambda$  and  $\mu$  depend on temperature and pressure, although their value may not change significantly. Substituting the stress tensor in equation 2.22 with the constitutive relation from equation 2.23 and assuming  $\lambda$  and  $\mu$  to be constant, yields the equation of motion

$$\rho \frac{\partial \mathbf{v}}{\partial t} + \rho (\mathbf{v} \otimes \nabla) \cdot \mathbf{v} = -p \nabla + (\lambda + \mu) (\mathbf{v} \cdot \nabla) \nabla + \mu (\mathbf{v} \otimes \nabla) \cdot \nabla + \rho \mathbf{g}, \quad (2.24)$$

which can be reduced in the case of an *incompressible fluid* ( $\mathbf{v} \cdot \nabla = 0$ ) to the incompressible NSE

$$\frac{\partial \mathbf{v}}{\partial t} + (\mathbf{v} \otimes \nabla) \cdot \mathbf{v} = \frac{-p \nabla}{\rho} + \nu (\Delta \mathbf{v}) + \mathbf{g}, \quad (2.25)$$

where  $\Delta(\bullet) = (\bullet)\Delta = \nabla^2(\bullet)$  denotes the vector LAPLACE operator,  $\nu = \frac{\mu}{\rho}$  is the kinematic viscosity and the gradient of pressure could also be expressed in the more familiar term  $\nabla p$  since pressure is a scalar field. The NSE constitute a system of partial differential equations that is inherently nonlinear due to the convective acceleration on the left-hand side. By scaling the quantities with reference values, nondimensionalization of the NSE can be achieved, which will be useful in the following sections. For simplicity, the derivation of the nondimensionalized equations, which can be found, for example, in Drikakis and Rider [2006], Fox et al. [2004] and Panton [2013], is omitted at this point. Moreover, the resulting variables, often denoted with a superscript asterisk, remain unmarked such that the nondimensionalized equation neglecting gravitational forces reads

$$\frac{\partial \mathbf{v}}{\partial t} + (\mathbf{v} \otimes \nabla) \cdot \mathbf{v} = \nabla p + \frac{1}{Re} \Delta \mathbf{v}, \quad (2.26)$$

where  $Re$  is the REYNOLDS number given by

$$Re = \frac{v_c D_c}{\nu}. \quad (2.27)$$

Here,  $v_c$  and  $D_c$  denote the characteristic velocity and characteristic length of the flow, respectively. A further dimensionless quantity of particular significance is the STROUHAL number  $St$ , which is defined by

$$St = \frac{f_c D_c}{v_c}, \quad (2.28)$$

where  $f_c$  is the characteristic frequency of the flow, e.g. the frequency of vortex shedding or forcing.

The physical quantities of interest,  $\mathbf{v}$ ,  $p$  and possibly  $\rho$ , generally depend on time and position. Whereas the spatial dependence is often the principal reason for the investigations conducted, precise knowledge of the time dependence of the fields is mostly of subordinate importance. However, the temporal resolution of experimental studies should be reasonably high such that the time scales of processes of increased significance are accurately covered. Therefore, measuring flow, especially at high REYNOLDS numbers, involves measuring *turbulence*, i.e. the irregular, three-dimensional motion of fluids on a broad spectrum of fluctuating scales. To separate the scales of interest, whether on a temporal, spatial, energy-related or dynamical basis, is a key objective in turbulence research. As the most manifest approach to scale separation, the decomposition of flow into a *mean flow* and a *fluctuating flow* has to be mentioned. In addition, scale separation may take into account periodic contributions. The theory and implications of these decomposition approaches are briefly outlined in the following section.

## 2.6 Flow Decomposition Based on Time Scales

The decomposition of instantaneous flow quantities into a mean and a fluctuating part proposed by OSBORNE REYNOLDS in 1894 is expressed by

$$q(\mathbf{x}, t) := \bar{q}(\mathbf{x}, t) + q'(\mathbf{x}, t), \quad (2.29)$$

where  $q$  is the instantaneous quantity,  $\bar{q}$  is the mean of the quantity,  $q'$  is the fluctuating part of the quantity, and  $\mathbf{x}$  and  $t$  denote position and time, respectively. The definition of the mean value depends on the case of application. In a general sense, the mean can be formulated as the convolution product of a normalized *filter function*  $G$  and the instantaneous value (Piquet [2013])

$$\bar{q}(\mathbf{x}, t) = G * q = \int G(\mathbf{x} - \mathbf{x}', t - t') q(\mathbf{x}', t') \, d\mathbf{x}' dt', \quad (2.30)$$

where the filter function has to be chosen compliant to the required mean value. However, the resulting convolution product has to fulfill the conditions of a REYNOLDS *operator*: linearity, commutativity with respect to time- and space-derivatives and the projection condition  $\overline{\bar{q}_1 q_2} = \bar{q}_1 \bar{q}_2$ , where  $q_1$  and  $q_2$  are two different instantaneous quantities (Meneveau and Sagaut [2006]).

An *ensemble average* does mathematically fulfill the requirements for an infinite number of samples  $N_s$  in the ensemble. In practice, the *time average* of turbulent flows in a statistically stationary state is the most common averaging technique due to its convenient implementation. Validity, i.e. similarity to the proper ensemble average

(where  $N_s$  tends to infinity), for large numbers of time-resolving measurement samples is often assumed invoking the *ergodic hypothesis*. For the following considerations  $\bar{q}$  is taken as the time average.

Assuming that the requirements of the averaging procedure are met, that gravitational forces can be neglected, as well as substituting the instantaneous quantities  $\mathbf{v} = \bar{\mathbf{v}} + \mathbf{v}'$  and  $p = \bar{p} + p'$  in the NSE 2.25, yields

$$\frac{\partial(\bar{\mathbf{v}} + \mathbf{v}')}{\partial t} + ((\bar{\mathbf{v}} + \mathbf{v}') \otimes \nabla) \cdot (\bar{\mathbf{v}} + \mathbf{v}') = \frac{-\nabla(\bar{p} + p')}{\rho} + \nu \Delta(\bar{\mathbf{v}} + \mathbf{v}'). \quad (2.31)$$

By averaging again and using  $\overline{q'} = 0$ , by definition of the mean, as well as linearity and commutativity with respect to the partial derivatives, the mean momentum transport becomes

$$\frac{\partial \bar{\mathbf{v}}}{\partial t} + (\bar{\mathbf{v}} \otimes \nabla) \cdot \bar{\mathbf{v}} + \overline{(\mathbf{v}' \otimes \nabla) \cdot \mathbf{v}'} = \frac{-\nabla \bar{p}}{\rho} + \nu \Delta \bar{\mathbf{v}}. \quad (2.32)$$

Since

$$\overline{(\mathbf{v}' \otimes \nabla) \cdot \mathbf{v}'} = \overline{\frac{\partial v'_i}{\partial x_j} \mathbf{e}_i \otimes \mathbf{e}_j \cdot v'_k \mathbf{e}_k} = \overline{v'_j \frac{\partial v'_i}{\partial x_j} \mathbf{e}_i} = \overline{\frac{\partial(v'_i v'_j)}{\partial x_j} \mathbf{e}_i} - \overline{v'_i \frac{\partial v'_j}{\partial x_j} \mathbf{e}_i} \quad (2.33)$$

and taking the average of the decomposed incompressible continuity equation  $(\bar{\mathbf{v}} + \mathbf{v}') \cdot \nabla = 0$  holds

$$\overline{(\bar{\mathbf{v}} + \mathbf{v}') \cdot \nabla} = \bar{\mathbf{v}} \cdot \nabla = 0 \quad \Rightarrow \quad \mathbf{v}' \cdot \nabla = \frac{\partial v'_j}{\partial x_j} = 0, \quad (2.34)$$

equation 2.32 can be written as

$$\frac{\partial \bar{\mathbf{v}}}{\partial t} + (\bar{\mathbf{v}} \otimes \nabla) \cdot \bar{\mathbf{v}} = \frac{-\nabla \bar{p}}{\rho} + \nu \Delta \bar{\mathbf{v}} - \overline{(\mathbf{v}' \otimes \nabla) \cdot \mathbf{v}'}. \quad (2.35)$$

The equation system 2.35 is referred to as the REYNOLDS-*averaged* NAVIER-STOKES *equations* (RANS equations), which resemble the NSE except for the rightmost term. Given that the flow is in a statistically stationary state, the partial derivative with respect to time can be eliminated such that equation 2.35 can be formulated as

$$\rho(\bar{\mathbf{v}} \otimes \nabla) \cdot \bar{\mathbf{v}} = \left( -\bar{p} \overset{\langle 2 \rangle}{\mathbf{I}} + 2\mu \overset{\langle 2 \rangle}{\mathbf{S}} - \rho \overline{(\mathbf{v}' \otimes \nabla) \cdot \mathbf{v}'} \right) \cdot \nabla, \quad (2.36)$$

where  $\overset{\langle 2 \rangle}{\mathbf{S}}$  is the *mean rate-of-strain tensor* defined by  $\overset{\langle 2 \rangle}{\mathbf{S}} = \frac{1}{2} \left( \frac{\partial \bar{u}_i}{\partial x_j} + \frac{\partial \bar{u}_j}{\partial x_i} \right) \mathbf{e}_i \otimes \mathbf{e}_j$  and  $-\rho \overline{(\mathbf{v}' \otimes \nabla) \cdot \mathbf{v}'} =: \overset{\langle 2 \rangle}{\boldsymbol{\tau}}$  is the REYNOLDS stress tensor (RST), which is usually simply denoted as  $-\rho \overline{u'_i u'_j}$ . The RST is symmetric such that there are six unknown component fields, the *turbulent stresses*, stemming from turbulent velocity fluctuations and influencing the mean momentum transport. Modelling the turbulent stresses is one of the major issues in the field of research on turbulence. Moreover, in clinical applications involving MRI, knowledge of the REYNOLDS stresses and the related *turbulent viscous shear stresses* is crucial for estimating irreversible pressure loss (Haraldsson et al. [2018]) and the effect

on hemolysis (Yen et al. [2014], Ha et al. [2016]).

The simple formulation of the REYNOLDS decomposition led to a widespread recognition and acceptance. Extraction of the mean flow serves as a temporal decomposition, differentiating (ideally) infinite time scales from all others.

Assuming the existence of a upstream wavemaker, HUSSAIN and WILLIAM C. REYNOLDS proposed a further reaching approach of flow decomposition, nowadays often referred to as *triple decomposition*, which includes an organized wave motion or *coherent* component  $\tilde{q}$  (Hussain and Reynolds [1970])

$$q(\mathbf{x}, t) := \bar{q}(\mathbf{x}, t) + \tilde{q}(\mathbf{x}, t) + q'(\mathbf{x}, t), \quad (2.37)$$

where  $\bar{q}$  is the time average,  $\tilde{q}$  is the coherent contribution and  $q'$  is the *remaining* stochastic turbulence, which is, as a result, slightly different from the definition given in equation 2.29. The coherent component is defined in terms of the *phase average*, which is given as

$$\langle q(\mathbf{x}, t) \rangle := \lim_{N_s \rightarrow \infty} \frac{1}{N_s} \sum_{n=0}^{N_s} q(\mathbf{x}, t + nT_c), \quad (2.38)$$

where  $T_c$  is the period of the coherent *cycle*. This approach leads to an average based on the values of the quantity that are present at a fixed phase of the cycle. Consequently, the coherent contribution to the instantaneous value can be obtained from

$$\tilde{q}(\mathbf{x}, t) = \langle q(\mathbf{x}, t) \rangle - \bar{q}(\mathbf{x}, t). \quad (2.39)$$

The triple decomposition approach is particularly advantageous in describing the dynamics of a flow, whose coherent component is expected to be dominant and distinct. This benefit comes at the cost of mathematical complexity. Applying equation 2.37 to the nondimensionalized NSE 2.26 produces a set of mixed terms. Phase-averaging, subsequent time-averaging and then subtracting the time-and-phase average from the phase average leads to

$$\frac{\partial \tilde{\mathbf{v}}}{\partial t} + (\bar{\mathbf{v}} \otimes \nabla) \cdot \tilde{\mathbf{v}} + (\tilde{\mathbf{v}} \otimes \nabla) \cdot \bar{\mathbf{v}} = -\nabla \tilde{p} + \frac{1}{Re} \Delta \tilde{\mathbf{v}} - (\tilde{\mathbf{v}} \otimes \tilde{\mathbf{v}} - \overline{\tilde{\mathbf{v}} \otimes \tilde{\mathbf{v}}}) \cdot \nabla - (\langle \mathbf{v}' \otimes \mathbf{v}' \rangle - \overline{\mathbf{v}' \otimes \mathbf{v}'}) \cdot \nabla, \quad (2.40)$$

where a couple of properties of the combined averaging procedures and the triple decomposed nondimensionalized equivalent of the incompressible continuity equation (see equation 2.34) are used to reduce the number of mixed terms (Reynolds and Hussain [1972]). Again, the equation system, extended by  $\tilde{\mathbf{v}} \cdot \nabla = 0$ , is not closed due to the unknown terms on the right-hand side. Models or simplifications are needed for further advancement. These are examined in section 2.8 when an approach has to be specified for the implementation of the LSA.

But before passing over to the topic of stability, it should be recalled that decomposing flow data can be worthwhile for different reasons and pursuing different objectives. By separating the mean and the coherent component, orderly structure can be withdrawn from the chaotic nature of turbulence with respect to its behaviour in time. Clearly,

other objectives could aim at the spatial structure as well as the energy content of dominating or minor flow features. The following approach involves the separation of the energetically most relevant *modes* out of a series of measurements.

## 2.7 Proper Orthogonal Decomposition

The purpose of applying a POD to such a series of measurements is to extract a *basis* for a *modal decomposition* (Berkooz et al. [1993]). The basis is chosen algorithmically so as to be optimal with respect to the  $L^2$ -norm (Holmes et al. [2012]), which is related to the energy content of signals. Therefore, applying a POD to a velocity vector field covers the maximal (specific) kinetic energy content with a given number,  $N_m$ , of *basis functions* (Tropea et al. [2007]), also referred to as modes. Moreover, the extracted modes are orthogonal, which is especially useful for reduced-order modelling (Taira et al. [2017]).

Typically, distinction is made between the *spatial* and the *snapshot* POD. Further classifications may take into account, for example, the manner of separating the variables, the approach to solving the problem with methods from linear algebra and the set of flow data. For the given case of application, only the snapshot POD (see Sirovich [1987]) on a REYNOLDS decomposed velocity component field with the eigenvalue decomposition applied will be considered.

The decomposition starts with the fluctuating *data vector*  $\mathbf{x}$  defined by

$$\mathbf{x}(\mathbf{x}, t_i) := \mathbf{v}(\mathbf{x}, t_i) - \bar{\mathbf{v}}(\mathbf{x}), \quad (2.41)$$

where  $\bar{\mathbf{v}}$  and  $\mathbf{v}$  represent the mean velocity and instantaneous velocity data vector at discrete points in time  $t_i$ . The data vectors are stacked arrays of velocity values where each value corresponds to a fixed spatial position  $\mathbf{x}$ . The approach of decomposing the fluctuating data vector into spatial modes  $\mathbf{u}_j$  and corresponding temporal coefficients  $a_j$  can be expressed by the linear superposition

$$\mathbf{x}(\mathbf{x}, t_i) = \sum_j a_j(t_i) \mathbf{u}_j(\mathbf{x}), \quad (2.42)$$

where the spatially dependent modes should be chosen optimally in the abovementioned context.

Given that the field consists of  $N_p$  equally spaced points where real-valued data have been acquired at  $N_s$  sampling points in time, a data matrix  $\mathcal{X} \in \mathbb{R}^{N_p \times N_s}$  can be constructed with the columns being the data vectors at the single sampling points in time. This approach can be extended if more than one measurement quantity is desired to be included. In that case the additional fields, again time-dependent and stacked as data vectors, are attached to, for example, the bottom end of  $\mathcal{X}$ .

With all data being gathered in the data matrix, the utilization of a *singular value decomposition* (SVD) would be sufficient to obtain the modes of the flow field according to

$$\mathcal{X} = \mathbf{U} \mathbf{S} \mathbf{W}^T, \quad (2.43)$$

where  $\mathbb{U}$  is the orthogonal data matrix consisting of the column-wise oriented, spatial modes (left singular vectors),  $\mathbb{S}$  comprises the (non-zero) *singular values*  $\sigma_j$  in descending order on its diagonal and  $\mathbb{W}^T$  is the transpose of the orthogonal matrix consisting of the right singular vectors.

Since  $N_p$  can become very large for the applications of flow field measurements ( $N_p \gg N_s$ ), the direct computation via the SVD is usually disregarded in favor of the following computationally more efficient alternative.

With the snapshot POD, the *snapshot covariance matrix*  $\frac{1}{N_s} \mathbb{X}^T \mathbb{X}$  is calculated. Due to the orthonormality of the (normalized) singular vectors, this leads to the equation of an eigenvalue problem

$$\frac{1}{N_s} \mathbb{X}^T \mathbb{X} \mathbf{w}_j = \sigma_j^2 \mathbf{w}_j, \quad (2.44)$$

where  $\mathbf{w}_j$  is the  $j$ -th right singular vector, which can be interpreted as the  $j$ -th normalized *temporal mode*, and  $\sigma_j$  its corresponding singular value. The scaling factor  $\frac{1}{N_s}$  is often omitted on the left-hand side and apportioned to  $\sigma_j^2$ . Note that the snapshot covariance matrix is of much lower dimension ( $\mathbb{X}^T \mathbb{X} \in \mathbb{R}^{N_s \times N_s}$ ), which significantly reduces the computational effort to solve the eigenvalue problem. The obtained eigenvalues correspond to the square of the singular values. For the chosen approach, the right singular vectors are multiplied by the singular values to obtain the scaled temporal modes  $\mathbf{a}_j$

$$\mathbf{a}_j = \sigma_j \mathbf{w}_j. \quad (2.45)$$

With the ordered singular values and the temporal modes calculated, the first  $N_s$  spatial modes are given by

$$\mathbf{u}_j = \frac{1}{\sigma_j^2} \mathbb{X} \mathbf{a}_j. \quad (2.46)$$

The temporal coefficient  $a_j(t_i)$  of equation 2.42 is found to be the  $i$ -th component of the  $j$ -th temporal mode

$$a_j(t_i) = \mathbf{a}_{j,i}. \quad (2.47)$$

Consequently, the fluctuating velocity field at a given point in time can be approximated with the leading  $N_m$  modes

$$\mathbf{z}(\mathbf{x}, t_i) \approx \sum_{j=1}^{N_m} a_j(t_i) \mathbf{u}_j(\mathbf{x}). \quad (2.48)$$

Typically, the leading POD modes of the fluctuating velocity field are these of the highest interest. Due to their high content of *turbulent kinetic energy*, these modes, together with their time coefficients, are assumed to be the dominant features of the flow under examination and are therefore supposed to span the basis for the spatiotemporally correlated *coherent structures* (Oberleithner [2012]).

A reasonable reconstruction of the flow field can often be achieved by a linear superposition of the first couple of modes and the mean flow. If all  $N_p$  eigenvalues were known, a conceivable criterion for the number of modes to retain would base on the amount of

energy, which is reflected by the ratio of the sum of the eigenvalues (Taira et al. [2017])

$$\frac{\sum_{j=1}^{N_m} \sigma_j^2}{\sum_{k=1}^{N_p} \sigma_k^2} \approx 1. \quad (2.49)$$

Further important points to mention are that the modes often appear in conjugated pairs and that the POD modes, although optimal with respect to energy content, are not necessarily the most important with respect to impact on the flow dynamics (Taira et al. [2017]). In general, one POD mode may depict features of flow that correspond to multiple scales in space or time, thereby mixing different frequencies (Frederich and Luchtenburg [2011]).

POD belongs to the class of *data-based* modal decomposition techniques. In contrast, the following approach to facilitate these decompositions, the global LSA can be attributed to the field of *operator-based* modal decomposition techniques.

## 2.8 Global Linear Stability Analysis

The starting point for the presented application of the global LSA is given by the nondimensionalized incompressible NSE including the corresponding continuity equation  $\mathbf{v} \cdot \nabla = 0$ . Given that the exact (steady) solutions  $\mathbf{v}_b$  and  $p_b$  to this equation system are known from experiments or numerical studies, global LSA aims at evaluating the stability of the *base flow* under small velocity and pressure *perturbations*,  $\epsilon \mathbf{v}''$  and  $\epsilon p''$ , where  $\epsilon$  is a small perturbation factor ( $\epsilon \ll 1$ ). In essence, the (temporal) development of these disturbances with respect to the base flow solution is considered (Taira et al. [2017]). That solution depends on two (*BiGlobal*) or three (*TriGlobal*) spatial directions (Theofilis [2011]).

The ansatz  $\mathbf{v} = \mathbf{v}_b + \epsilon \mathbf{v}''$ ,  $p = p_b + \epsilon p''$  is substituted into the nondimensionalized NSE (2.26) and the corresponding continuity equation. Since the base flow is a solution of the equation system and thus cancels out, this substitution yields

$$\frac{\partial \mathbf{v}''}{\partial t} + (\mathbf{v}'' \otimes \nabla) \cdot \mathbf{v}_b + (\mathbf{v}_b \otimes \nabla) \cdot \mathbf{v}'' = -\nabla p'' + \frac{1}{Re} \Delta \mathbf{v}'' - \epsilon (\mathbf{v}'' \otimes \nabla) \cdot \mathbf{v}'', \quad (2.50)$$

where the rightmost term can be interpreted as a *nonlinear forcing term* of the perturbation field, which vanishes for  $\epsilon \rightarrow 0$ . Neglecting the rightmost term, i.e. *linearizing* equation 2.50, results in a differential equation that would resemble equation 2.40, if it was not for the *interaction terms* of the coherent and stochastic velocity fields. By imposing two rigorous assumptions on these interaction terms, a more apparent similarity of the equations can be achieved. Firstly, it is assumed that the nonlinear interactions of the coherent component are weak and can be omitted (Müller et al. [2019])

$$(\tilde{\mathbf{v}} \otimes \tilde{\mathbf{v}} - \overline{\tilde{\mathbf{v}} \otimes \tilde{\mathbf{v}}}) \cdot \nabla = \mathbf{0}. \quad (2.51)$$

## 2 Physical and Mathematical Essentials

Secondly, the term  $(\langle \mathbf{v}' \otimes \mathbf{v}' \rangle - \overline{\mathbf{v}' \otimes \mathbf{v}'}) \cdot \nabla = \widetilde{\mathbf{v}' \otimes \mathbf{v}'}$ , which can be interpreted as the REYNOLDS stress oscillation evoked by a traversing coherent disturbance (Reynolds and Hussain [1972]), is modelled by

$$\frac{1}{Re_t} \tilde{\mathbf{v}} \otimes \nabla \approx \overset{\langle 2 \rangle}{\tilde{\boldsymbol{\tau}}} := -(\langle \mathbf{v}' \otimes \mathbf{v}' \rangle - \overline{\mathbf{v}' \otimes \mathbf{v}'}), \quad (2.52)$$

where  $Re_t$  is the *turbulent* REYNOLDS number and  $\overset{\langle 2 \rangle}{\tilde{\boldsymbol{\tau}}}$  denotes the *stochastic-coherent interaction tensor*. The turbulent REYNOLDS number is defined via  $Re_t := \frac{v_c D_c}{\nu_t}$ , where  $\nu_t$  is the *eddy viscosity* and is assumed to be constant within the ROI. This is in contrast to the common approach—paralleling the BOUSSINESQ *hypothesis*—, in which  $\nu_t$  is modelled as a scalar field depending on, for example, the RST  $\overset{\langle 2 \rangle}{\tilde{\boldsymbol{\tau}}}$  and the mean rate-of-strain tensor  $\overset{\langle 2 \rangle}{\tilde{\mathbf{S}}}$  (Müller et al. [2019], Kaiser et al. [2018]). So far, the question of how to optimally model the eddy viscosity or, more generally, the interaction term is still unanswered. The given simplified model is chosen because the REYNOLDS stresses remain unknown from the experimental data used for the analysis.

With these two assumptions from equations 2.51 and 2.52 the nondimensionalized incompressible transport of coherent momentum from equation 2.40 can be expressed by

$$\frac{\partial \tilde{\mathbf{v}}}{\partial t} + (\bar{\mathbf{v}} \otimes \nabla) \cdot \tilde{\mathbf{v}} + (\tilde{\mathbf{v}} \otimes \nabla) \cdot \bar{\mathbf{v}} = -\nabla \tilde{p} + \frac{1}{Re^*} \Delta \tilde{\mathbf{v}}, \quad (2.53)$$

where

$$\frac{1}{Re^*} = \frac{1}{Re} + \frac{1}{Re_t} \quad (2.54)$$

defines the *effective* REYNOLDS number.  $Re^*$  is used to model the ostensibly increased influence of viscosity due to turbulence. It is worth noting that the equations 2.53 and 2.50 in its linearized formulation look similar, but they differ in that the perturbation due to the coherent component is not necessarily small and the mean flow does not provide an exact solution of the NSE. Still, the application of the global LSA to the mean flow is an interesting variant since the NSE are linearized around the flow attractor rather than around the steady solution (Noack et al. [2011]). This leads to a differing interpretation and implication of the results, as will be shown shortly.

For the given case of an axisymmetric geometry it is useful to define the modal approach of  $\tilde{\mathbf{v}}$  and  $\tilde{p}$  with respect to the cylindrical coordinate system from section 2.1. This is combined with a separation of the variables  $\mathbf{x}$  and  $t$  as

$$\tilde{\mathbf{v}}(\mathbf{x}, t) := \Re\{\hat{\mathbf{v}}(r, x) e^{i(m\phi - \omega t)}\}, \quad (2.55)$$

$$\tilde{p}(\mathbf{x}, t) := \Re\{\hat{p}(r, x) e^{i(m\phi - \omega t)}\}, \quad (2.56)$$

where  $\hat{\mathbf{v}}$  and  $\hat{p}$  denote the velocity and pressure amplitude fields, respectively,  $\omega$  is the mode's complex-valued angular frequency,  $m$  is the *azimuthal wave number* and  $\Re$  denotes the real part of a complex function. The components of  $\hat{\mathbf{v}}$  with respect to the cylindrical coordinate system are denoted by  $\hat{v}_x = \hat{u}$ ,  $\hat{v}_\rho = \hat{v}$  and  $\hat{v}_\phi = \hat{w}$  (see section 2.1). Applying this ansatz to equation 2.53 and the corresponding continuity equation leads to the formulation of a *generalized eigenvalue problem* (GEVP). After the fields and

their derivatives are discretized in terms of the linear operators  $\mathbb{A}$  and  $\mathbb{B}$ , the GEVP can be expressed by

$$\mathbb{A}\hat{\mathbf{q}} = \omega\mathbb{B}\hat{\mathbf{q}}, \quad (2.57)$$

where the resulting eigenvector  $\hat{\mathbf{q}}$  is written as a generalized data vector, which comprises the (spatially discrete) amplitude values of  $\hat{\mathbf{v}}$  and  $\hat{\mathbf{p}}$  (cf. Theofilis [2011]). The eigenvectors represent the instability modes with corresponding (nondimensionalized) complex eigenvalues  $\omega$ . While the real part of  $\omega$  corresponds to the angular eigenfrequency, the imaginary part represents the growth rate of the instability mode. An interpretation BARKLEY pointed out for the mean flow stability analysis of a laminar cylinder wake flow is that the mean flow is marginally stable when it is understood as the steady solution of the NSE under the effect of a turbulent forcing due to REYNOLDS stresses. This is assumed to rely on a nonlinear process, which causes the mean flow to reach a state where the oscillation amplitude is saturated (Barkley [2006]). NOACK et al. support that proposition demonstrating time-averaged cases with nearly zero growth rates (Noack et al. [2011]).

With the theoretical basis being established, the thesis proceeds with the methodical approach, which also includes the description of the relevant test facilities and modules that have been used and constructed.

## 3 Materials and Methods

One substantial part of the designated task and intended purpose was to facilitate velocity field measurements of a turbulent flow with a particular technical significance by means of MRV. This is a novelty for both participating institutions, the HFI and the PTB. In order to conduct the experiments at the facilities of the PTB, a new test rig was to be designed and constructed, meeting the safety requirements of the MR system and its surroundings. Moreover, the principal item of this test rig, the *test module* or *phantom*, had to fulfill another set of requirements since PIV experiments had to be realized for comparison and validation. To briefly introduce the aspects of design and construction is the motive of the following pages. Thereafter, the utilized specific measurement and data analysis techniques are explained on the theoretical basis of chapter 2.

### 3.1 Experiment Design and Construction

The core of the test module is the swirler, or formally swirl generator. Different swirler geometries have been tested at the HFI throughout the last years. Due to its simple design, compact size and two modification options, the decision was made in favor of the HP swirler, which was developed at the HFI and thoroughly investigated by REICHEL before (Reichel [2017]).

The swirl generator is characterized by eight *eccentric vanes* and an interior frustum of a cone that redirect the axial pipe flow into a cylindrical *mixing tube*, thereby inducing tangential velocities and thus a rotating motion of the fluid particles. Subsequently, the fully turbulent swirling jet emerges from the mixing tube's downstream outlet into the confined combustion chamber. Swirl intensity can be manipulated by exchangeable blocking rings outside of the vanes and the choice of axial orifice insets located at the upstream swirler end. Four rings and five orifice insets were manufactured to allow for diverse combinations, of which only a selected set has been used in the experimental study. Minor changes were made with respect to the original design. These changes mainly concern omitting unused geometrical features and scaling of the swirl generator. Nevertheless, geometrical similarity was retained as far as possible.

The design REYNOLDS number was predefined to  $Re = 20000$ , and it is based on the mixing tube diameter  $D_c := D = 0.0245$  m and the *bulk velocity*  $v_c := v_0$  inside the mixing tube. This leads to a volume flow rate of approx.  $1.39 \text{ m}^3 \text{ h}^{-1}$ . Since ferromagnetic materials are prohibited within the vicinity of the MR system, exclusively synthetic materials are used. The swirler is made of polymethyl methacrylate (PMMA), the screws consist of polyamide 6 (PA6, also referred to as polycaprolactam or Perlon). While the swirler is integrated in both measurement setups, additional components and their assembling depend on the respective measurement that is carried out.

### 3.1.1 PIV Setup

PIV experiments were performed at the HFI water laboratory. The test rig basically consists of a 3 m<sup>3</sup> cistern, an in-line multi-stage centrifugal pump, an electromagnetic flowmeter and the upright standing, transparent water tank in the shape of a rectangular cuboid. For flow rate control, a bypass, which leads back to the cistern and is controlled by a ball valve, is positioned between pump and flowmeter. A waterproof front door facilitates equipping the tank with the test module components. These include three fixating horizontal PMMA plates, two transparent PMMA pipes with an inner diameter of approx. 115 mm and a total of nine polyvinyl chloride (PVC) adapters to connect the swirler and the pipes to the plates. The central adapter protrudes from the middle plate to enhance optical access. The lengths of the upstream and downstream pipe are 200 mm and 500 mm, respectively, while the thickness of both is 5 mm. A section of the upper half of the  $xy$ -plane is illuminated with a neodymium-doped yttrium aluminum garnet (Nd:YAG) laser through the side window. A scientific complementary metal-oxide semiconductor (sCMOS) camera, including an EF-EOS mount adapter for remotely adjusting the focus and aperture of the lens, is positioned close to the rear window for the purpose of image acquisition. An overview of the most important technical equipment is given in table 3.1. Technical drawings of the module components and a simplified test rig illustration are attached in Appendix A and Appendix B, respectively.

Technical element	Name or specification	Manufacturer
Centrifugal pump	Movitec V6/7 B	KSB SE & Co. KGaA
Flowmeter	Promag 50P25	Endress+Hauser AG
Laser system	Twins BSL CFR, ICE 450	Quantel USA, Inc. (Lumibird S.A.)
Camera	pco.edge 5.5	PCO AG
Lens	EF 35 mm f/2	Canon K.K.

Table 3.1: Technical equipment used for the PIV experiments

The laser sheet is aligned with the  $xy$ -plane employing center line marks and a single-level target. The target is attached to a fixation gadget, which allows for readjustments after filling the water tank. Seeding (silver coated hollow glass spheres of 10  $\mu\text{m}$  diameter) is gradually added to the reservoir such that an adequate and homogeneous particle density is achieved. Bright reflections of the laser sheet, which may impair the image quality or affect the camera sensors, are on the one hand reduced by a black optical aluminum foil on the rear side of the combustion chamber and by masking adhesive tapes on the water tank windows on the other hand.

### 3.1.2 MRV Setup

The test rig of the MRV experiments can be divided up into two sections. Firstly, the *supply and regulation system* outside of the shielded scanner room allows for the usage of ferromagnetic materials and common electronic components. Secondly, the *measurement system* inside the scanner room, which is subjected to strict requirements concerning

### 3 Materials and Methods

material selection, waterproofness and operator convenience. The two systems are connected through two small *wave guides* in the shielded wall, which are equipped with appropriate brass fittings.

The supply and regulation system consists of a 0.6 m<sup>3</sup> water reservoir, an adjustable centrifugal aquarium pump, a turbine flowmeter and the main test rig. The rig itself is made of aluminum profiles and equipped with two float-type flow meters as well as a barometer on a T-shaped flow manifold. For prospective experiments at the MR facility, special attention is paid to the possibility of variably complementing the rig. The performed measurements require a bypass, which includes a ball valve and leads back to the reservoir, for flow rate control. Different setups for future applications are conceivable and easy to implement. In order to reduce the formation of bubbles, approx. 10 mL of a 45 % solution of polysorbate 20, also known as Tween 20, is added to the partially filled reservoir (approx. 150 L of water). The pump is mounted on a wooden frame, which also serves as the fixation of the near-ground tubing and the flowmeter.

The measurement system consists of a PVC phantom, which is connected to the supply system by PVC tubing. At the rear and front end of the phantom, a three-way and two-way ball valve are mounted, respectively. When the swirler configuration is modified, the former serves as a drain tap as soon as the latter is closed. Since the measurements are performed on the horizontal patient couch, a downstream air vent is provided at the upper edge to ensure the complete filling of the combustion chamber. The phantom is composed of an upstream and downstream pipe, each connected to an adapter fitting, the central socket and, of course, the swirler, which is inserted from the rear end. To match both the upstream region's and the combustion chamber's length of the PIV experiments, the lengths of the PVC pipes are adjusted to 208 mm and 492 mm, respectively. The inner diameter of both pipes is approx. 115.4 mm, which implies a slight discrepancy with respect to the PMMA pipes. A 3 T open bore MR system and a knee coil are used for the measurements, which are controlled from the operator room. Specifications of the essential components are listed in table 3.2. Technical drawings can be found in Appendix A, and a simplified illustration of the test rig is attached in Appendix B.

Technical element	Name or specification	Manufacturer
Centrifugal pump	DC Runner 9.2	AB Aqua Medic GmbH
turbine flowmeter	DFM-Ms R 3/4"	B.I.O-TECH e.K.
MR system	MAGNETOM Verio	Siemens AG
Knee coil	Tx/Rx 15-channel	Quality Electrodynamics, LLC (Siemens AG)

Table 3.2: Technical equipment used for the MRV experiments

For the following sections and chapters it appears convenient to define three (generalized) MRV measurement planes. These are based on the clinical designations of anatomical planes and correspond to the definitions of the applied MR system.

Parallel to the ground and fixed to the center of the mixing tube's outlet, i.e. in the *xy*-plane, the *coronal plane* is defined. The perpendicular plane, which is also fixed to

the mixing tube's outlet and coincides with the  $zx$ -plane is referred to as the *sagittal plane*, although median plane would be more precise at this point. The *transverse plane* completes the set. It is as well perpendicular to the coronal plane, but coincides with the  $yz$ -plane and is generalized in that it has no fixing point. The axial position is provided for the determination of these cross sections.

## 3.2 PIV Principle, Settings and Specifications

At first, a short recapitulation of the applied PIV principle is given in order to put the following specifications of the measurements and data analysis on a firm foundation. Note that this is not an exhaustive explanation of the method, but rather a detailed view of the applied particular case. Following this, the performed measurements and their most important parameters are specified.

### 3.2.1 PIV Principle

PIV is a widely used method in studying air and water flows, and it facilitates the spatially resolved determination of the instantaneous velocity field (Raffel et al. [2007]). This non-intrusive, optical measurement technique is based on the *visualization* and subsequent *evaluation* of *particle displacements*. Particles are added to the fluid under investigation, which is water for the given study, in the form of the aforementioned seeding. Visualization means that the particles in the measurement plane of approx. 1.5 mm thickness are illuminated twice by short laser pulses. This allows for the determination of their momentarily positions by taking two triggered camera images. Evaluation is performed through a cross-correlation—by means of fast FOURIER transforms (FFT)—of the respective momentarily particle positions given by the two snapshots. On the assumption that the particles follow the pathlines of the fluid ideally, the particle displacement  $\Delta\mathbf{r}$  within the time difference  $\Delta t$  of the pulses can be identified with the fluid velocity at the particle's initial position. For this purpose, it is also assumed that the fluid velocity does not vary within the time difference, which is commonly termed *pulse distance* or pulse delay.

A preceding target-based calibration of the camera view field is obligatory to provide the scaling factor between camera pixels and, for example, millimeters. Furthermore, the view plane is subdivided into a set of quadratic interrogation areas, also referred to as *windows*, before the cross-correlation of the images is executed. If  $\Delta t$  is chosen such that the particles do not cross the window borders, the correlation peak has to be detected inside the same window. Commonly, the time difference is chosen to a smaller value that corresponds to a displacement of half the window size or less. Finally, a further assumption states that the fluid velocity within a single window is uniform and can thus be calculated from the correlation peaks.

This outlined principle concerns the ordinary PIV, also referred to as *Mono PIV*, which enables the determination of two velocity components in their respective dimensions (2D2C). That is, the *through-plane displacement*, also referred to as out-of-plane displacement, cannot be detected and exiting particles, which are naturally common in swirling flows, have to be taken into consideration when deciding on the pulse distance.

The described method is depicted in a simplified version in Figure 3.1 (adapted from Schlüßler [2017]).

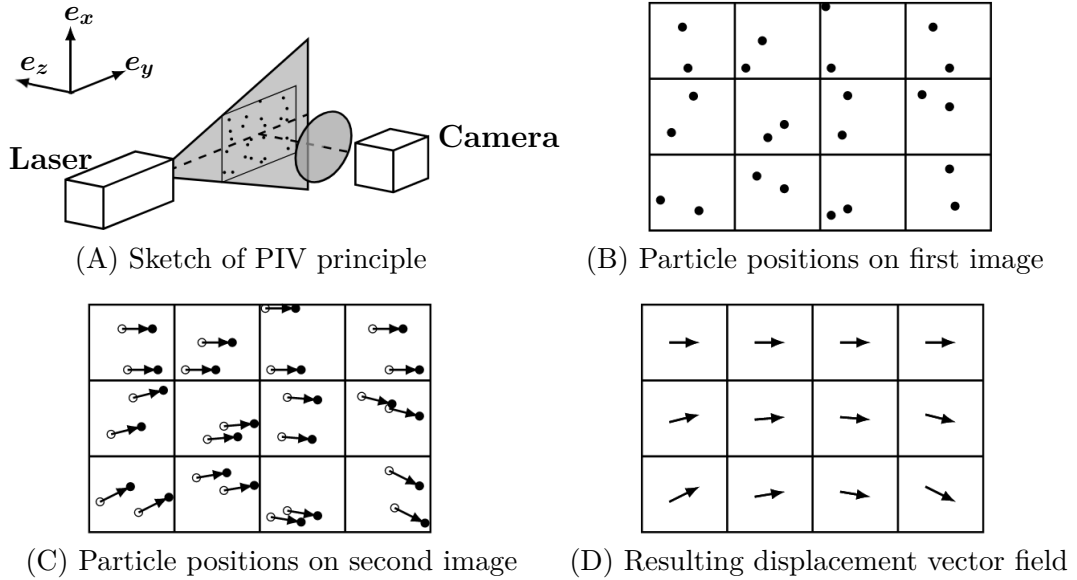


Figure 3.1: Simplified PIV principle. Adapted from *Optisches Geschwindigkeitsmesssystem zur vektoriellen Erfassung instationärer Strömungsprozesse* (p. 12), by R. Schlüßler, 2017, Dresden, Germany: Sächsische Landesbibliothek - Staats- und Universitätsbibliothek Dresden. Copyright 2017 by R. Schlüßler. Adapted with permission.

### 3.2.2 PIV Settings and Specifications

A set of eight swirler configurations is investigated experimentally. The purpose of two of these is to determine whether the installation position of the swirler within the central adapter markedly alters the mean flow appearance, which cannot be confirmed. One of the remaining six configurations is selected as the *base case* (*Re20000\_dj0\_br575*), for which two kinds of modifications are applied. These modifications include the attachment of either thicker blocking rings (*br800* and *br1100*) or the choice of axial orifice insets (*dj65* and *dj96*). At last, a non-swirling jet with sealed vanes is tested for diversification and comparison. All measurements are performed at least twice for reasons of verification, and all configurations but one are tested at  $Re = 10000$ ,  $Re = 20000$  and  $Re = 30000$ . The non-swirling jet configuration is an exception as the case for  $Re = 30000$  is omitted.

Of these measurements a small set depicting different characteristic flow patterns is selected for the subsequent comparison with MRV data. The most important settings of this set of PIV experiments are listed in table 3.3. The complete evaluation process and

### 3 Materials and Methods

the extraction of the mean images of the data sets is performed using PIVview2C 3.6 (PIVTEC GmbH). MATLAB<sup>®</sup> (release R2015a) is used for merging and post-processing of the respective mean images.

	Re20000		Re10000
	dj0_br575	dj96_br575	dj96_brInf
<b>General settings</b>			
wavelength	532 nm		
resolution	2560 × 2160 pixel		
Sampling rate	7.5 s <sup>-1</sup>		
Pulse distance	150 μs	150 μs	200 μs
$N_s$	10 × 1000	2 × 1125	2 × 1125
<b>Pre-Processing</b>			
Filter applied	None		
Background handling	Division by average background		
<b>Evaluation</b>			
Window size	16 × 16 pixel		
Step size	8 × 8 pixel		
Limit ROI	Crop margins		
Correlation mode	Standard (FFT) correlation, uniform weighting		
Interrogation	Multi-grid interrogation (grid refinement)		
Initial window size	256 × 256 pixel		
Image Interpolation	B-spline interpolation, fourth-order		
Sub-pixel peak fit	least squares GAUSS fit (3 × 3 points)		
<b>Outlier detection</b>			
Normalized median test	Threshold: 4.0		
Max. displacement test	8.0 pixel		
Max. displacement diff.	2.0 pixel		
Min. SNR	10.0		
<b>Outlier replacement</b>			
By interpolation	enabled		
By reevaluation	enabled, with larger sample		
Validation passes	5		

Table 3.3: PIV settings for the selected cases

### 3.3 MRV Principle, Selected Methods and Specifications

The physical essentials of obtaining measurement signals on the basis of NMR have already been addressed in section 2.4. The question remains how spatially resolved images and, consequently, velocity vector fields are determined from the obtained signal. The answer to this question partially depends on the deployed measurement method. Since MRI in general is a technique predominantly used in the diversified field of clinical examinations, a wide-ranging variety of dedicated measurement principles and *sequences* is available for the various specific requirements. In the following section the small portion of selected methods as well as the common ground of the basic approach to spatial encoding are explained or outlined.

The section starts with the description of signal modification, then covers the topic of spatial encoding, which includes a brief introduction to the concept of *k-space*, and finally points out the aspects of *velocity encoding* and the measurement specifications.

#### 3.3.1 Signal Modification and Gradient Fields

As explained before in section 2.4.4, the net magnetization in its non-equilibrium state induces the FID signal in the receiver coils. The decay of the signal, in terms of the envelope, corresponds to the vanishing transverse magnetization, which is according to the BLOCH equations (2.17-2.19) governed by the transverse relaxation time  $T_2$  or, more precisely, by  $T_2^*$ . However, in order to facilitate spatial encoding, it is advantageous to modify the FID signal in a certain manner such that it generates a well-defined *echo*. In a first step, the concept of *gradient echo* (GRE) sequences involves accelerating the process of signal decay by superposing a linear magnetic gradient field  $\overset{\langle 2 \rangle}{\mathbf{G}}$  on the main magnetic field for a definite period of time. For the common small magnetic gradient fields, typically on the order of several  $\text{mT m}^{-1}$ , it is justifiable to assume that the gradient field only affects the  $z$ -component of the main magnetic field (i.e.  $B_0$ ) (Vlaardingerbroek et al. [2013]). According to equation 2.12, the resulting spatially dependent magnetic flux density,  $\mathbf{B}_0 + \overset{\langle 2 \rangle}{\mathbf{G}} \cdot \mathbf{x}$ , where  $\mathbf{x}$  is the position vector with respect to the *isocenter* of the scanner system, thereby varies the precession frequency  $\omega_0$  linearly with  $\mathbf{x}$  and depending on the proportionality constant  $\gamma$ , which implies a spatially dependent  $\omega_0$ . Since these deviations of the precession frequency result in an additional reduction of the transverse relaxation time, the measurement signal, which has a damped sinusoidal shape, quickly diminishes due to enhanced dephasing. By reversing the polarity of the gradient magnetic field at the end of the definite period, the externally imposed part of the dephasing process can be reversed and the echo occurs before the end of the  $T_2^*$ -decay. The simplified process is depicted in figure 3.2, where  $S_g$  represents the generic signal.

Usually, the time between the center of the RF pulse and the center of the echo is defined as *echo time* TE, and the time between two subsequent RF pulses is defined as *repetition time* TR. In most cases TR is desired to be short enough to provide fast image acquisition. Since the signal amplitude depends on the initial longitudinal magnetization, which

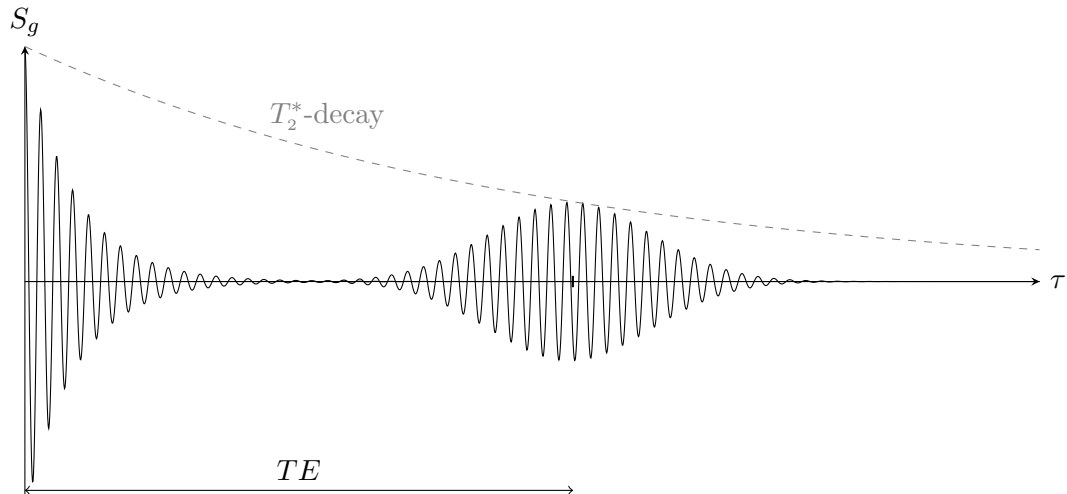


Figure 3.2: Simplified illustration of the gradient echo within  $T_2^*$ -decay

in turn depends on  $T_1$  (see equation 2.16), TR would be limited by long longitudinal relaxation times if  $90^\circ$  pulses were applied. Thus, the flip angle  $\alpha$  (see equation 2.14) is reduced such that a short TR and sufficient signal amplitude can be achieved.

The gradient fields are generated by three separate *gradient coils* and can independently be switched in all directions such that the superposition may create oblique slices of constant magnetic flux density. The gradient coils are of particular importance in the process of spatial encoding, which will be apparent shortly. But before proceeding to the next topic, it should be noted that other signal modification techniques exist besides the GRE sequences. Especially worth mentioning is the *spin echo* sequence, which involves a second RF pulse, or multiple further RF pulses, but no gradient fields. The concept allows for a cancellation of the dephasing effects of static magnetic field inhomogeneities and multiple echo generation until the  $T_2$ -decay ceases.

In fact, GRE sequences of multiple RF pulses produce spin echoes as well. In consequence, suitable combinations of gradient strength, flip angle, timing of pulses and other factors spawn various further techniques of signal modification, which cannot be covered in this thesis. For further information, the textbook of BERNSTEIN et al. may serve as an excellent starting point (Bernstein et al. [2004]).

The pulse sequences enable the modification of the signals necessary for image acquisition. Still, information of the signals has to be prepared with respect to its origin before assembling the image from obtained information.

### 3.3.2 Spatial Encoding: Slice Selection

The first question of image acquisition is which information of the signal can be used to indicate spatial location. Since the location is eventually encoded in the waveform detected by the receiver coils, *frequency* and *phase* of the waveform constituents appear as appropriate encoding quantities. Furthermore, the sheer *existence* of an incoming signal indicates that the RF pulse has resonantly interfered with the spin ensemble and

tilted the net magnetization out of its equilibrium such that a transverse magnetization can be detected. The latter property is used for the first encoding step.

When a gradient field alters the effective magnetic flux density depending on spatial position, the resonance frequency  $\omega_0$  varies in linear dependence. Thus, by irradiating the complete measurement volume with a pulse (distribution) of bandwidth  $\Delta\omega_0$ , a locally limited response due to resonance extracts a *slice* out of the volume. The thickness of the slice can be specified by  $\Delta\omega_0$  as well as the by the slice selection gradient (SSG) field and should be chosen with simultaneous consideration of sufficient spatial resolution and sufficient signal intensity, which results from the number of proton spins contributing to the overall magnetization.

Furthermore, the intra-slice dephasing caused by the SSG must be taken into account. Increasing the slice thickness or gradient fields results in differing precession frequencies of the spin ensembles and thus in differing phases inside the selected slice. This problem can be overcome by switching an inverse rephasing gradient in the time interval between the RF pulse and the echo.

Thick slices, however, can otherwise be interpreted as *slabs* and hence be treated with a different three-dimensional encoding technique. This topic will be briefly addressed in section 3.3.5.

Although the variable gradient fields and RF pulses are capable of selecting slices with virtually any orientation, it is convenient for the following to assume the slice to be orientated coinciding with the coronal plane, i.e. the  $xy$ -plane in the predefined coordinate system of section 2.1. Note that the convention of the longitudinal  $z$ -component in scanner systems necessarily conflicts with the chosen reference systems. The conventional  $z$ -direction corresponds to the  $x$ -directions in the predefined systems.

With the *slice selection* applied, the problem is reduced to two dimensions. Before introducing the next encoding steps, a brief digression into a rather theoretical part of the imaging concept appears as an expedient foundation.

#### 3.3.3 The Concept of $k$ -Space

Up to this point, the signals detected from the excited slice are still undistinguishable with respect to their origin in the  $xy$ -plane. By applying gradient fields with proper timing in the  $x$ - and  $y$ -direction respectively, ambiguity can be eliminated and a *signal intensity* can be assigned to the discrete voxels. However, the necessary information on the respective signal intensities cannot be obtained within a single measurement process. Information is rather gathered within a series of consecutive measurement passes and subsequently transformed to depict the complete picture. Each measurement pass contributes substantial information, but no single pass is capable of providing unmitigated information on a particular voxel.

The method bases on the underlying concept of  $k$ -space. In order to illustrate the concept, it is useful to investigate the (generic) measurement signal  $S_g(t)$ . For that reason three definitions shall be made. The precessing transverse magnetization of equation 2.15, which is oriented in the  $xy$ -plane, is interpreted as a complex-valued function of time where real and imaginary part correspond to the  $x$ -direction and

### 3 Materials and Methods

$y$ -direction, respectively:

$$M_{\perp} := M_x + iM_y. \quad (3.1)$$

Since the magnetic gradient field is assumed to only affect the main magnetic field, the tensor can be reduced to those components that contribute to the  $z$ -component of the magnetic field by defining  $\mathbf{G}$  following

$$\mathbf{G} := \mathbf{e}_z \cdot \overset{\langle 2 \rangle}{\mathbf{G}}. \quad (3.2)$$

Furthermore, the local phase accumulation  $\varphi$  with respect to the transverse magnetization that precesses with  $\omega_0$ , i.e. the local phase accumulation in the rotating reference system of the spins and therefore the phase accumulation after demodulation, is defined as

$$\varphi(\mathbf{x}, t) := \gamma \int_{t_0}^t \mathbf{G}(\tau) \cdot \mathbf{x} \, d\tau, \quad (3.3)$$

where  $t_s$  is the point in time when the gradients are switched on.

With these definitions a simplified, though plausible model of the measurement signal received by multiple coils is given by FESSLER (Fessler [2010]). The adapted equation for a single coil receiver, a selected slice of thickness  $\Delta z$  and for the assumption that  $T_2^*$  is constant within the slice would read in consistent notation:

$$S_g(t) = \int_{\mathcal{S}} \int c(x, y) M_{\perp}(x, y) \Delta z e^{-\frac{t}{T_2^*}} e^{-i\varphi(x, y, t)} \, dx dy, \quad (3.4)$$

where  $c$  is the receiver coil sensitivity function,  $M_{\perp}$  is the spatially dependent transverse magnetization at the end of the RF pulse and  $\mathcal{S}$  denotes the area of integration, which is given by the extent of the excited slice. Note that the constant initial phase shift due to the RF flip is assumed to be zero or attributed to  $M_{\perp}$ .

Reconsidering equation 3.3 and decomposing it for the Cartesian directions gives

$$\gamma \int_{t_0}^t \mathbf{G}(\tau) \cdot \mathbf{x} \, d\tau = \gamma x \int_{t_0}^t G_x(\tau) \, d\tau + \gamma y \int_{t_0}^t G_y(\tau) \, d\tau + \gamma z \int_{t_0}^t G_z(\tau) \, d\tau, \quad (3.5)$$

which leads to the definition of the *angular wave numbers*  $k_x$  and  $k_y$

$$\gamma \int_{t_0}^t G_x(\tau) \, d\tau =: k_x(t), \quad \gamma \int_{t_0}^t G_y(\tau) \, d\tau =: k_y(t). \quad (3.6)$$

Usually,  $\mathbf{k}$  and its components are simply referred to as *spatial frequencies*. Note that some authors use a different definition by scaling the left sides with  $\frac{1}{2\pi}$  (see e.g. Brown et al. [2014], Bernstein et al. [2004]). Assuming that the integral vanishes for the third term of equation 3.5 due to an inverse rephasing gradient as explained in section 3.3.2, equation 3.4 can be rewritten in the following form:

$$S_g(t) = S_g(k_x(t), k_y(t)) = \int_{\mathcal{S}} \int c(x, y) M_{\perp}(x, y) \Delta z e^{-\frac{t}{T_2^*}} e^{-i\mathbf{k}(t) \cdot \mathbf{x}} \, dx dy. \quad (3.7)$$

Equation 3.7 illustrates that the signal takes the form of a two-dimensional FOURIER transform of the weighted transverse magnetization. Since spins beyond the extents do

not contribute to the signal, the area of integration can be readily extended to infinity to match the proper definition of the transform. Thus, an inverse FOURIER transform is capable of mapping the desired distribution of  $M_{\perp}$  within the selected slice.

By modulating the spatial frequencies, i.e. varying the timing and strength of the gradient fields in equations 3.6, the measurement signals can be altered. In consequence, each measurement pass can be adjusted such that it corresponds to a different trajectory in  $\mathbf{k}$ -space, which is essentially a matrix to store the *raw data* of the measurement passes. Following the usual convention, the rows and columns correspond to different discrete values of  $k_y$  and  $k_x$ , respectively. With proper choice of the gradients' strength and timing it is possible to fill a line, or even multiple lines, in  $\mathbf{k}$ -space with each measurement pass. In fact, filling  $\mathbf{k}$ -space can be achieved with a vast variety of approaches, which lead to a multitude of advanced imaging methods, e.g. spiral imaging or techniques exploiting symmetry properties of  $\mathbf{k}$ -space. In the following, the explanations are restricted to the case of sequential, complete filling of  $\mathbf{k}$ -space along the Cartesian directions. This means that each pass fills one line in the  $k_x$ -direction, which is repeated for the number of points in one column, i.e. the number of points in the  $k_y$ -direction.

The simplified filling approach is performed by sampling the complex-valued measurement signals at discrete (equidistant) points in time  $t_i$ , which yields an (equidistant) spacing  $\Delta k$ . This spacing also reflects the smallest wave number and is inversely related to the *field of view* (FOV), i.e. the spatial extents  $E_x$  and  $E_y$  of the slice, by  $E_x = \frac{2\pi}{\Delta k_x}$  and  $E_y = \frac{2\pi}{\Delta k_y}$ . On the other hand, the resolution of the spatial image in terms of  $\Delta E_x$  and  $\Delta E_y$  is inversely related to the maximum value of the respective spatial frequencies,  $k_{x,max}$  and  $k_{y,max}$ , by  $\Delta E_x = \frac{E_x}{N_{p,x}} = \frac{\pi}{k_{x,max}}$  and  $\Delta E_y = \frac{E_y}{N_{p,y}} = \frac{\pi}{k_{y,max}}$ , where  $N_{p,x}$  and  $N_{p,y}$  denote the number of points (voxels) in the respective directions of the *image space* (Vlaardingerbroek et al. [2013]).

Thus, the dimensions of  $\mathbf{k}$ -space match the dimensions of image space. The  $k_x$ -dimension is defined by the number of sampling points in time, while the  $k_y$ -dimension corresponds to the number of measurement passes. With this fact in mind it is apparent that measurement time is largely determined by the  $k_y$ -dimension.

As mentioned at the beginning of this section, there is no one-to-one relation between the points or lines in  $\mathbf{k}$ -space and in image space. The data points rather depict the contributions of the spatial harmonics, whose wave lengths are specified by  $\frac{2\pi}{\|\mathbf{k}\|}$ , to the complete image (Vlaardingerbroek et al. [2013]). The harmonics with large wave lengths are located near the  $\mathbf{k}$ -space center and define the rough structure and the contrast of the image, whereas the finer structures are defined by the smaller wave lengths at the edges of  $\mathbf{k}$ -space (Siemens Healthcare GmbH [2015]).

This relationship of wave numbers and level of detail is illustrated in figure 3.3 (reprinted from Siemens Healthcare GmbH [2015]). On the left-hand side the  $\mathbf{k}$ -spaces corresponding to cranial images in the sagittal plane are depicted. The images on the right-hand side differ from each other depending on the segment of  $\mathbf{k}$ -space that is considered for image construction. Complete  $\mathbf{k}$ -space yields a high-contrast, sharp edged image, the sole center region generates a high-contrast, blurred representation, whereas the outer region results in the depiction of the missing sharp edges.

Understanding the concept and implications of  $k$ -space is of particular importance for the methodical approach. From this starting point the encoding of the remaining two spatial directions can be readily elucidated.

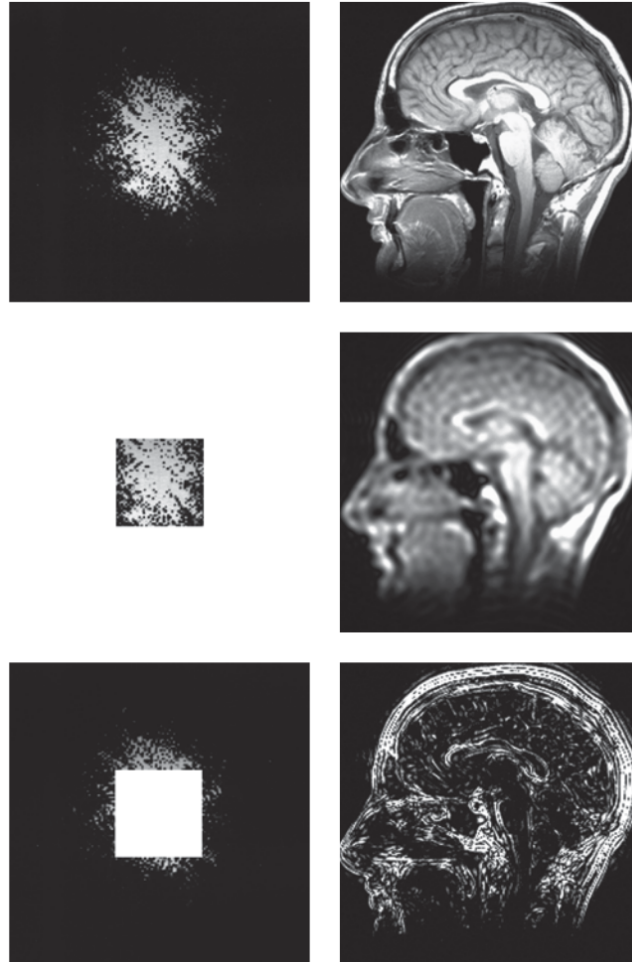


Figure 3.3: Relationship of wave numbers and level of detail using the example of cranial imaging. Reprinted from *Magnets, Spins, and Resonances: An introduction to the basics of Magnetic Resonance* (p. 118), by Siemens Healthcare GmbH, Erlangen, Germany: Siemens in-house publishing. Copyright 2015 by Siemens Healthcare GmbH. Reprinted with permission.

### 3.3.4 Spatial Encoding: Frequency Encoding

In order to fill one line of  $k$ -space, one must receive and sample a signal, for which each sampling corresponds to a different wave number  $k_x$ , while  $k_y$  remains constant. According to equations 3.6, this can be achieved by changing the time integral of the applied gradient  $G_x$ , which is automatically satisfied as time goes on. As long as this gradient strength in the  $x$ -direction is kept constant in time,  $k_x$  changes with linear

time dependence and each sample may serve as an entry in the raw data matrix. The magnetic gradient field is referred to as *frequency-encoding gradient* (FEG) or *readout gradient* since it is specifically applied during the execution of readout.

As the time period of readout is short compared to that of multiple measurement passes along the  $k_y$ -direction, the number of voxels in the  $x$ -direction, and thereby the resolution  $\Delta E_x$ , could be easily enhanced by obtaining more samples. However, nearly isotropic voxels are often favored and the number of voxels in both dimensions should match powers of two. Thus, doubling sampling frequencies quickly results in highly anisotropic voxels.

Note that placing the center of the magnetic gradient field, where the additional magnetic flux density due to the gradient vanishes, in the middle of the slice leads to a (HERMITIAN) symmetry of the spatial frequencies with respect to the  $\mathbf{k}$ -space center. Therefore, all spatial harmonics are covered twice, which allows for the aforementioned approximations that exploit this symmetric distribution for measurement acceleration. Furthermore, it should be mentioned that the gradient fields cannot be switched on or off instantaneously. According to FARADAY's law of induction, the rate of change in magnetic flux induces *eddy currents*, which may not only influence the components of the scanner system but also the measurement performed. Although the ramp associated with gradient field switching is of particular importance for many imaging sequences, it is often neglected in simplified descriptions. The definitions in equations 3.6 point out that the ramps directly influence the spatial frequencies in both encoding directions. The second of which is termed *phase-encoding* direction and the encoding approach is described in the following.

### 3.3.5 Spatial Encoding: Phase Encoding

Filling  $\mathbf{k}$ -space along the  $k_y$ -direction involves as many measurement passes as there are lines in the raw data matrix if one line is filled within each pass. The selection of the line to be filled relies on the adjustment of the spatial frequency  $k_y$ . In contrast to the  $k_x$ -direction the phase-encoded frequency must not change during the signal's readout. For this reason, the *phase-encoding gradient* (PEG)  $G_y$  is applied and ended before the readout starts. This corresponds to traversing  $\mathbf{k}$ -space from the center to the left edge of a specific line. The subsequent FEG and the concomitant readout enable the filling of the line. At the end of the relaxation process, the procedure can be repeated for the next line, i.e. the next spatial frequency  $k_y$ , by applying a gradient field of scaled strength until the matrix is completely filled.

In image space the method appears as less intuitive. Each measurement pass results in the registration of a measurement signal, which is generated by the complete slice, and each measurement pass uses a different gradient field strength  $G_y$ . Of course, the gradient field of a single pass results in a spatially dependent phase accumulation along the  $y$ -direction, which remains (temporarily) unchanged when the gradient field is switched off. In consequence, the signal of one measurement pass portrays a specific composition of phases. Due to their difference in gradient field strength, any two measurement passes must therefore reveal distinguishable compositions of phases. The multitude of compositions, combined with the information on the applied gradient field strengths, allow for a spatial allocation of the origin of the signals. As soon as the raw data matrix

is filled, i.e. after the *time of acquisition* TA, an inverse FFT may yield the image of the selected slice. Certainly, the image reconstruction becomes more involved when multiple receiving coils are used.

To establish order in the series of sequentially switched gradients, figure 3.4 (reprinted from Bushberg and Boone [2011]) may prove as an expedient overview. Note that an additional *rewinder gradient* is switched in phase-encoding direction and the FEG is extended. These two modifications are hardly relevant for the course of this thesis, and thus the explanation of their purpose is omitted to avoid confusion. However, the modifications bear significance in their exemplary nature since they illustrate that the actual pulse sequence design is more complex in practical applications. Depending on the measurement objective, contrast modification, selected  $k$ -space trajectories, the sequence of numerous consecutive RF pulses, i.e. the *pulse train*, and many additional factors, the GRE pulse sequence may be adapted to yield the required result.

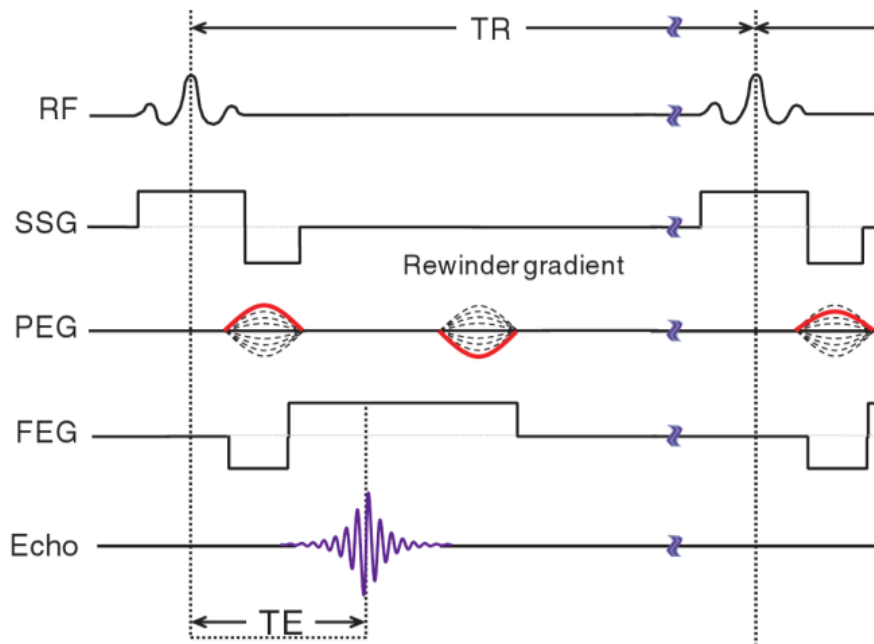


Figure 3.4: Simplified visualization of an exemplary GRE pulse sequence with a PEG rewinder and extended FEG duration. Reprinted from *The Essential Physics of Medical Imaging* (Third Edition, p. 454), by J.T. Bushberg and J.M. Boone, 2011, Philadelphia, USA: Wolters Kluwer Health. Copyright 2012 by Lippincott Williams & Wilkins. Reprinted with permission.

As indicated in section 3.3.2, the outlined technique can be extended to three dimensions in order to create volume encodings of slabs. For this purpose, the third dimension is identified as a further phase-encoding direction, which results in a three-dimensional  $k$ -space and hence in prolonged overall measurement times since each line of each layer of the data matrix has to be filled by a measurement pass. This fact elucidates the need for rapid acquisition techniques and methods that are capable of filling multiple lines

within each pass.

Finally, with the methodical basis unraveled the quantitative measurement of flow can be depicted.

### 3.3.6 Velocity Encoding

At first, recall that the appropriate encoding quantities of the measurement signal are given by frequency and phase, which already serve as resources for spatial mapping. Since the required velocity vector field necessitates an additional encoding step, further information must be extracted from the measurement signal. Again, this can be achieved by means of various approaches. The relevant approach for the course of this thesis is *phase-contrast* (PC) MRI and bases on the effect that moving spin ensembles accumulate different net phases depending on the affecting gradient fields and their velocity along the corresponding direction. In fact, this observation is already indicated by equation 3.3 when the ensemble's position  $\mathbf{x}$  is assumed to be time-dependent.

Expanding the time-dependent position vector into a TAYLOR series about the expansion point in time  $t_e$  and truncating the series after the second-order term leads to

$$\mathbf{x}(t) \approx \mathbf{x}(t_e) + \mathbf{v}(t_e)(t - t_e) + \frac{1}{2}\mathbf{a}(t_e)(t - t_e)^2, \quad (3.8)$$

where  $\mathbf{a}$  is the acceleration of the fluid element containing the spin ensemble. This approximation is supported by KOUWENHOVEN et al., who have stated that the time derivatives on the order of jerk and of higher order can be neglected (in the case of *bipolar gradients*) for all practical applications (Kouwenhoven et al. [1995]). For the sake of simplicity, it is assumed that local magnetic field inhomogeneities, e.g. due to susceptibility variations, can be neglected. Furthermore, the contribution due to acceleration is neglected, which is a simplistic assumption of the applied model and is reconsidered in section 5.2.

Substituting equation 3.8 into the definition of the phase accumulation 3.3, restricting the considerations to a gradient field applied along the  $x$ -direction and fixing  $t_e = 0$  leads to

$$\varphi(\mathbf{x}, t) \approx x(0)\gamma \int_{t_0}^t G_x(\tau) d\tau + u(0)\gamma \int_{t_0}^t G_x(\tau)\tau d\tau = x(0)\gamma m_0 + u(0)\gamma m_1, \quad (3.9)$$

where  $m_0$  and  $m_1$  denote the *zeroth-order* and *first-order gradient moment*, respectively. This shows that the phase accumulations of moving spin ensembles additionally depend on their velocities as well as on the *gradient waveform*, which refers to the timing and strength of the applied gradient fields. *Velocity-compensated* gradient waveforms, where  $m_1 = 0$  but  $m_0 \neq 0$ , can be designed by means of combinations of bipolar gradients. The appropriate gradient waveform involves the switching of gradients of reversed polarity such that the first-order gradient moment vanishes at the time of readout (Schmitter and Schnell [2018]).

However, the induced phase accumulation due to the flow of the spin ensemble can also be interpreted as a source of information when it is contrasted with the velocity-compensated measurement or, more generally, with another measurement performed with a different first-order gradient moment. In general, the difference of the first-order

### 3 Materials and Methods

moments  $\Delta m_1$  of two flow-encoding acquisitions where the zero-order moments are equal (at the time of readout) linearly relates the velocity along the gradient direction to the observed phase accumulation difference. This holds for the phase difference of each pixel (Pelc et al. [1991a]), and can be expressed as

$$\Delta\varphi(\mathbf{x}) = u(\mathbf{x})\gamma\Delta m_1. \quad (3.10)$$

The subtraction of phase accumulations also enables the elimination of background phase contributions both images share (Markl et al. [2012]). For this reason, two subsequent measurements with non-zero  $\Delta m_1$  are sufficient to quantify unidirectional velocities. For the determination of the velocity vector field with its three components within a slice (2D3C) or a volume (3D3C), four measurements would suffice when, for example, the phase accumulation of the first measurement is considered as the reference phase for the three remaining measurements. This particular method of four acquisitions is referred to as simple *four-point encoding* (Pelc et al. [1991b]).

Since the turbulent flow under consideration is investigated on the basis of its time average, as explained in section 2.6, proximity in time of the individual componentwise acquisitions is not mandatory. Therefore, the three velocity components of each case are measured in three separate sessions, which corresponds to six measurement cycles and implies the assumption of time invariance of the mean flow. This approach allows for (almost) equal time delays between the reference measurement and the respective acquisitions of the velocity components.

As  $\Delta\varphi$  is bounded by  $\pm\pi$ , an encoding restriction is required in order to allow for distinguishable velocities on the given interval. The restriction is imposed by the *velocity encoding* value  $v_{enc}$  following

$$v_{enc} = \frac{\pi}{\gamma|\Delta m_1|}, \quad (3.11)$$

which has to be chosen higher than the expected maximum velocity magnitude along the respective direction to ensure the absence of *aliasing*. However, since *velocity noise* scales with  $v_{enc}$  according to the equation

$$\sigma_v = \frac{2 v_{enc}}{\pi S_R}, \quad (3.12)$$

where  $\sigma_v$  is the velocity noise and  $S_R$  denotes the SNR of the magnitude image,  $v_{enc}$  should not be chosen exceedingly high (Schmitter and Schnell [2018]). Equation 3.12 also implies that the validity of the quantitative measurements is impaired by increasing dynamic ranges of the velocity component field. In general, the *velocity distribution* of turbulent flows inside a voxel compromises the measurement signal and leads to a reduced SNR.

In order to overcome the problem of low SNR in turbulent flows, the MRV experiments within this thesis are carried out by taking the (time) average of multiple acquisitions. The implications of this approach, along with a short summary of the selected methods, are delineated in the following.

### 3.3.7 MRV Specifications

The time-averaged MRV experiments are conducted for the three selected cases described in section 3.2.2. In addition to the  $u$ - and  $v$ -component of the velocity obtained from PIV measurements, the  $w$ -component in the respective plane (2D3C), i.e. the coronal plane, is determined for all cases. Further measurements of selected components are performed on transverse planes and on planes that are rotated away from the coronal plane by particular azimuthal angles  $\phi$ . The latter measurements are used to generate an azimuthal average, which implies an additional spatial average of the time averages of the individual measurements. This approach bases on the predefined assumption of rotational symmetry of the velocity components.

Slice selective, non-triggered PC GRE sequences are applied on anisotropic voxels with spatial extents of  $0.75 \text{ mm} \times 0.75 \text{ mm} \times 4 \text{ mm}$  or  $0.75 \text{ mm} \times 0.75 \text{ mm} \times 1 \text{ mm}$  depending on the given case. Here, the last value indicates the slice thickness, which will be specified for the particular cases in chapter 4. The filling of  $\mathbf{k}$ -space is performed along the Cartesian directions where each measurement pass is applied to fill a single line. The readout direction is chosen as the  $x$ -direction for all measurements in the coronal plane or its rotated equivalents. For the case of transverse measurements the  $y$ -direction is chosen. The value of  $v_{enc}$  is individually determined on the basis of preliminary tests with a small number of averaged images and adjusted to approx. 150% of the observed maximum velocity value. Values of the selected  $v_{enc}$  range from  $1.5 \text{ m s}^{-1}$  to  $4.5 \text{ m s}^{-1}$ . 1000 images are averaged to obtain the mean velocity fields of the coronal planes. For the remaining cases, i.e. measurements in rotated or transverse planes, the number of averages varies and is specified for the depicted results in chapter 4. Additional parameters of the MRV experiments are listed in Appendix C.

It has to be emphasized that the validity of data obtained in such a manner relies on certain properties of the investigated velocity field. Recall from section 2.6 that the averaging procedure has to fulfill the conditions of the REYNOLDS operator. The outlined theory concerns a large number of averaging samples where each sample covers the complete ROI. While this is correct for the case of PIV snapshots, the MRV data are acquired in a sequential fashion. Any two lines in  $\mathbf{k}$ -space are acquired at different times, and thus the transformed velocity field in image space reflects a state of the flow that is given by the superposition of spatial harmonics at different points in time, which is not exactly the definition of a snapshot. This limitation leads to a further assumption in addition to the requirements of the averaging procedure. In the following, it is assumed that due to the comparatively large number of samples each line in  $\mathbf{k}$ -space is obtained at arbitrary flow states and that all lines share a comparable set of obtained flow state acquisitions at the end of the measurement.

After the acquisition the measurement data are automatically averaged and transformed to grey level phase- and magnitude images by the scanner operation system. The raw phase images reveal noise in the areas where no signal is detected, either because of the loss of signal or because of the absence of signal due to the lack of water. With the additional geometrical information provided by the magnitude image, preliminary flow fields are generated using MATLAB®. By declaring noise-dependent acceptance threshold values for the respective magnitude images, a straightforward signal filter is created, which by element-wise multiplication serves as an applicable indicator for areas

of valid flow in the noisy phase image. Eventually, the required velocity field is obtained via the mapping to  $\pm\pi$  and the subsequent scaling by the given  $v_{enc}$ .

Two further remarks shall be made at this point. Firstly, the generated velocity field appears distorted due to magnetic field inhomogeneities and gradient field nonlinearities (Walker et al. [2014]). The operation system allows for an automatic *distortion correction* option. If the option remains unselected, the correction has to be postponed to the post-processing. Secondly, since the sign of the flow depends on the definition of the axes within the operation system, for some cases the correct orientations of the measurement plane axes have to be specified during post-processing as well, which is especially important for the application of the azimuthal average.

In a final step, azimuthal averaged MRV data and corresponding PIV data are utilized for the calculation of stability and POD modes, respectively. The specifications of these approaches are the subject of the next section.

### 3.4 POD and LSA Specifications

5000 PIV snapshots of the base case (Re20000\_dj0\_br575) experiments are used to perform the POD in MATLAB<sup>®</sup>. The evaluation is restricted to the  $v$ -component of the snapshots, and  $N_m = 40$  is specified beforehand. Except for the cropping during the process of PIV evaluation (see section 3.2.2) the ROI remains as the untrimmed velocity field. The first two modes are of particular interest. These constitute a complex conjugate pair that are combined as the real and imaginary part of a single mode. Computationally adjusting the phase angle of this mode eventually allows for an approximate matching to the phase angle of the instability mode.

Global LSA is undertaken for the temporal and azimuthal average of the base case's velocities fields, which are obtained from MRV experiments as follows: The measurement slices are chosen such that they span from  $\phi = 0^\circ$  to  $\phi = 165^\circ$  in  $15^\circ$  increments and cover the complete cross sectional area. Taking account of the possible sign change, all slices are divided in axisymmetric halves that are subsequently fused to an average field of the bisected central swirler cross section. This is carried out for the  $u$ -,  $v$ - and  $w$ -component, which are thus given with respect to the predefined cylindrical coordinate system. The number of averages per slice is 100, which yields 2400 averages in total for the combined, bisected cross section. Subsequently, the ROI is trimmed with respect to the axial direction such that the  $x$ -extents reach from  $-2\frac{x}{D}$  to  $5\frac{x}{D}$ . Two-dimensional mesh creation is accomplished using Gmsh (release 4.4.0) (Geuzaine and Remacle [2009]). The mesh includes a refinement region in the proximity of the mixing tube's outlet and consists of 11 207 triangles. The interpolation of the mean velocity fields on the mesh, subsequent discretization of the equation system that is linearized around the base flow (mean flow), and the solution of the GEVP is achieved by the use of an in-house solver (*felics code*). The solver is based on continuous GALERKIN finite elements, where second-order elements for the velocity component fields and first-order elements for the pressure field are used. Following the approach outlined in section 2.8, the effective REYNOLDS number is estimated by  $Re^* = 150$  (see equations 2.53 and 2.54), the azimuthal wave number is set to  $m = 1$  and the real part of the angular frequency is assumed to be located between

### 3 Materials and Methods

3.7 and 4.4. The latter approximation bases on the STROUHAL number (see 2.28), which is estimated to be  $0.6 < St < 0.7$ , and the relation  $\omega_r = 2\pi St$ . The boundary conditions are set according to table 3.4. Only the radial mode of the applicable eigenvalue (inside the assumed interval) is then concerned for the comparison with the chosen POD mode.

Symmetry axis	Inlet/Outlet	Walls
$\hat{u} = 0$	$\hat{u} = 0$	$\hat{u} = 0$
$\frac{\partial \hat{v}}{\partial \rho} = 0$	$\hat{v} = 0$	$\hat{v} = 0$
$\frac{\partial \hat{w}}{\partial \rho} = 0$	$\hat{w} = 0$	$\hat{w} = 0$
$\hat{p} = 0$	$\hat{p} = 0$	$\frac{\partial \hat{p}}{\partial n} = 0$

Table 3.4: Boundary conditions of the global LSA specified for the three types *Symmetry axis*, *Inlet/Outlet* and *Walls*

The abovementioned specifications of the POD and global LSA conclude the chapter on materials and methods. In the following the experimental results of the three selected cases, i.e. *swirling flow without injector jet* (base case), *swirling flow with injector jet* and the *sole injector jet*, are presented and compared. Furthermore, the results of the two modal decomposition techniques are depicted and evaluated.

## 4 Results

The results are presented as follows: PIV and MRV data of the  $u$ - and  $v$ -component are depicted and compared within their respective measurement planes, where the PIV cross-sectional plane is regarded as equivalent to a section of the coronal plane. Additionally, velocity fields on selected transverse planes from MRV data are attached to provide further insight and illustrate the capabilities and limitations of this measurement technique. A comparison of the  $w$ -component fields of the first two cases follows. At last, the results of the POD and the global LSA are provided.

It is important to mention that the ranges of the colorbars in the major part of the following figures do not cover the full range of the measured velocities but are chosen as compromises between contrast and velocity ranges. Furthermore, note that all velocity fields are normalized by the bulk velocity  $v_0$ , unless otherwise stated, and that all axes are normalized by the diameter of the mixing tube  $D$ .

### 4.1 Base Case: Swirling Flow without Injector Jet

Figure 4.1 depicts the obtained axial velocity measurement results of the base case (*Re20000\_dj0\_br575*), where (A) and (C) depict the velocity fields within the coronal plane from MRV and PIV data, respectively. A qualitative assessment based on a first visual inspection yields the impression of excellent agreement within the according sections. The CRZ and the outer recirculation zone (ORZ) are clearly recognizable in both measurement. A central area of increased velocity stretches from the downstream end of the CRZ along the flow axis to the downstream end of the measurement section. Similar flow is vaguely identifiable at the outer *confinements of the combustion chamber* (CCC).

Discrepancies are found for the thickness of the swirling jet in the combustion chamber's upstream region. However, both MRV and PIV data show an asymmetric pattern, where the left jet branch appears with decreased velocities, e.g. between  $\frac{x}{D} \approx 0.5$  and  $\frac{x}{D} \approx 1$ , and reduced thickness as compared to the right.

The most salient contrast between the two velocity fields is the difference in smoothness. PIV data show smooth gradations, whereas MRV data appear pixelated and reveal noisy outliers, e.g. at the outer CCC and mixing tube, at the CCC at  $\frac{x}{D} = 0$  and alongside the upstream end of the mixing tube ( $\frac{x}{D} \approx -2.1$ ). The latter can probably be ascribed to small amounts of water between the blocking ring and the swirler. There is an apparent increase in outliers near the right CCC compared to the left-hand side. Explanations for the difference in smoothness are found in the increased resolution of the PIV experiments as compared to the MRV experiments (approx.  $0.4 \text{ mm} \times 0.4 \text{ mm}$  vs. approx  $0.75 \text{ mm} \times 0.75 \text{ mm}$ ) and in the increased number of PIV averaging samples (10 000 vs. 1000).

Besides the comparative evaluation, the extended FOV of MRV data allows for further

## 4 Results

assessment of the flow field inside of the mixing tube. Clearly, due to the strong swirling motion the large portion of axial flow is pressed against the wall of the mixing tube, leaving a region of reduced axial velocity close to the axis. In fact, a small center region of reversed flow appears at  $\frac{x}{D} \approx -2$ . *Flow voids* occur at the mixing tube walls close to the vane outlets, where the flow is rather abruptly redirected.

Two further observed measurement limitations have to be mentioned. At first, the shape of the downstream flow field indicates that the aforementioned correction function (see section 3.3.7) could not ideally compensate for the distortion of the field distal from the isocenter, which is located at  $\frac{x}{D} \approx 1$ . The second important observation is the small area of seemingly reversed flow on the outer side of the left shear layer. Elevated noise at this location of increased velocity gradients can account for this misinterpretation but aliasing cannot be ruled out with certainty.

Velocity profiles, normalized by the bulk velocity, at  $\frac{x}{D} = 2.5$ ,  $\frac{x}{D} = 1.5$  and  $\frac{x}{D} = 0.5$  are depicted in the subplots (D), (E) and (F), respectively, for both PIV and MRV data. The profiles of both measurement techniques show a remarkable agreement, except for a peak velocity discrepancy of the jet branches at  $\frac{x}{D} = 0.5$ . Apart from that, there is a slight difference in slope at  $\frac{x}{D} = 0.5$  and  $\frac{y}{D} \approx 0.3$ , a marginal increase in reversed flow of MRV data close to the walls at  $\frac{x}{D} = 0.5$  and a slight difference in forward flow at  $\frac{x}{D} = 2.5$  and  $\frac{y}{D} \approx -0.1$  as well as close to the walls.

At last, subplot (B) depicts the axial velocity field in the transverse plane fixed at  $\frac{x}{D} \approx -2.5$  ( $N_s = 1000$ ). This slice is chosen to gain insight into the complex flow field at the swirler vane inlets and inside of the mixing tube's upstream end, where application of PIV is hardly feasible. Although PIV data are not available for comparison, some interesting observations can be made. There is an area of flow void downstream of the frustum of a cone, probably due to turbulent phase dispersion and its resulting signal loss. Another point is that the flow signal at the vanes shows enhanced misregistration such that the segments between the vanes appear out of shape. Moreover, the outer region of the transverse plane reveals an unexpected pattern. Slow reversed flow appears to be at the upper left quadrant, whereas slow forward flow appears to be at the lower right quadrant. Finally, a stationary air bubble is located at the upper edge, characterized by the complete absence of signal within this area.

## 4 Results

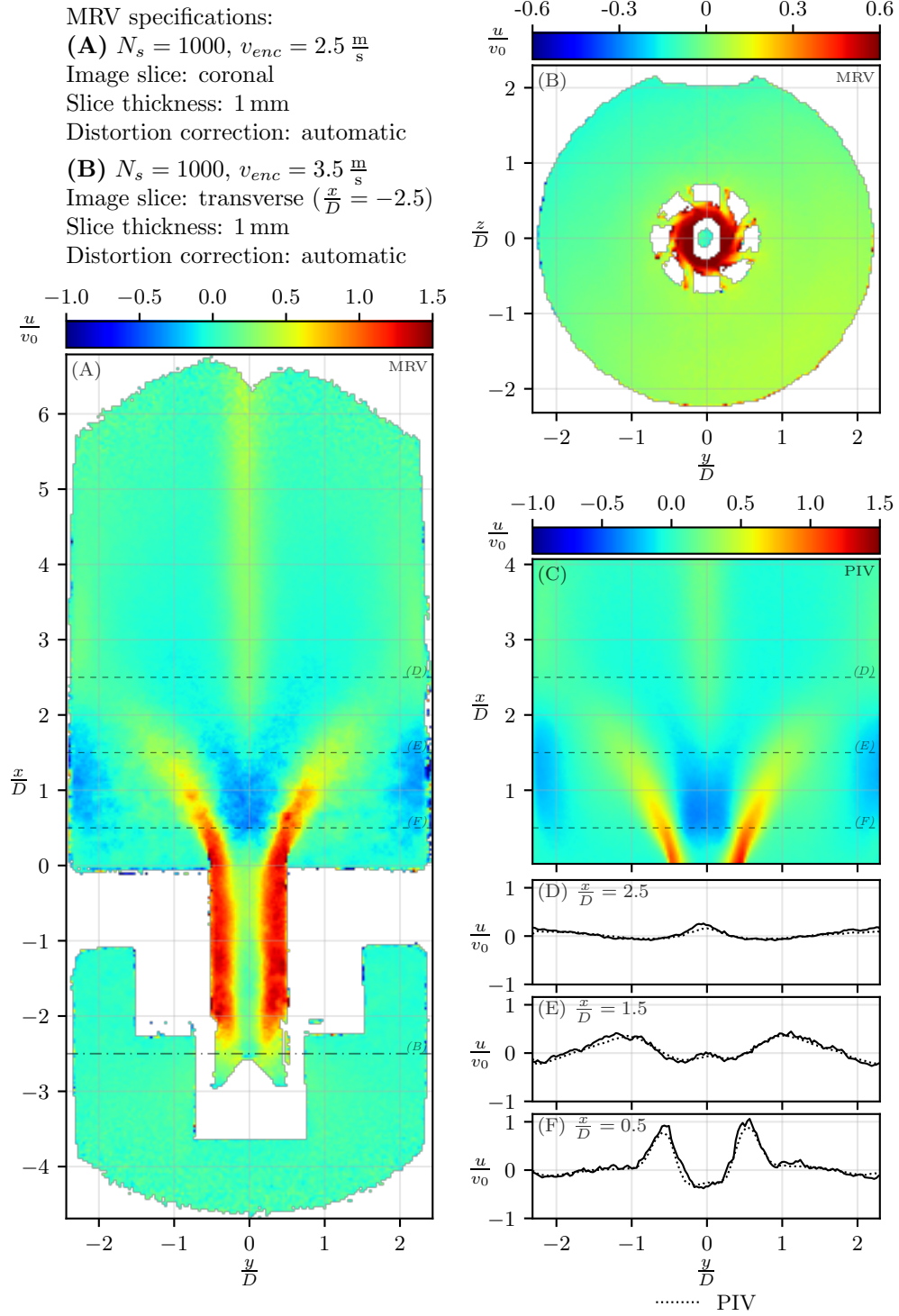


Figure 4.1: Axial velocity field comparison of the case: swirling flow without injector jet; (A) MRV, coronal plane (B) MRV, transverse plane (C) PIV, coronal plane (D)-(F) MRV and PIV velocity profiles from (A) and (C) at  $\frac{x}{D} = 2.5$ ,  $\frac{x}{D} = 1.5$  and  $\frac{x}{D} = 0.5$

## 4 Results

The comparison of the transverse velocity component, i.e.  $v$  (along the  $y$ -direction), of the respective base case measurements is depicted in figure 4.2 in the same arrangement and with the same specifications as given for the axial velocity field before. MRV data reveal a conspicuous discrepancy at the mixing tube's outlet as compared to PIV data. Moreover, this discrepancy in MRV data pervades the entire length of the mixing tube in the form of asymmetric streaks. Apart from that, the shared FOV of both PIV and MRV exhibits reasonable agreement. The branches of the swirling jet are similar in shape and transverse velocity magnitude. However, the velocities obtained from PIV appear to be slightly lower and especially the right branch shows decreased thickness. Both data sets clearly depict the ORZ. Again, the shape is similar but a slight velocity excess is present in MRV data, especially close to the CCC at  $\frac{x}{D} = 0$ . The excess in velocity is even more prominent when regarding the central, asymmetric whirl that stretches from the CRZ to the downstream end of the respective measurement sections. In fact, the mere occurrence of this whirl is a noticeable, and to some degree unexpected, result.

As outlined before in the case of the axial velocity component, measurement limitations such as noise at the CCC, degraded smoothness, minor flow voids (e.g. at  $\frac{x}{D} \approx -2.1$ ) and misregistrations (e.g. at  $\frac{x}{D} \approx -2.1$  and  $\frac{x}{D} \approx -0.1$ ) are found in the FOV of MRV data. Furthermore, the pattern of seemingly increased or decreased velocities dependent on the measurement quadrant (see figure 4.1,(B)) is detectable at the upstream and, though less notable, the downstream end of the FOV in (A).

The transverse slice depicted in (B) gives further insight into the flow field at the mixing tube's inlets ( $\frac{x}{D} \approx -2.5$ ). The flow void in the center region, the air bubble and the misregistrations at the vane segments again appear as an undesirable measurement impairment. In addition, there is a discrepancy between the transverse velocity field of the coronal and the transverse slice. While the coronal measurement depicts positive transverse velocities inside and outside of the mixing tube at  $\frac{x}{D} \approx -2.5$  and  $\frac{y}{D} < 0$ , the transverse slice reveals positive (outside) and negative (inside) transverse velocities at the same area. Of course, the same holds true for  $\frac{y}{D} > 0$  with all signs changed. In contrast, the expected result would rather show transverse velocities, which are close to zero along the line  $\frac{z}{D} = 0$ . Perhaps, the red and blue twin pattern in (C) can be assumed to be rotationally displaced in the clockwise direction.

At last, the velocity profiles extracted from (A) and (C) further illustrate the former findings. At  $\frac{x}{D} = 2.5$  the profiles of MRV and PIV data are in good agreement, except for the dent caused by the whirl, which is markedly pronounced in MRV data but almost vanishes in PIV data. At  $\frac{x}{D} = 1.5$  no such dent can be found in the profile of the PIV measurements. Furthermore, the profiles show less congruence for  $\frac{y}{D} > 1$ . Contrasting that, the the profiles at  $\frac{x}{D} = 0.5$  are mostly in good agreement, except for the region close to the mixing tube's outlet, where the abovementioned discrepancy leads to a deviating flow in MRV data as compared to PIV data.

## 4 Results

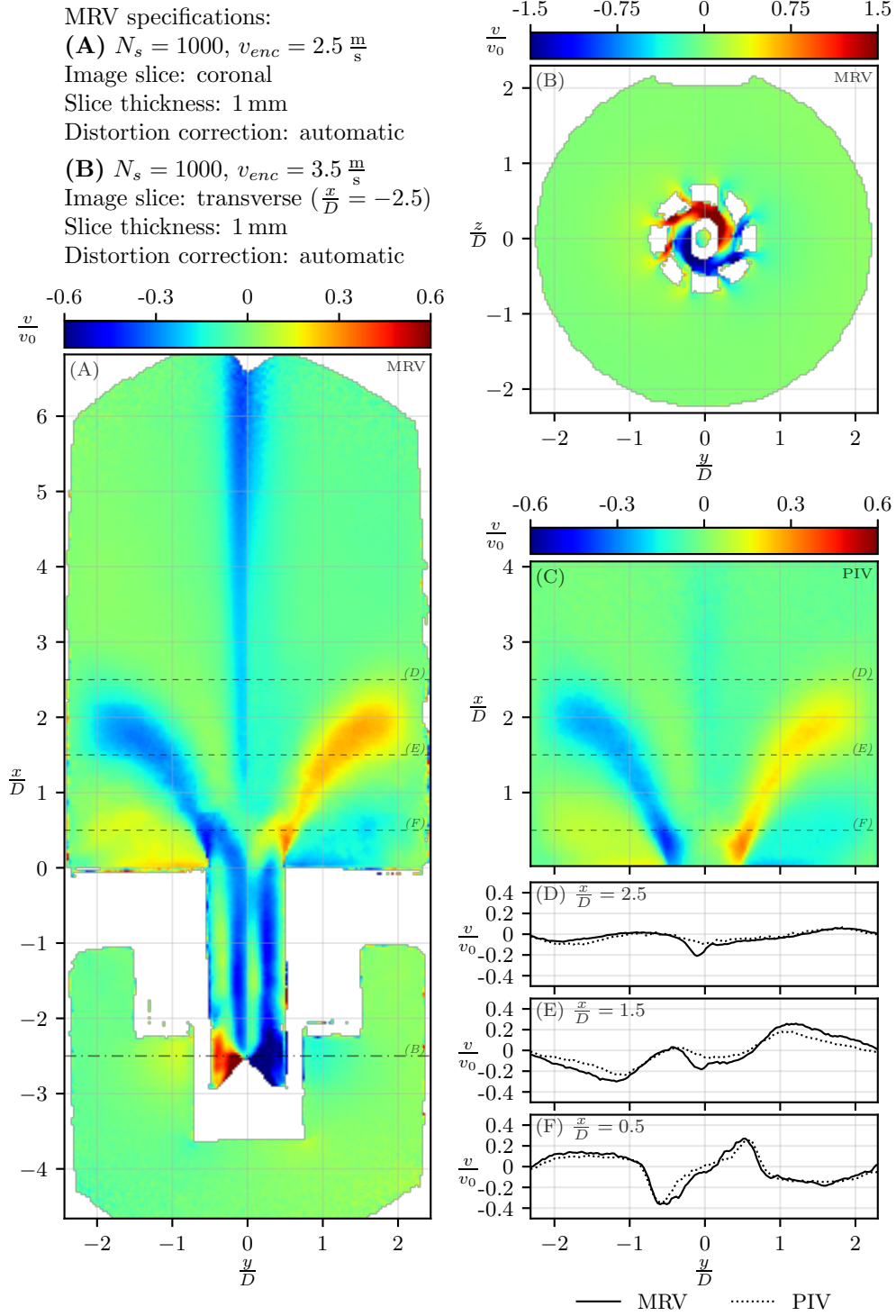


Figure 4.2: Transverse velocity field comparison of the case: swirling flow without injector jet; (A) MRV, coronal plane (B) MRV, transverse plane (C) PIV, coronal plane (D)-(F) MRV and PIV velocity profiles from (A) and (C) at  $\frac{x}{D} = 2.5$ ,  $\frac{x}{D} = 1.5$  and  $\frac{x}{D} = 0.5$

## 4.2 Swirling Flow with Injector Jet

The results of the axial velocity fields of the second case (*Re20000\_dj96\_br575*) are compared in figure 4.3, where (A) and (B) picture the MRV results within the coronal slice and the transverse slice at  $\frac{x}{D} \approx -0.7$ , respectively, and (C) depicts the velocity field obtained from PIV. Again, the qualitative visual evaluation yields the impression of striking resemblance. The inner, flame-shaped, yellow and the outer, turquoise contour appear similar in shape and axial velocity magnitude. A difference in shape, however, exists at the downstream end ( $\frac{x}{D} \approx 2.2$ ) of the emanating jet. Furthermore, PIV data reveal an asymmetry, which is not found in MRV data, as the left side of the flame-shaped, yellow region appears to be reduced in width.

Further inspection of the extended FOV of the MR measurement gives rise to three considerable observations. Firstly, although there still is image quality impairment, the misregistrations and noise effects at the CCC appear as less severe. Note that for the given case the slice thickness is set to 4 mm and the automatic distortion correction is not activated. Instead, the correction of the coronal slice data is performed during post-processing. These two alterations may contribute to the impression that signal noise seems to be reduced as compared with the base case measurements on the one hand but, in spite of that, the pipe confinements have a jagged shape along (almost) the entire surface on the other hand. Moreover, the manual distortion correction results in a FOV stretching that intensifies with increasing distance from the isocenter. For example, the upstream end of the swirler geometry at  $\frac{x}{D} \approx -3.9$  appears shifted as compared to that depicted in figures 4.1 and 4.2, where the respective confinements are located within  $-3.7 < \frac{x}{D} < -3.6$ .

Secondly, signal noise at the upstream and downstream end of the FOV is more prominent than in the base case measurements. However, this feature largely depends on the threshold value selected for post-processing, which is significantly smaller in this case as compared to the coronal measurements of the base case.

Thirdly, the flow inside the injector, which is actually cylinder-shaped, exhibits major *artifacts*. Close to the upstream orifice the velocity is substantially decreased and flow voids occur to both sides, yielding the impression of a flow constriction.

Subplots (D)-(F) illustrate the velocity profiles from (A) and (C) at the indicated positions. While (D) and (E) are in excellent agreement, there is a slight discrepancy in (F). Velocities obtained from PIV are below those obtained from MRV for  $-0.5 < \frac{y}{D} < 0.5$ . The asymmetric shape detected in (C) is confirmed by the dotted velocity profile. However, although not clearly observable in (A), MRV data exhibit a comparable asymmetry. This might be indicative for a constructional imperfection of the swirler geometry.

The axial velocity field in the transverse slice fixed at  $\frac{x}{D} \approx 0.7$  is depicted in subplot (B). The probably most salient aspect of this measurement is its pixelated appearance. Despite the inadequate resolution and the comparatively low number of averages ( $N_s = 128$ ), the profile of the jet within the mixing tube is reasonably identifiable and corresponds to the results depicted in (A) at  $\frac{x}{D} \approx 0.7$ .

## 4 Results

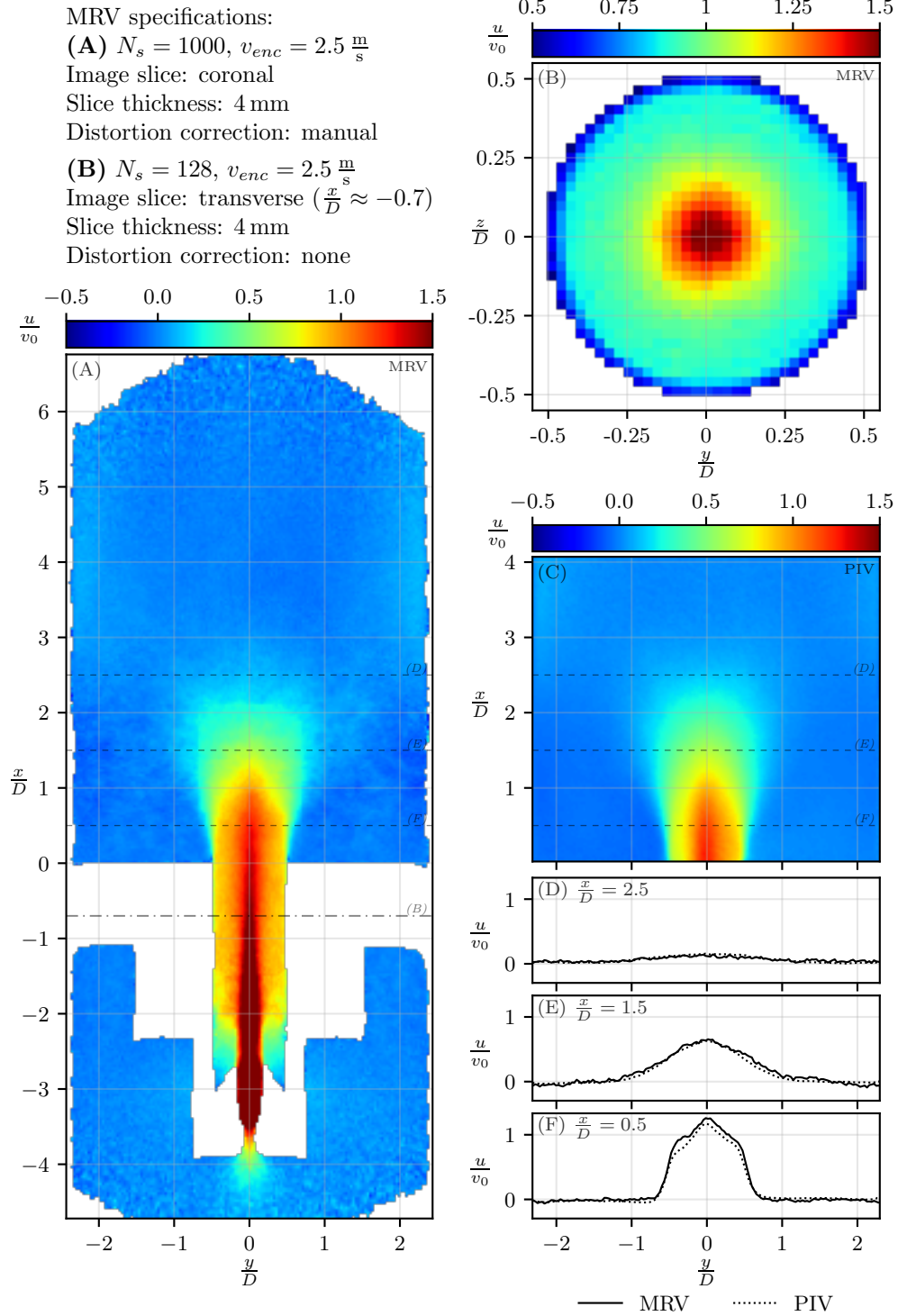


Figure 4.3: Axial velocity field comparison of the case: swirling flow with injector jet; (A) MRV, coronal plane (B) MRV, transverse plane (C) PIV, coronal plane (D)-(F) MRV and PIV velocity profiles from (A) and (C) at  $\frac{x}{D} = 2.5$ ,  $\frac{x}{D} = 1.5$  and  $\frac{x}{D} = 0.5$

## 4 Results

The fourth set of measurement results relates to the transverse velocity field of the swirling flow with injector jet. The slice specifications are identical to those of the abovementioned investigation of the axial velocity field. Coronal MRV data and PIV data, depicted in (A) and (C) are in acceptable agreement, albeit enhanced shortcomings concerning the branch shapes of the swirling jet. These seem to be more stretched in the axial direction in PIV data as compared to MRV data. Additionally, the transverse velocity magnitudes, especially within the right branch, are less pronounced in PIV data. This also holds for the ORZ. However, the areas of increased inward-facing velocity at  $\frac{x}{D} \approx 0$  are similar in both measurements.

Regarding the shared FOV of both measurements, the major discrepancy is certainly found to be the asymmetric pattern at the mixing tube's outlet. Unlike the transverse velocity field of the base case (see figure 4.2), where four streaks pervade the mixing tube and cross the centerline, the flow inside the mixing tube of figure 4.4,(A) appears axisymmetric in shape though asymmetric in transverse velocity magnitude, i.e. the velocity values in the mixing tube seem to be shifted towards negative velocities. Moreover, the pattern of positive velocities in the corners of the second and fourth quadrant that are distal from the isocenter contrasting negative velocities in the first and third quadrant is again recognizable. Due to the small velocity range the pattern appears yet more pronounced. Increased flow voids at the mixing tube inlets and around the injector orifice are found as compared to the axial velocity measurement depicted in figure 4.3),(A). Apart from these flow voids the comparison with the axial velocity field shows that the transverse field is cropped at the upstream and downstream end as well as less jagged at the pipe confinements. This effect is mainly accounted for and can be compensated by the threshold parameter that acts as the simplified noise filter function. The velocity profiles extracted from MRV and PIV data at  $\frac{x}{D} = 2.5$  and  $\frac{x}{D} = 1.5$  (subplots (D) and (E)) are in good agreement. However, the slight differences in slope at the center region and in magnitude closer to walls confirm the qualitative observations from (A) and (C) regarding the difference in shape mentioned above. Subplot (F) depicts the profiles at  $\frac{x}{D} = 0.5$ . A slight, almost constant velocity excess occurs for  $\frac{y}{D} < -0.2$  and  $\frac{y}{D} > 2$ . The major discrepancy is, however, the dent at  $-0.2 < \frac{y}{D} < 0.5$  that is caused by the asymmetric pattern in MRV data.

The transverse velocity field in the transverse slice at  $\frac{x}{D} \approx -0.7$  (subplot (B)) completes the comparison of the second set of results. Note that the number of samples is chosen inadequately low ( $N_s = 32$ ). Still, the obtained result within the mixing tube is remarkable. At first, the velocity fields in the transverse slice and in the coronal slice are in conflict. At  $\frac{z}{D} \approx 0$ , which corresponds to the field depicted in the coronal slice, the velocity profile appears to be symmetric. This is in contrast to the data given in (A). In addition, the transverse velocity magnitudes at  $\frac{z}{D} \approx 0$  in the transverse slice significantly exceed the values indicated by the coronal slice data, especially for  $\frac{y}{D} < 0$ . At last, the twin pattern in (C) again yields the impression of being rotationally shifted in the clockwise direction.

## 4 Results

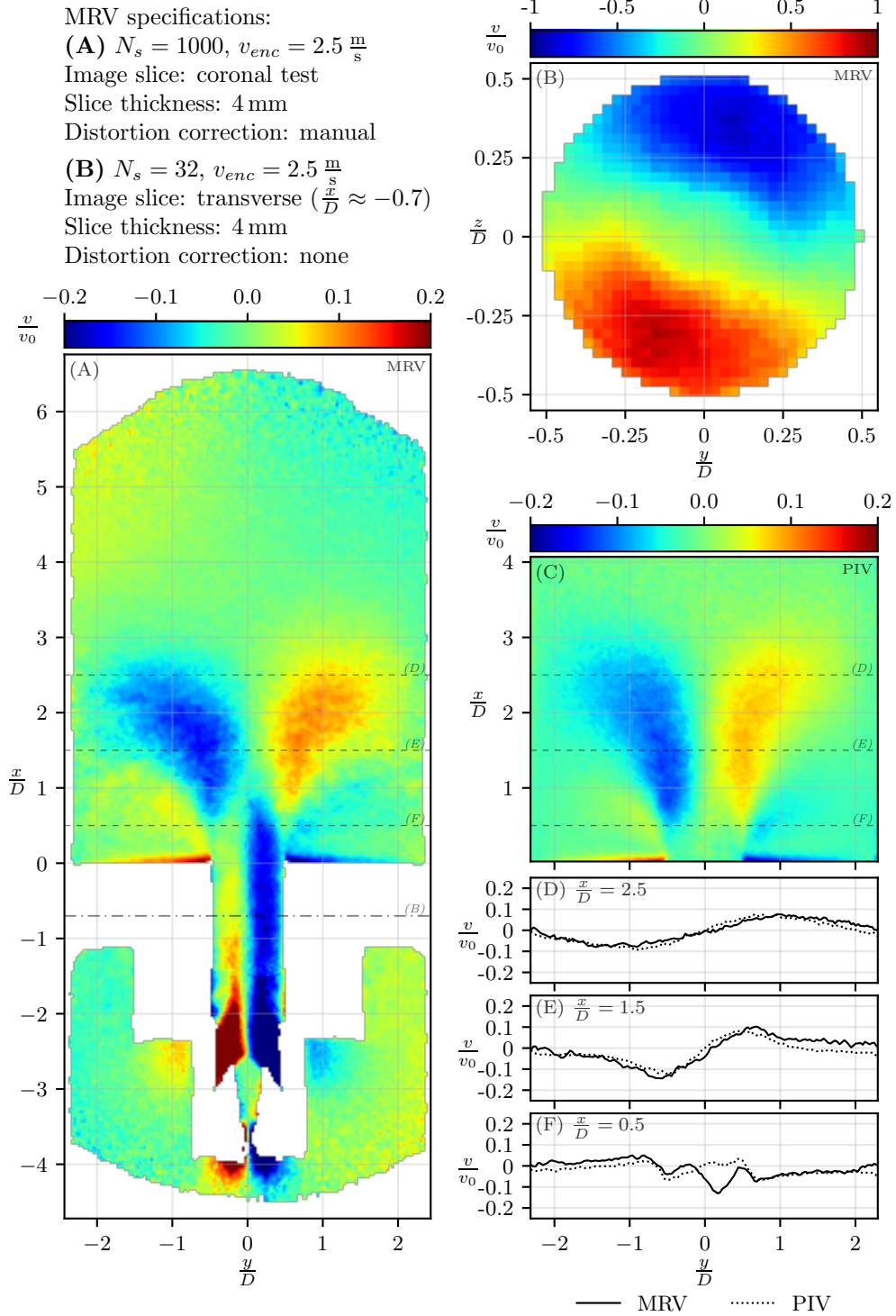


Figure 4.4: Transverse velocity field comparison of the case: swirling flow with injector jet; (A) MRV, coronal plane (B) MRV, transverse plane (C) PIV, coronal plane (D)-(F) MRV and PIV velocity profiles from (A) and (C) at  $\frac{x}{D} = 2.5$ ,  $\frac{x}{D} = 1.5$  and  $\frac{x}{D} = 0.5$

### 4.3 Sole injector jet

For the third part of the comparative analysis of the results, figure 4.5 depicts the axial velocity field of the sole injector jet case. Recall that the REYNOLDS number of this case is set to 10 000 and the vanes of the mixing tube are sealed. Also note that the velocity field acquisition is performed on a set of slices as outline in section 3.3.7. The increment of the rotation angle  $\phi$  starting from the coronal plane is  $15^\circ$ , though the slices at  $\phi = 15^\circ$  and  $\phi = 90^\circ$  are omitted due to stationary air bubbles that may impair image quality.

As before, the first step of the comparison involves the qualitative comparison of the shared FOV of subplots (A) and (C). The sole injector jet reveals a substantial mismatch regarding the axial velocity at the region close to the centerline. For this region it appears that the axial velocity values obtained from PIV data amount to approx. two-thirds of the values obtained from MRV data. The discrepancy is clearly illustrated by the difference in shape and color between (A) and (C). In order to evaluate the results regarding their individual shapes and to estimate whether the assumed scaling factor is constant throughout the FOV, the velocity profiles (D)-(F) are fitted by scaling PIV data such that  $u^f = \frac{3}{2}u$ , while MRV profiles remain unaltered. Indeed, the (fitted) peak velocities of both profiles match reasonably well for all three axial positions. However, as indicated by the jet center offset depicted in (C), the PIV profiles exhibit an asymmetric shape, where the tendency to the left side is particularly recognizable at  $\frac{x}{D} = 0.5$ . The profiles at  $\frac{x}{D} = 1.5$  and  $\frac{x}{D} = 2.5$  may indicate a slight streamwise attenuation of this effect.

Reconsidering the extended FOV of the MRV acquisition yields the observation that the vanes become visible due to the azimuthal average. On the left-hand side, close to the projected vane slots, a flow void region appears. Further flow voids occur within the mixing tube to both sides of the injector jet ( $-2.3 < \frac{x}{D} < -1.5$ ) and at the injector orifice ( $-3.6 < \frac{x}{D} < -3.1$ ). At least the latter are accompanied by severe velocity measuring errors similar to those found in the axial velocity fields of the second case (see figure 4.3). Further observations corresponding to the previous shown results are the misregistrations at  $\frac{x}{D} \approx -2$  as well as at  $|\frac{y}{D}| \approx 0.6$ , the increased noise at the CCC and the pixelated pattern of signal noise at the downstream end of the MRV measurement section.

The axial position of the transverse slice is set to  $\frac{x}{D} \approx 0.4$ . Its axial velocity field is determined on the basis of 100 samples. Although the depicted cross-section manifests the expected jet profile, the axial velocity magnitudes do not match the values indicated in (A) at the corresponding axial position. The axial peak velocity ratio based on the profile of (A) at  $\frac{x}{D} \approx 0.4$  and (B) is approx. 1.3. Thus, a significant underestimation of axial velocities within the transverse slice must be assumed. The flow void at the upper edge of the transverse slice is caused by a stationary air bubble that may negatively affect data validity. Furthermore, vague marks suffuse the transverse slice at the center region ( $-0.2 < \frac{y}{D} < 0.2$ ). These inconspicuous marks may be indicative of measurement artifacts (e.g. *ghosts*).

## 4 Results

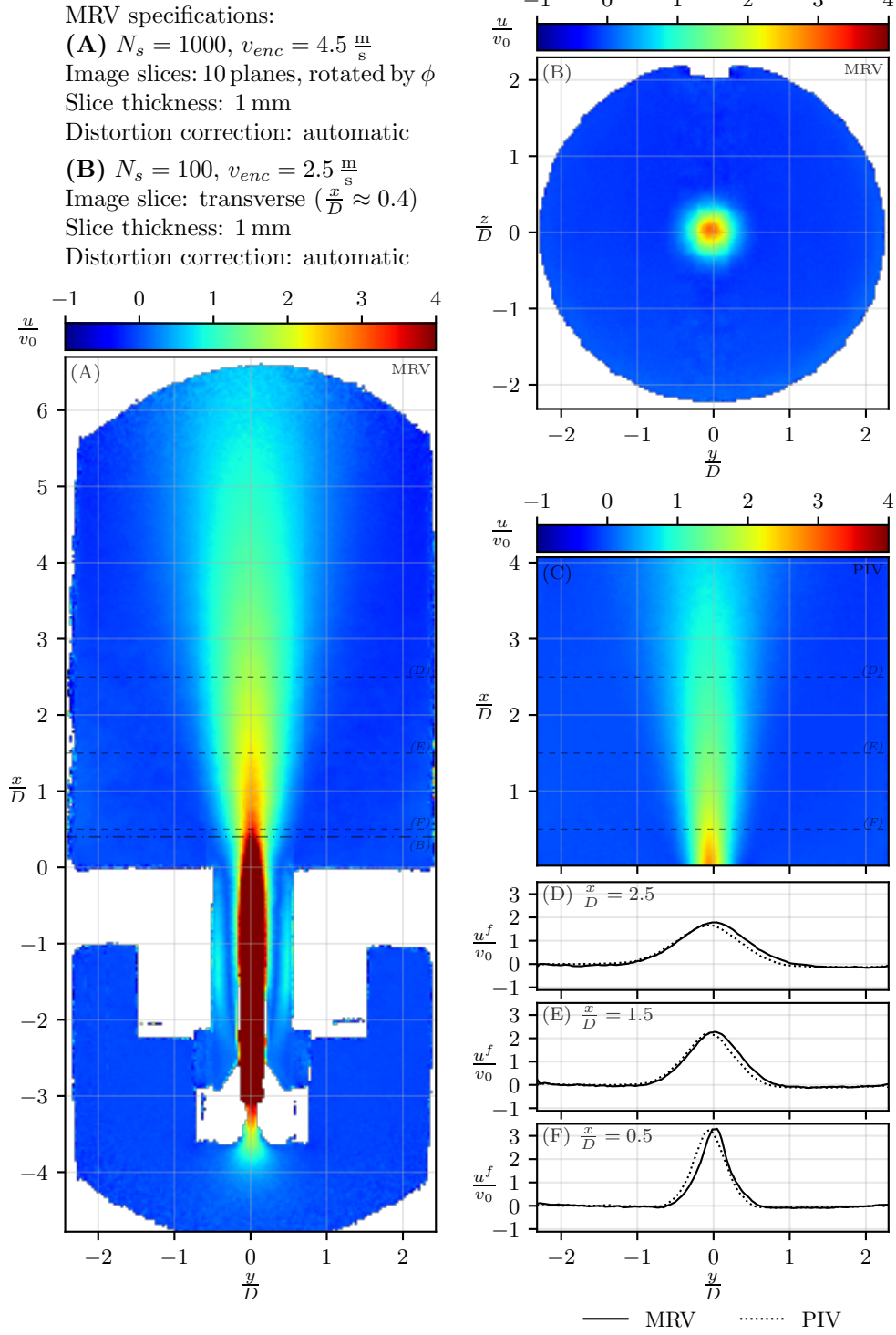


Figure 4.5: Axial velocity field comparison of the case: sole injector jet; (A) MRV, azimuthal average of 10 planes with differing angles of rotation  $\phi$  (B) MRV, transverse plane (C) PIV, coronal plane (D)-(F) MRV and PIV velocity profiles from (A) and (C) at  $\frac{x}{D} = 2.5$ ,  $\frac{x}{D} = 1.5$  and  $\frac{x}{D} = 0.5$

## 4 Results

The last case of the comparison of mean PIV and MRV velocity fields is shown in figure 4.6. Transverse velocities of the sole injector jet case are obtained from the same measurement slices as mentioned at the beginning of this section in the description of the axial velocity field acquisitions. However, acquisitions within the transverse slice are omitted. The velocity fields within the shared FOV of subplots (A) and (B) present a rather dissimilar picture close to the mixing tube's outlet. Regions of inward-facing flow at  $\frac{x}{D} \approx 0.1$  largely differ in size and shape, although an excess in velocity magnitudes is recognizable in both PIV and MRV on the right-hand side. The probably most significant difference between the transverse velocity data obtained from both measurement methods is the flow pattern at the centerline close to  $\frac{x}{D} = 0$ . MRV data depict a narrow passage, where the jet runs through the inward-facing flow coming from both sides. This passage diverges at  $\frac{x}{D} \approx 0.7$ , allowing for a delayed expansion of the central jet. In contrast, PIV data depict the onset of expansion of the central jet proximate to  $\frac{x}{D} = 0$ . Furthermore, the respective entrainment regions of PIV and MRV differ in curvature. The discrepancy between the two data sets also extends to the transverse velocity magnitudes found within the ORZ and within the branches of the entrainment regions. Still, an asymmetric pattern with an excess in velocity magnitude on the right-hand side can be observed in (A) and (B).

The extracted velocity profiles substantiate the visual impressions. At  $\frac{x}{D} = 0.5$  the profiles from PIV and MRV hardly match in the interval  $-1.5 < \frac{y}{D} < 1$ , although, however, the small magnitude of transverse velocities should be minded. At  $\frac{x}{D} = 1.5$  and  $\frac{x}{D} = 2.5$  the deviation between the profiles is rather acceptable. An exception to this may be found in (C) in the interval  $0 < \frac{y}{D} < 1$ , where MRV data reveal an area of locally increased velocities, contrasting an area of locally decreased velocities in PIV data.

Once again, the extended FOV of the MR measurement shall be reconsidered. Because of the small velocity range, noise at the CCC, and even more distinctive at the confinements of the upstream pipe, is clearly recognizable. Flow voids appear at the shear layers of the jet within the mixing tube and at the upstream area of the injector. Misregistration of flow is found at  $\frac{x}{D} \approx -2$  and  $\frac{y}{D} \approx -1.2$ . Areas of seemingly increased or decreased transverse velocity are found at the outmost corners of the MRV, e.g. at  $\frac{x}{D} \approx -4$ ,  $\frac{y}{D} \approx -2.2$  or  $\frac{x}{D} \approx 5.3$ ,  $\frac{y}{D} = 2.2$ . Within the vanes an unexpected quadrupole-like pattern occurs, which may result from the superposition of the rotated slices or indicate a measurement artifact. It is worth mentioning that, as an exception, the transverse velocity field obtained from PIV data seems to be more pixelated than the MRV field within the shared FOV.

## 4 Results

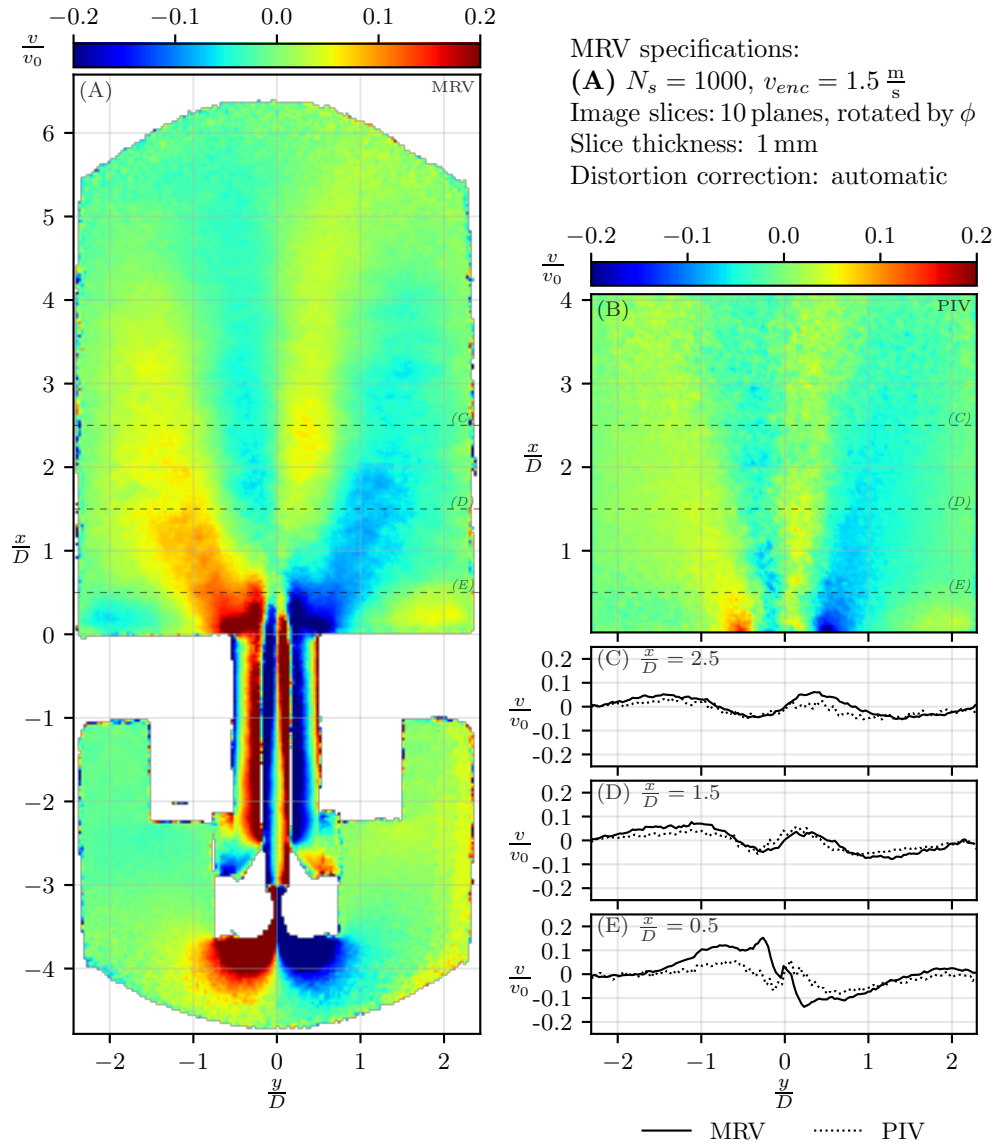


Figure 4.6: Transverse velocity field comparison of the case: sole injector jet; (A) MRV, azimuthal average of 10 planes with differing angles of rotation  $\phi$  (B) PIV, coronal plane (C)-(E) MRV and PIV velocity profiles from (A) and (B) at  $\frac{x}{D} = 2.5$ ,  $\frac{x}{D} = 1.5$  and  $\frac{x}{D} = 0.5$

## 4.4 Comparison of Through-Plane Velocities

This section covers the results of the velocity component fields perpendicular to the measurement section, i.e. the coronal slice in the given cases. Since Mono PIV is applied, which does not allow for an acquisition of the through-plane component, the comparison has to rely on the sole MRV fields. Only the first and second case are chosen for depiction because these comprise a swirling motion.

Figure 4.7 illustrates the through-plane components ( $w$ -components) of the base case and the swirling flow with injector jet in (A) and (B), respectively. The FOV are adjusted such that their axial positions coincide horizontally. However, because the measurements are performed with slightly different alignments, the subplots are shifted with respect to each other.

Since the colorbars match, the difference in color contrast indicates an increased swirl within the mixing tube for the case without injector jet. Moreover, the gap in the close proximity of the centerline appears significantly smaller as compared to the case with the injector jet. Both MR measurements show an increased through-plane velocity at the upstream section of the mixing tube. Differences in the flow pattern are identifiable downstream of the combustion chamber inlet. While in (A) the through-plane velocity branches of the emanating flow spread and gradually fade downstream of the inlet, the branches in (B) rather retain their shape and direction before reversing in a sharp bend at  $\frac{x}{D} \approx 1.1$ . Subsequently, the downstream sections of both cases depict dissimilar patterns. The case without injector jet exhibits a distinct separation along the centerline, where negative through-plane velocities—again, with an asymmetric excess—are found on the left-hand and positive through-plane velocities on the right-hand side. No such distinct separation occurs within the case with injector jet.

A few voxels at the right shear layer of both measurements ( $\frac{x}{D} \approx 0.1$ ,  $\frac{y}{D} \approx 0.5$ ) show anomalous results. As mentioned before, aliasing cannot be ruled out with certainty even though this area is particularly subjected to increased noise. Further adverse effects on the acquisitions are found in both cases: Flow voids at the vanes are more prominent in (A), especially at  $\frac{y}{D} \approx -0.5$ . The area close to the orifice of the injector, however, exhibits particular flow voids as well. Misregistrations at the interface of the swirler geometry and the blocking ring are exclusively found in (A). Note at this point that both cases differ in slice thickness (1 mm vs. 4 mm). Additionally, noise impairments are noticeable at the CCC of both cases. Whereas the misregistrations appear as more severe in (A), e.g. at  $\frac{y}{D} = -2.4$ , the FOV contour of (B) seems to be more jagged, not only at the CCC but also at the downstream end of the measurement section and at upstream confinements of the swirler geometry, e.g. at  $\frac{x}{D} \approx -3.9$ . At last, the direct comparison of the two acquisitions also illustrates the aforementioned FOV stretching of the second case caused by the manual distortion correction.

## 4 Results

MRV specifications:

*Swirling flow without injector jet*

(A)  $N_s = 1000$ ,  $v_{enc} = 2.5 \frac{m}{s}$

Image slice: coronal

Slice thickness: 1 mm

Distortion correction: automatic

*Swirling flow with injector jet*

(B)  $N_s = 1000$ ,  $v_{enc} = 2.5 \frac{m}{s}$

Image slice: coronal

Slice thickness: 4 mm

Distortion correction: manual

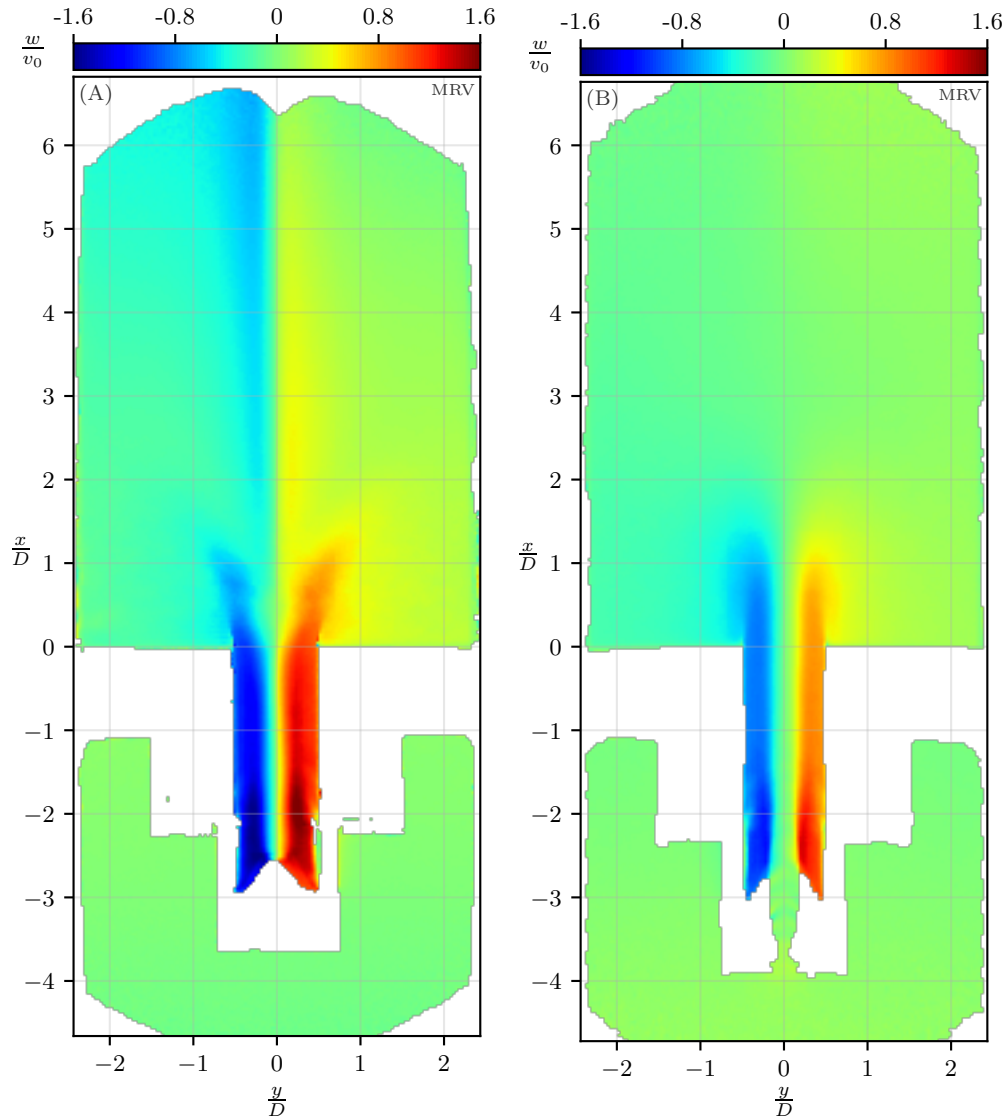


Figure 4.7: Through-plane velocity field comparison of the cases: swirling flow without and with injector jet; (A) MRV, coronal plane, without injector jet (B) MRV, coronal plane, with injector jet

## 4.5 Comparison of Modes Obtained from POD and LSA

Figure 4.8 pictures the resulting modes obtained from POD and global LSA in (A) and (B), respectively. The eigenvalue spectrum of the LSA modes is depicted in (C), where  $\omega_r$  and  $\omega_i$  denote the real and imaginary part of the coherent mode's angular frequency, respectively. The selected eigenvalue, which corresponds to the mode in (B), is marked with a red cross. Note that the real part of the eigenvalue lies well within the expected interval, i.e. between 3.7 and 4.4 (see section 3.4). Further note that the growth rate, which is expected to be (close to) zero for the case of a marginally stable mode (see section 2.8), is  $\omega_i \approx -0.6$  and thus not exactly complies with the conditions. However, the selected eigenvalue is located at a distinct position within its vicinity, indicating its particular significance. One further distinct eigenvalue of potential interest is found at  $\omega_r \approx 2.8$ . Since this value is outside the interval of the expected angular frequency, the corresponding mode is not taken into consideration.

Two remarks shall be made, before the modes are compared. Firstly, the real part of the LSA mode, which is calculated from the (temporal and azimuthal) mean MRV fields on the bisected central cross section, is mirrored at the centerline to allow for a similar representation of the two results. Secondly, recall that the first two PIV modes are combined to a complex mode and adjusted in phase angle such that the resulting modes from POD and LSA approximately match.

In principle, the results depicted in subplots (A) and (B) are in reasonable agreement, although three major differences appear. The first conspicuous discrepancy is the attenuated decay of the mode obtained from LSA, which results in a stretched extent of the mode shape beyond  $\frac{x}{D} = 2$ . Moreover, the spatial wavelengths of both modes slightly differ, which is especially recognizable in the region of  $1.3 < \frac{x}{D} < 2$ . At last, the particular contours and shapes of the individual LSA mode features differ from the corresponding counterparts given by the combined POD modes, e.g. at  $\frac{x}{D} \approx 1.2$  and  $\frac{y}{D} \approx 0.7$ .

Further remarkable findings are the faint, drop-shaped and the elongated, tooth-shaped structure depicted downstream of and in the mixing tube of subplot (B). Rather than the actual occurrence, the extent that stretches far upstream appears as an unexpected result.

On the basis of the presented results, the thesis continues with their evaluation and the discussion of applied methods. In the course of this, a particular focus is put on the limitations found and the simplifications made during this work.

## 4 Results

POD specifications:

*Swirling flow without injector jet*

**(A)**  $N_s = 5000$ ,  $N_m = 40$

Image slice: coronal

Method: snapshot POD of  $v(\mathbf{x}, t)$

Modes combined: first two

Normalization: unsigned maximum

LSA specifications:

*Swirling flow without injector jet*

**(B)**  $N_s = 2400$ ,  $v_{enc} = 2.5 \frac{m}{s}$

Image slices: 12 planes, rotated by  $\phi$

Slice thickness: 1 mm

Distortion correction: automatic

Normalization: unsigned maximum

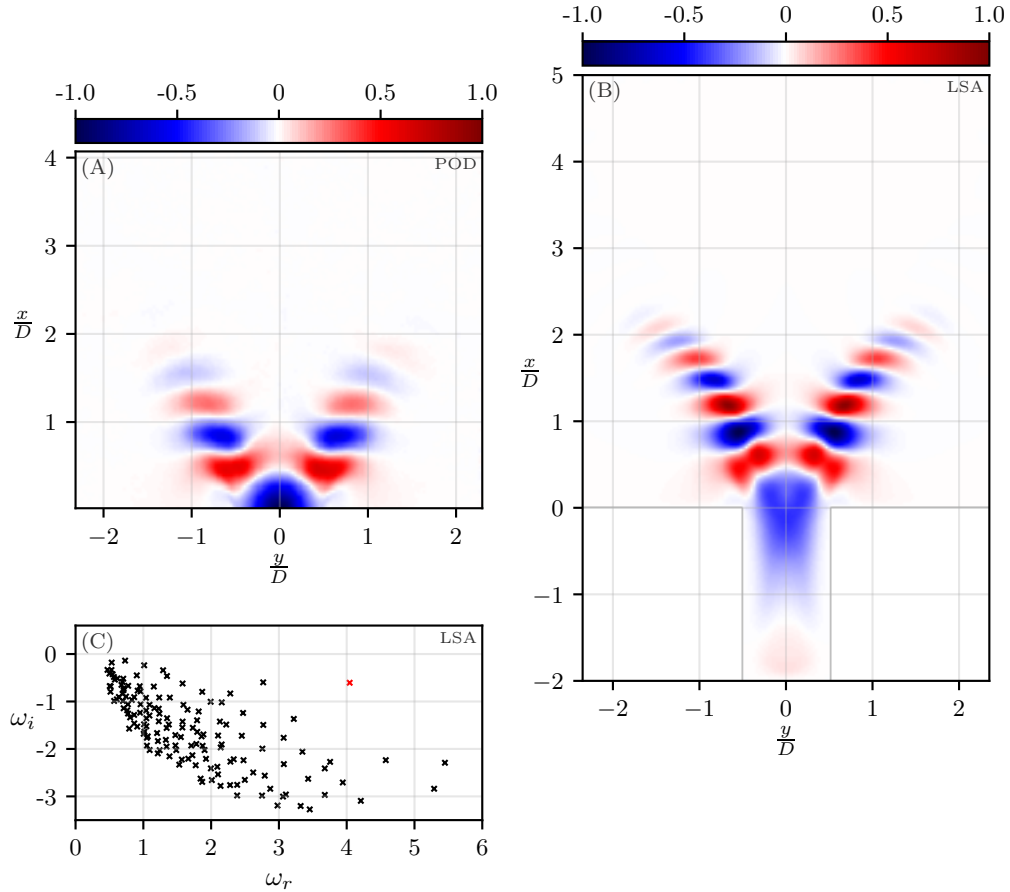


Figure 4.8: POD and LSA mode comparison of the case: swirling flow without injector jet; (A) combined first two POD modes (B) mirrored global LSA mode, obtained from the azimuthal average of 12 bisected planes with differing angles of rotation  $\phi$  (C) LSA eigenvalue spectrum, selected eigenvalue is highlighted in red

## 5 Discussion

To start with, recall that this thesis aims at the acquisition of mean velocity fields within a swirl combustor by means of PIV and MRV as well as the further processing and the comparison of the measurement results.

The application of MRV to a turbulent flow with a particular technical significance and the subsequent analysis on the basis of temporal mean fields is a novel approach for the participating institutions, i.e. the HFI and the PTB Berlin. Therefore, the task includes the design and the construction of a test rig to facilitate the experiments and to allow for an assessment of the applicability of this method. Thus, this work, and in particular this chapter, focuses on the *proof-of-concept* of the turbulent flow MRV, which is based on the temporal (and in some cases spatial) average of multiple measurement samples within the swirl combustor.

The chapter is structured as follows: At first, general remarks concerning the results given in chapter 4 are made. In the course of this, the individual cases as well as the velocity components are examined and specific findings are emphasized. Following this, measurement limitations, errors and improvement concepts are briefly evaluated. At last, future prospects and potentials of the applied methods are discussed.

### 5.1 General Evaluation of the Results

In order to assess the MRV results, PIV experiments are conducted, whose results serve as a benchmark for a comparative analysis. With respect to this benchmark it can be stated that the MRV results are, on the whole, in good agreement. The large share of specific flow characteristics found in the three different cases is recognizable in corresponding PIV and MRV fields as far as their FOV coincide. Therefore, it is reasonable to believe that mean data acquisition on the basis of multiple samples will have the potential to produce similar flow fields if measurement limitations are taken into consideration and are subsequently compensated. Further, MRV results imply that mean velocity fields of comparable quality can be obtained almost independently of the phantom geometry and the orientation of the slice. This is a convenient advantage compared with PIV experiments. However, it is important to note that the lack of velocity fields within transverse slices obtained from PIV forbids a thorough, quantitative evaluation of transverse MRV fields. The same argumentation applies to the through-plane MRV that yields reasonable results but lacks a benchmark measurement for comprehensive analysis.

Considering the specific cases of sections 4.1-4.3, four major points are of particular significance. At first, the axial velocities obtained from PIV data in the sole injector jet case exhibit a considerable discrepancy in magnitude and a recognizable discrepancy in symmetry as indicated in figure 4.5. Since PIV data can be approximately matched to

MRV data by means of simple scaling, it is justifiable to assume that the discrepancy is caused by reduced volume flow within the FOV of PIV experiments. The flow rates in all experiments are measured with sufficient accuracy. Therefore, the most reasonable explanation is that, due to the increased pressure loss at high velocities within the injector jet, gap flow occurs at the confinements of the PIV test rig. Two critical regions can be detected for these gap flows: the gaps between the fixating PMMA plates and the outer windows as well as the gaps between the downstream PMMA pipe and its PVC adapters. Since gap flows at the outer windows have to pass another gap at the downstream end of the tank, where seals and tight sockets are applied, to return to the flow outlet, it is presumed that the gap between the PMMA pipe and its adapters caused the greater part of volume flow loss. A slight imperfection in the alignment or the cylindrical geometry of the PMMA pipe could then produce an asymmetric gap flow that possibly accounts for the asymmetric shape and shift of the jet observed in PIV data. Minor gap flows may also explain some of the discrepancies found in the comparison of the transverse velocity fields of the sole injector jet. Thus, because PIV data of this case are limited in their benchmark quality, deviating MRV data within the shared FOV are hardly judgeable. At this point, it is worth mentioning that gap flows may also affect the velocity fields of the other two cases. Indications are found in figures 4.1(D) and (F) as well as 4.3(E) and (F). However, existing deviations are small as compared to the sole injector jet, which may correspond to the fact that the overall inlet area of the other cases is significantly larger. Although the REYNOLDS number of the base case is doubled as compared to the sole injector jet, the volume flow per inlet area only amounts to approximately one third of the latter case, which substantially reduces pressure loss and thereby the presumed gap flows. Furthermore, the existing small deviations in the profiles of figures 4.1 and 4.3 can also be caused by the additional measurement limitations that are discussed below. It should also be noted that the most important observations on measurement limitations do not rely on magnitude discrepancies in otherwise similar velocity profiles but rather on structural variations of flow patterns. These are found in all three cases, albeit mostly located within the extended FOV of the MRV field.

This directly leads to the second particularly important result, which can be observed within the extended FOV, i.e. in the mixing tube, and partly within the shared FOV. The unusual flow patterns that occur within the mixing tubes of the respective cases, are almost exclusively found in MRV fields of the transverse velocity component. Since these patterns extend to the shared FOV at the mixing tube's outlet and are not found in PIV fields, there is reason to believe that they are caused by measurement artifacts, which predominantly occur along the phase-encoding direction, i.e. the  $y$ -direction, if it coincides with the velocity encoding direction. It is, of course, possible that the same artifacts also occur (to a lesser extent) in the axial velocity fields but are hardly identifiable because of the increased velocity range. One indication supporting this conjecture is the presence of vague marks in the transverse slice of the third case (see figure 4.5). If these marks indicate artifacts, their occurrence may also explain the peak velocity deficit between subplots (A) and (B) detected within this case.

The third major point concerns the observation of asymmetry in the PIV fields of figures 4.1 and 4.3, which is particularly perceivable on the left-hand side in subplot (F) of both figures. On the one hand, geometrical imperfections originating from the

construction process can cause this effect as mentioned in section 4.2. On the other hand, localized deficiencies of the laser sheet illumination may contribute to the depicted asymmetry, which is also found in figure 4.6. However, the three remaining velocity fields obtained from PIV lack this feature, and neither the laser sheet before the measurements nor the outlier detection results from post-processing after the measurements reveal significant localized differences within this region. In conclusion, a negative impact due to insufficient illumination cannot be confirmed but also not excluded.

The last significant finding from sections 4.1-4.3 is the existence of an asymmetric whirl downstream of the CRZ, which only appears in the base case. This whirl presumably crosses the entire length of the combustion chamber and connects the CRZ to the outlet orifice of the combustion chamber. Since it appears not only in PIV but also in MRV mean fields, it is assumed to be stationary or to have at least a preferential orientation. Clearly, negative transverse velocities pictured in figure 4.2 indicate an asymmetry with respect to the centerline that may correspond to the asymmetric shape of the flow downstream of the mixing tube's outlet, which in turn probably results from geometrical imperfections as mentioned above. The fact that this whirl is not detectable in the other two cases leads to the conclusion that it is caused by the base case's increased swirl intensity, which results in vortex breakdown and the formation of a CRZ close to the mixing tube's outlet.

As an applicable indicator of swirl intensity, the through-plane velocity fields shown in section 4.4 depict differences in spreading and decay of the emanating branches in a comparison of the base case and the swirling flow with injector jet. In absence of PIV data, these can only be evaluated by direct comparison but, based on the reasoning on vortex breakdown induced CRZ formation, the differences in branch spreading and in the distinctness of field separation correspond to the expectations. However, the difference in slice thickness of the two data sets has to be considered. The observed differences may be less salient when the slice thickness is chosen identically.

Before discussing the results obtained from POD and GLSA, it is worth noting that the depicted flow fields of the base case are highly similar but not identical to the fields that are used as the base flow solution of the global LSA. As mentioned in section 3.4, the base flow used for LSA is obtained by averaging the bisected fields of 12 rotated slices. Because these fields are similar to the results depicted in chapter 4, their reproduction is omitted. After the averaging procedure, the transverse and through-plane velocity component can be identified as radial and tangential velocities, respectively.

Considering the POD and LSA results, it is particularly remarkable that, despite the simplified model given in equations 2.53 and 2.54 and despite the presumed measurement artifacts in the radial velocity field, the modes depicted in figure 4.8 are in reasonable agreement. One reason for this is probably the small contribution of the radial velocity discrepancy as compared to the axial (compare figure 4.1(A)) and the tangential (compare figure 4.7(A)) component, which both show plausible results. A further aspect concerning the impact of the radial velocity fields is that the streaks are predominantly found within the smaller region of the mixing tube, whereas the larger share of the combustion chamber lacks severe artifacts. Nevertheless, the unexpectedly stretched structure within the mixing tube (see figure 4.8) may be caused by these streaks if both structure and streaks actually turn out to be unphysical.

In the course of the preceding general evaluation, some measurement limitations are already mentioned. For a more specific consideration, a selection of the detected impairment contributions and potential improvement approaches shall be discussed in the following section.

## 5.2 Limitations and Improvement Approaches

To start with, the MRV limitations of lesser impact are considered. Noise at the CCC, or more generally at the boundaries of the fluid, and further misregistrations at interfaces can be detected in almost all measurements. Increasing the threshold value of the simplified filter leads to the loss of data, e.g. in highly turbulent regions, and is thus no applicable option. As it is often the case, increasing the SNR appears to be the expedient—though challenging—means. In fact, various approaches exist to increase signal magnitude. These include the use of contrast agents, higher main magnetic flux densities, an increased number of samples, larger voxel sizes and many more, although for some of these (e.g. voxel sizes) trade-offs must be considered, if the approach is viable at all.

A further option to increase SNR is to reduce the noise, for example, by reducing magnetic field inhomogeneities. Clearly, this is in a general sense an ongoing subject of research. Yet, a straightforward improvement could rely on the choice of materials of the phantom components. Because of its enhanced resistance to pressure and its convenience in the process of manufacturing, PVC elements are used for the construction of the phantom. However, this choice may negatively affect the magnetic field homogeneity close to the solid-fluid interfaces due to an elevated difference in susceptibility of water and PVC as compared to, for example, water and PMMA (see Wapler et al. [2014]). As outlined in section 2.3, susceptibility deviations lead to local magnetic field inhomogeneities by distorting the magnetic field lines, which in consequence results in measurement inaccuracies. This might be a minor influence but, considering the large volume of PVC, improvements are possible to achieve.

This approach does not resolve the problem of misregistrations at interfaces where static water remains within gaps (see for example figure 4.5(A) at  $\frac{x}{D} \approx -2.1$ ). An increased SNR and enhanced filter functions may allow for an elimination of these misregistrations. A further small, though undesirable, limitation concerns the stationary air bubbles, which may not only lead to incomplete flow data but may also have impact on the obtained flow field itself. It is assumed that stationary bubbles upstream of the swirler geometry do not affect the downstream flow structures. However, this can hardly be proven. Moreover, for the sole injector jet case small, stationary bubbles are also found within the combustion chamber. In order to account for a potential negative impact, future phantom designs can benefit from providing additional air vents at the upper side around the measurement ROI. This modification will also simplify measurement preparations.

Another measurement observation cannot be attributed to imaging artifacts with absolute certainty, but if the identified velocity differences that depend on the measurement quadrant (see for example figure 4.1(B)) are indeed caused by artifacts, these can be of compromising nature, especially in acquisitions with low velocity ranges. Due to the

complexity of the flow fields, further information and investigations are necessary to exclude the possibility of correct velocity acquisitions, for example in the corners of the coronal slices in figures 4.2 and 4.4. A potential cause of the presumed artifacts can be found in the occurrence of eddy currents, which are briefly mentioned in section 3.3.4, and of *concomitant fields*, also referred to as MAXWELL terms. Based on the assumption of small gradient fields in section 3.3.1, the concomitant fields are not discussed in this thesis. For further information, the interested reader may find a good starting point in the works of NORRIS et al. (Norris and Hutchison [1990]) and BERNSTEIN et al. (Bernstein et al. [1998]). Correction of measurement errors caused by eddy currents typically relies on estimations based on phase differences in static tissue (Schmitter and Schnell [2018]). Considering the given application where commonly no static fluid is present within the ROI, an isolated water-filled chamber integrated into the design of future phantoms can help to improve the estimation and thus the eddy current correction.

Severe impairment of the presented measurement data mainly manifests in two observations. The first relates to significant flow voids, the second to the occurrence of streak patterns within and close to the mixing tube. Flow voids are most probably caused by broad velocity distributions within a voxel. As this is an intrinsic feature of turbulent flows, the increase of spatial resolution, which would be a straightforward approach to tackle such problems, does not necessarily need to translate into improved results. Moreover, an increase of spatial resolution also necessitates an increase of the SNR basing on the improvement approaches outlined above and further advanced techniques. In order to address the problem of the streak pattern, again assuming that they are unphysical, more research is needed. A first step could include the determination of dependencies of their occurrence, e.g. the direction of phase-encoding, the slice thickness, TE, TR or further sequence design parameters. Perhaps, even altering the choice of materials yields perceivable differences due to the reduction of magnetic field inhomogeneities within the large central socket. Ruling out that the patterns are caused by discrete measurement ghosts may also become necessary. An important improvement, however, can be expected when acceleration-compensated measurement sequences are applied. Although this approach is not necessarily effective to avoid the streak pattern, it will in any case prove beneficial for the overall accuracy. Typically, acceleration-compensated measurements are subjected to prolonged acquisition times, and are therefore rarely applied in clinical use. Considering engineering purposes, prolonged acquisition times are less critical and can possibly contribute to the elimination of further unexpected measurement observations, e.g. the presumably rotationally shifted twin pattern depicted in figure 4.2(B).

Of course, more limitations may be veiled behind these mentioned above or may become more apparent in the course of future applications. For example, the vague marks and the significant underestimation of axial velocities in the sole injector jet case (see figure 4.5, (A) and (B)) indicate that further studies have to be performed for an improved comprehension of their causes.

Further studies could also benefit from an alteration of the measurement principle. Although this particular aspect cannot be considered as a limitation for the conducted experiments, a specific restriction is made by filling of  $\mathbf{k}$ -space along the Cartesian directions.

Similarly, the use of anisotropic voxels could be avoided in follow-up studies, although negative impacts on the obtained measurement results are not directly conspicuous. Retaining the high spatial resolutions in measurement slices, i.e. in the frequency- and phase-encoding direction, then requires a decreased slice thickness, which commonly results in a decreased SNR. Thus, a well-performing compromise must be aimed at. At last, a conceivable approach to improve spatial resolution and smoothness of the velocity fields would be to perform multiple acquisitions with voxel grids in image space that are slightly shifted with respect to each other and interpolate the resulting fields.

In a final section, an outlook is given to elucidate further potentials of this measurement technique and to point out exemplary objectives, provided that the described problems and limitations can be overcome.

### 5.3 Future Prospects and Potentials

The most specific and significant advantage of MRV is its ability of signal acquisition without optical access and without noteworthy flow disturbance. This is a striking argument in favor of MR acquisitions not only in clinical use but also for potential engineering purposes. Complex geometries often limit the feasibility of flow studies that require optical access such as PIV experiments. Moreover, the extents of the FOV are often reduced by geometrical restrictions and, in the case of PIV, by the fixed orientation of the laser sheet. In contrast, MRV allows for a substantially improved flexibility concerning the orientation of measurement slices. Geometrical restrictions are of secondary importance and rather influence the distribution of the fluid (e.g. by air pockets) than the actual acquisition. On the downside, one has to consider that the velocity ranges in MR acquisitions are largely limited, that MRV images do not represent proper snapshots and that regions of increased turbulence are accompanied by significant signal loss. Furthermore, since the voxel size cannot be chosen in orders considerably smaller than in this thesis, minimum experiment length scales must be considered. In consequence, maximum length scale ratios given by the measurement coils are binding for a single-acquisition experiment. As a summary of these arguments, it can be stated that the future use of MRV for engineering applications will prove particularly beneficial in three-dimensional flows with low to moderate velocities, especially when complex geometries and various measurement planes are investigated.

Future applications can also pursue and intensify the use of data- or operator-based decomposition techniques. Specifically for the use of a global stability analysis, the results depicted in figure 4.8 are promising. In order to further improve the validity of the stability modes, and perhaps the similarity to corresponding POD modes, an approach that involves a spatially dependent eddy viscosity on the basis of the RST and the mean rate-of-strain tensor would be advantageous. This approach may largely alter the local effective viscosity and thereby change the local decay of coherent structures as well as the growth rate, i.e. the imaginary part of the eigenvalue, which currently shows a significant difference to the expected value of zero. Prospectively, the determination, or even the approximate estimation, of the RST in a complex flow field can be a viable and reasonable objective, which augments the significance of MRV with respect to

engineering purposes.

A further, interesting field of application is found in the experimental conduct of a *resolvent analysis* on the basis of time-averaged MRV data. Subsequently, a worthwhile approach would rely on the reconstruction of mean and fluctuating flow states by means of a resolvent analysis, where the input data consist of a time-averaged MR flow field (e.g. within a certain measurement slice) and pointwise time-resolved velocity measurements. The feasibility of this method was shown, for example, for the case of a two-dimensional backward facing step using numerical data (Beneddine et al. [2016]) and for a cold round jet using experimental data obtained by PIV (Beneddine et al. [2017]). Furthermore, for a comprehensive explanation of a particular reconstruction methodology based on PIV experiments, data-assimilation and a resolvent analysis, the work of SYMON may be of increased interest (Symon [2018]). One concept addressing the problem of time-resolved measurements is *FOURIER velocity encoding* (FVE), which was already proposed in the early 1980s and allows for the quantification of velocity spectra (Moran [1982], see also Elkins and Alley [2007], Macgowan et al. [2005]). However, pointwise MR acquisitions, also referred to as *single-point imaging* techniques, remain an field of intensified research up to the present day (see e.g. Bruschewski et al. [2019]). Nevertheless, since pointwise time-resolved acquisitions can be achieved by different measurement techniques, a combined measurement approach would probably still facilitate an experimental reconstruction of the mean and fluctuating flow states. The reconstruction of fluctuating flow states as outlined above might eventually prove as a valuable tool not only for technical flows but also for clinical use. If the reconstruction of fluctuating flow states can be achieved on the basis of one mean flow and a few pointwise time-resolved acquisitions, an accelerated measurement alternative might be found for the in-vivo estimation of REYNOLDS stresses and the related turbulent viscous shear stresses. Of course, this prospect appears rather farsighted, but it also illustrates the potential of this method yet to be exhausted.

## 6 Conclusion

This thesis covered the experimental investigation of the turbulent flow field inside a swirl combustor by means of PIV and MRV. The focus was on the proof-of-concept of the turbulent flow MRV, while PIV experiments were used for comparison and validation. Temporal and spatial averages with comparatively high numbers of measurement samples were used for the MRV acquisitions in order to determine two-dimensional mean velocity fields and allow for a comparison with time-averaged PIV data. These measurements and their subsequent analysis were conducted for the first time at the HFI and PTB Berlin and yielded the construction and initial operation of a new test rig at the MR facilities of the PTB Berlin, which will be suitable for further studies.

Mean axial and transverse velocity fields of three cases with varying swirl intensity were obtained with both measurement techniques and showed in overall terms a good agreement. It appeared that data quality of these MR acquisitions was sufficient to facilitate the subsequent utilization in a global LSA, which yielded reasonable results as compared with POD modes obtained from PIV. However, the comparison of PIV and MRV results also showed minor and major deviations, which partially impaired the reliability and validity of some MRV and PIV acquisitions. Nevertheless, these measurement limitations did not compromise the general applicability of the method but rather indicate that further research is necessary in order to optimize the applied acquisition sequences.

# Bibliography

- R. Lorenz, J. Bock, A. J. Barker, F. von Knobelsdorff-Brenkenhoff, W. Wallis, J.G. Korvink, M.M. Bissell, J. Schulz-Menger, and M. Markl. 4D flow magnetic resonance imaging in bicuspid aortic valve disease demonstrates altered distribution of aortic blood flow helicity. *Magnetic Resonance in Medicine*, 71(4):1542–1553, 2014. doi: 10.1002/mrm.24802. URL <https://onlinelibrary.wiley.com/doi/abs/10.1002/mrm.24802>.
- U. Morbiducci, R. Ponzini, G. Rizzo, M. Cadioli, A. Esposito, F. De Cobelli, A. Del Maschio, F. Maria Montevicchi, and A. Redaelli. In Vivo Quantification of Helical Blood Flow in Human Aorta by Time-Resolved Three-Dimensional Cine Phase Contrast Magnetic Resonance Imaging. *Annals of biomedical engineering*, 37:516–31, 03 2009. doi: 10.1007/s10439-008-9609-6.
- X. Liu, Y. Fan, and X. Deng. Effect of Spiral Flow on the Transport of Oxygen in the Aorta: A Numerical Study. *Annals of biomedical engineering*, 38:917–26, 03 2010. doi: 10.1007/s10439-009-9878-8.
- P.F. Drake and E.H. Hubbard. Combustion system aerodynamics and their effect on burning of heavy fuel oil. *Journal of the Institute of Fuel*, 39(302):98–109, 1966.
- A.D. Robertson. Scaling and Modelling Criteria for Burner Design with Swirl Addition. *Journal of the Institute of Fuel*, 39(307):335–342, 1966.
- H.L. Morton. *Effect of swirl on turbulent jets in ducted streams*. PhD thesis, Massachusetts Institute of Technology, Gas Turbine Laboratory, Cambridge, USA, 12 1968. <http://hdl.handle.net/1721.1/104685>.
- J.M. Beér and N.A. Chigier. *Combustion aerodynamics*. Fuel and energy science series. Applied Science Publishers, 1972. ISBN 9780853345138. URL <https://books.google.de/books?id=eAUpAQAAMAAJ>.
- N. Syred and J.M. Beér. Combustion in swirling flows: A review. *Combustion and Flame*, 23(2):143–201, 1974. ISSN 0010-2180. doi: [https://doi.org/10.1016/0010-2180\(74\)90057-1](https://doi.org/10.1016/0010-2180(74)90057-1). URL <http://www.sciencedirect.com/science/article/pii/0010218074900571>.
- N. Syred. A review of oscillation mechanisms and the role of the precessing vortex core (PVC) in swirl combustion systems. *Progress in Energy and Combustion Science*, 32(2):93–161, 2006. ISSN 0360-1285. doi: <https://doi.org/10.1016/j.pecs.2005.10.002>. URL <http://www.sciencedirect.com/science/article/pii/S0360128505000353>.

## Bibliography

- C. Elkins and M. Alley. Magnetic resonance velocimetry: Applications of magnetic resonance imaging in the measurement of fluid motion. *Experiments in Fluids*, 43: 823–858, 12 2007. doi: 10.1007/s00348-007-0383-2.
- S. Grundmann, F. Wassermann, R. Lorenz, B. Jung, and C. Tropea. Experimental investigation of helical structures in swirling flows. *International Journal of Heat and Fluid Flow*, 37:51–63, 2012. ISSN 0142-727X. doi: <https://doi.org/10.1016/j.ijheatfluidflow.2012.05.003>. URL <http://www.sciencedirect.com/science/article/pii/S0142727X12000665>.
- F. Wassermann, D. Hecker, B. Jung, M. Markl, A. Seifert, and S. Grundmann. Phase-Locked 3D3C-MRV Measurements in a Bi-stable Fluidic Oscillator. *Experiments in Fluids*, 54, 01 2013. doi: 10.1007/s00348-013-1487-5.
- D.K. Freudenhammer. *Magnetic Resonance Velocimetry for Unsteady Flows*. PhD thesis, Technische Universität Darmstadt, 1 2017. URL <https://tuprints.ulb.tu-darmstadt.de/id/eprint/5847>.
- R.W. Brown, Y.C.N. Cheng, E.M. Haacke, M.R. Thompson, and R. Venkatesan. *Magnetic Resonance Imaging: Physical Principles and Sequence Design*. Wiley, 2014. ISBN 9780471720850. URL <https://books.google.de/books?id=Z45SAwAAQBAJ>.
- W. Pauli. Zur Quantenmechanik des magnetischen Elektrons. *Zeitschrift für Physik*, 43(9):601–623, 9 1927. ISSN 0044-3328. doi: 10.1007/BF01397326. URL <https://doi.org/10.1007/BF01397326>.
- F. Gori, S. Vicalvi, M. Santarsiero, F. Frezza, G. Schettini, S. Ambrosini, and R. Borghi. An elementary approach to spinors. *European Journal of Physics*, 18:256–262, 01 1999. doi: 10.1088/0143-0807/18/4/002.
- J.T. Bushberg and J.M. Boone. *The Essential Physics of Medical Imaging*. Wolters Kluwer Health, 2011. ISBN 9780781780575. URL <https://books.google.de/books?id=tqM8IG3f8bsC>.
- M.A. Bernstein, K.F. King, and X.J. Zhou. *Handbook of MRI Pulse Sequences*. Elsevier Science, 2004. ISBN 9780080533124. URL <https://books.google.de/books?id=d6PLHcyejEIC>.
- M.T. Vlaardingerbroek, J.A. Boer, A. Luiten, and F. Knoet. *Magnetic Resonance Imaging: Theory and Practice*. Springer Berlin Heidelberg, 2013. ISBN 9783662052525. URL <https://books.google.de/books?id=9D78CAAAQBAJ>.
- S. Currie, N. Hoggard, I.J. Craven, M. Hadjivassiliou, and I.D. Wilkinson. Understanding MRI: basic MR physics for physicians. *Postgraduate Medical Journal*, 89(1050): 209–223, 2013. ISSN 0032-5473. doi: 10.1136/postgradmedj-2012-131342. URL <https://pmj.bmj.com/content/89/1050/209>.
- F. Bloch. Nuclear Induction. *Phys. Rev.*, 70:460–474, Oct 1946. doi: 10.1103/PhysRev.70.460. URL <https://link.aps.org/doi/10.1103/PhysRev.70.460>.

## Bibliography

- E. Fukushima and S.B.W. Roeder. *Experimental pulse NMR: A nuts and bolts approach*. Westview Press, 1981. doi: 10.1201/9780429493867.
- D. Drikakis and W. Rider. *High-Resolution Methods for Incompressible and Low-Speed Flows*. Computational Fluid and Solid Mechanics. Springer Berlin Heidelberg, 2006. ISBN 9783540264545. URL <https://books.google.de/books?id=1FVhPGEwJasC>.
- R.W. Fox, A.T. McDonald, and P.J. Pritchard. *Introduction to fluid mechanics*. Wiley international edition. Wiley, 2004. ISBN 9780471202318. URL <https://books.google.de/books?id=wroeAQAATAAJ>.
- R.L. Panton. *Incompressible Flow*. Wiley, 2013. ISBN 9781118013434. URL <https://books.google.de/books?id=fRv16MKgUp4C>.
- J. Piquet. *Turbulent Flows: Models and Physics*. Springer Berlin Heidelberg, 2013. ISBN 9783662035597. URL <https://books.google.de/books?id=6oPnCAAAQBAJ>.
- C. Meneveau and P. Sagaut. *Large Eddy Simulation for Incompressible Flows: An Introduction*. Scientific Computation. Springer Berlin Heidelberg, 2006. ISBN 9783540264033. URL <https://books.google.de/books?id=SH90vyraATOC>.
- H. Haraldsson, S. Kefayati, S. Ahn, P. Dyverfeldt, J. Lantz, M. Karlsson, G. Laub, T. Ebbers, and D. Saloner. Assessment of Reynolds stress components and turbulent pressure loss using 4D flow MRI with extended motion encoding. *Magnetic Resonance in Medicine*, 79(4):1962–1971, 2018. doi: 10.1002/mrm.26853. URL <https://online.library.wiley.com/doi/abs/10.1002/mrm.26853>.
- J.-H. Yen, S.-F. Chen, M.-K. Chern, and P.-C. Lu. The effect of turbulent viscous shear stress on red blood cell hemolysis. *Journal of Artificial Organs*, 17(2):178–185, Jun 2014. ISSN 1619-0904. doi: 10.1007/s10047-014-0755-3. URL <https://doi.org/10.1007/s10047-014-0755-3>.
- H. Ha, J. Lantz, H. Haraldsson, B. Casas, M. Ziegler, M. Karlsson, D. Saloner, P. Dyverfeldt, and T. Ebbers. Assessment of turbulent viscous stress using ICOSA 4D Flow MRI for prediction of hemodynamic blood damage. *Scientific Reports*, 6:39773, 12 2016. doi: 10.1038/srep39773.
- A.K.M.F. Hussain and W.C. Reynolds. The mechanics of an organized wave in turbulent shear flow. *Journal of Fluid Mechanics*, 41(2):241–258, 1970. doi: 10.1017/S0022112070000605.
- W.C. Reynolds and A.K.M.F. Hussain. The mechanics of an organized wave in turbulent shear flow. Part 3. Theoretical models and comparisons with experiments. *Journal of Fluid Mechanics*, 54(2):263–288, 1972. doi: 10.1017/S0022112072000679.
- G. Berkooz, P. Holmes, and J.L. Lumley. The Proper Orthogonal Decomposition in the Analysis of Turbulent Flows. *Annual Review of Fluid Mechanics*, 25(1):539–575, 1993. doi: 10.1146/annurev.fl.25.010193.002543. URL <https://doi.org/10.1146/annurev.fl.25.010193.002543>.

## Bibliography

- P. Holmes, J.L. Lumley, G. Berkooz, and C.W. Rowley. *Turbulence, Coherent Structures, Dynamical Systems and Symmetry*. Cambridge Monographs on Mechanics. Cambridge University Press, 2012. ISBN 9781107008250. URL <https://books.google.de/books?id=x93aZaFz5p4C>.
- C. Tropea, A.L. Yarin, and J.F. Foss. *Springer Handbook of Experimental Fluid Mechanics*. Springer Handbook of Experimental Fluid Mechanics. Springer, 2007. ISBN 9783540251415. URL <https://books.google.de/books?id=y0xDUAdQA1kC>.
- K. Taira, S.L. Brunton, S.T. M. Dawson, C.W. Rowley, T. Colonius, B.J. McKeon, O.T. Schmidt, S. Gordeyev, V. Theofilis, and L.S. Ukeiley. Modal Analysis of Fluid Flows: An Overview. *AIAA Journal*, 55(12):4013–4041, 2017. doi: 10.2514/1.J056060. URL <https://doi.org/10.2514/1.J056060>.
- L. Sirovich. Turbulence and the dynamics of coherent structures. I. Coherent structures. *Quarterly of Applied Mathematics*, 45:561–571, 10 1987. doi: 10.1090/qam/910462.
- K. Oberleithner. *On Turbulent Swirling Jets: Vortex Breakdown, Coherent Structures, and their Control*. PhD thesis, TU Berlin, 2012.
- O. Frederich and D. Luchtenburg. Modal Analysis of Complex Turbulent Flow. *7th International Symposium on Turbulence and Shear Flow Phenomena, Ottawa, Canada*, 7 2011.
- V. Theofilis. Global Linear Instability. *Annual Review of Fluid Mechanics*, 43(1): 319–352, 2011. doi: 10.1146/annurev-fluid-122109-160705. URL <https://doi.org/10.1146/annurev-fluid-122109-160705>.
- J.S. Müller, F. Lückoff, and K. Oberleithner. Guiding actuator designs for active flow control of the precessing vortex core by adjoint linear stability analysis. *Journal of Engineering for Gas Turbines and Power*, 141(4):41028, 2019.
- T.L. Kaiser, T. Poinso, and K. Oberleithner. Stability and sensitivity analysis of hydrodynamic instabilities in industrial swirled injection systems. *Journal of Engineering for Gas Turbines and Power*, 140(5):051506/1–10, 2018. doi: 10.1115/1.4038283. URL <https://hal.archives-ouvertes.fr/hal-01755243>.
- B.R. Noack, M. Morzynski, and G. Tadmor. *Reduced-Order Modelling for Flow Control*. CISM International Centre for Mechanical Sciences. Springer Vienna, 2011. ISBN 9783709107584. URL <https://books.google.de/books?id=NqTmEIjKeDIC>.
- D. Barkley. Linear analysis of the cylinder wake mean flow. *Europhysics Letters*, 75: 750–756, 09 2006. doi: 10.1209/epl/i2006-10168-7.
- T.G. Reichel. *Flashback Prevention in Lean-Premixed Hydrogen Combustion*. PhD thesis, TU Berlin, 2017.
- M. Raffel, C.E. Willert, Steven Wereley, and J. Kompenhans. *Particle Image Velocimetry: A Practical Guide*. Experimental Fluid Mechanics. Springer Berlin Heidelberg, 2007. ISBN 9783540723073. URL <https://books.google.de/books?id=WH5w2TvK2bQC>.

## Bibliography

- R. Schlüßler. *Optisches Geschwindigkeitsmesssystem zur vektoriellen Erfassung instationärer Strömungsprozesse*. PhD thesis, TU Dresden, 3 2017. URL <https://nbn-resolving.org/urn:nbn:de:bsz:14-qucosa-221375>.
- J.A. Fessler. Model-Based Image Reconstruction for MRI. *IEEE Signal Processing Magazine*, 27(4):81–89, July 2010. ISSN 1053-5888. doi: 10.1109/MSP.2010.936726.
- Siemens Healthcare GmbH. *Magnets, Spins, and Resonances: An introduction to the basics of Magnetic Resonance*. Siemens in-house publishing, 2015. URL <https://www.siemens-healthineers.com/de/magnetic-resonance-imaging/magnetom-world/publications/mr-basics>.
- M. Kouwenhoven, M.B. Hofman, and M. Sprenger. Motion Induced Phase Shifts in MR: Acceleration Effects in Quantitative Flow Measurements-A Reconsideration. *Magnetic Resonance in Medicine*, 33(6):766–777, 1995. doi: 10.1002/mrm.1910330605. URL <https://onlinelibrary.wiley.com/doi/abs/10.1002/mrm.1910330605>.
- S. Schmitter and S. Schnell. 4D Flow MRI. In I. Sack and T. Schaeffter, editors, *Quantification of Biophysical Parameters in Medical Imaging*, pages 187–212. Springer International Publishing, 2018. doi: 10.1007/978-3-319-65924-4\_9. URL [https://doi.org/10.1007/978-3-319-65924-4\\_9](https://doi.org/10.1007/978-3-319-65924-4_9).
- N.J. Pelc, R.J. Herfkens, A. Shimakawa, and D.R. Enzmann. Phase Contrast Cine Magnetic Resonance Imaging. *Magnetic resonance quarterly*, 7:229–54, 11 1991a.
- M. Markl, A. Frydrychowicz, S. Kozerke, M. Hope, and O. Wieben. 4D flow MRI. *Journal of Magnetic Resonance Imaging*, 36(5):1015–1036, 2012. doi: 10.1002/jmri.23632. URL <https://onlinelibrary.wiley.com/doi/abs/10.1002/jmri.23632>.
- N.J. Pelc, M.A. Bernstein, A. Shimakawa, and G.H. Glover. Encoding strategies for three-direction phase-contrast MR imaging of flow. *Journal of Magnetic Resonance Imaging*, 1(4):405–413, 7 1991b. doi: 10.1002/jmri.1880010404. URL <https://doi.org/10.1002/jmri.1880010404>.
- A. Walker, G. Liney, P. Metcalfe, and L. Holloway. MRI distortion: considerations for MRI based radiotherapy treatment planning. *Australasian Physical & Engineering Sciences in Medicine*, 37(1):103–113, Mar 2014. ISSN 1879-5447. doi: 10.1007/s13246-014-0252-2. URL <https://doi.org/10.1007/s13246-014-0252-2>.
- C. Geuzaine and J.-F. Remacle. Gmsh: A 3-D finite element mesh generator with built-in pre- and post-processing facilities. *International Journal for Numerical Methods in Engineering*, 79(11):1309–1331, 2009. doi: 10.1002/nme.2579. URL <https://onlinelibrary.wiley.com/doi/abs/10.1002/nme.2579>.
- M.C. Wapler, J. Leupold, I. Dragonu, D. von Elverfeld, M. Zaitsev, and U. Wallrabe. Magnetic properties of materials for MR engineering, micro-MR and beyond. *Journal of Magnetic Resonance*, 242:233–242, 2014. ISSN 1090-7807. doi: <https://doi.org/10.1016/j.jmr.2014.02.005>. URL <http://www.sciencedirect.com/science/article/pii/S1090780714000433>.

## Bibliography

- D.G. Norris and J.M.S. Hutchison. Concomitant magnetic field gradients and their effects on imaging at low magnetic field strengths. *Magnetic Resonance Imaging*, 8(1): 33–37, 1990. ISSN 0730-725X. doi: [https://doi.org/10.1016/0730-725X\(90\)90209-K](https://doi.org/10.1016/0730-725X(90)90209-K). URL <http://www.sciencedirect.com/science/article/pii/0730725X9090209K>.
- M.A. Bernstein, X.J. Zhou, J.A. Polzin, K.F. King, A. Ganin, N.J. Pelc, and G.H. Glover. Concomitant gradient terms in phase contrast MR: Analysis and correction. *Magnetic Resonance in Medicine*, 39(2):300–308, 1998. doi: 10.1002/mrm.1910390218. URL <https://onlinelibrary.wiley.com/doi/abs/10.1002/mrm.1910390218>.
- S. Beneddine, D. Sipp, A. Arnault, J. Dandois, and L. Lesshafft. Conditions for validity of mean flow stability analysis. *Journal of Fluid Mechanics*, 798:485–504, 07 2016. doi: 10.1017/jfm.2016.331.
- S. Beneddine, R. Yegavian, D. Sipp, and B. Leclaire. Unsteady flow dynamics reconstruction from mean flow and point sensors: An experimental study. *Journal of Fluid Mechanics*, 824:174–201, 08 2017. doi: 10.1017/jfm.2017.333.
- S.P. Symon. *Reconstruction and Estimation of Flows Using Resolvent Analysis and Data-Assimilation*. PhD thesis, California Institute of Technology, 2018. URL <http://resolver.caltech.edu/CaltechTHESIS:05302018-181049042>.
- P.R. Moran. A flow velocity zeugmatographic interlace for NMR imaging in humans. *Magnetic Resonance Imaging*, 1(4):197–203, 1982. ISSN 0730-725X. doi: [https://doi.org/10.1016/0730-725X\(82\)90170-9](https://doi.org/10.1016/0730-725X(82)90170-9). URL <http://www.sciencedirect.com/science/article/pii/0730725X82901709>.
- C.K. Macgowan, C.J. Kellenberger, J.S. Detsky, K. Roman, and S.-J. Yoo. Real-time Fourier velocity encoding: An in vivo evaluation. *Journal of Magnetic Resonance Imaging*, 21(3):297–304, 2005. doi: 10.1002/jmri.20266. URL <https://onlinelibrary.wiley.com/doi/abs/10.1002/jmri.20266>.
- M. Bruschewski, H. Kolkmann, K. John, and S. Grundmann. Phase-contrast single-point imaging with synchronized encoding: a more reliable technique for in vitro flow quantification. *Magnetic Resonance in Medicine*, 81(5):2937–2946, 2019. doi: 10.1002/mrm.27604. URL <https://onlinelibrary.wiley.com/doi/abs/10.1002/mrm.27604>.

# Appendices

# **Appendix A**

## **Technical Drawings**

Appendix A Technical Drawings

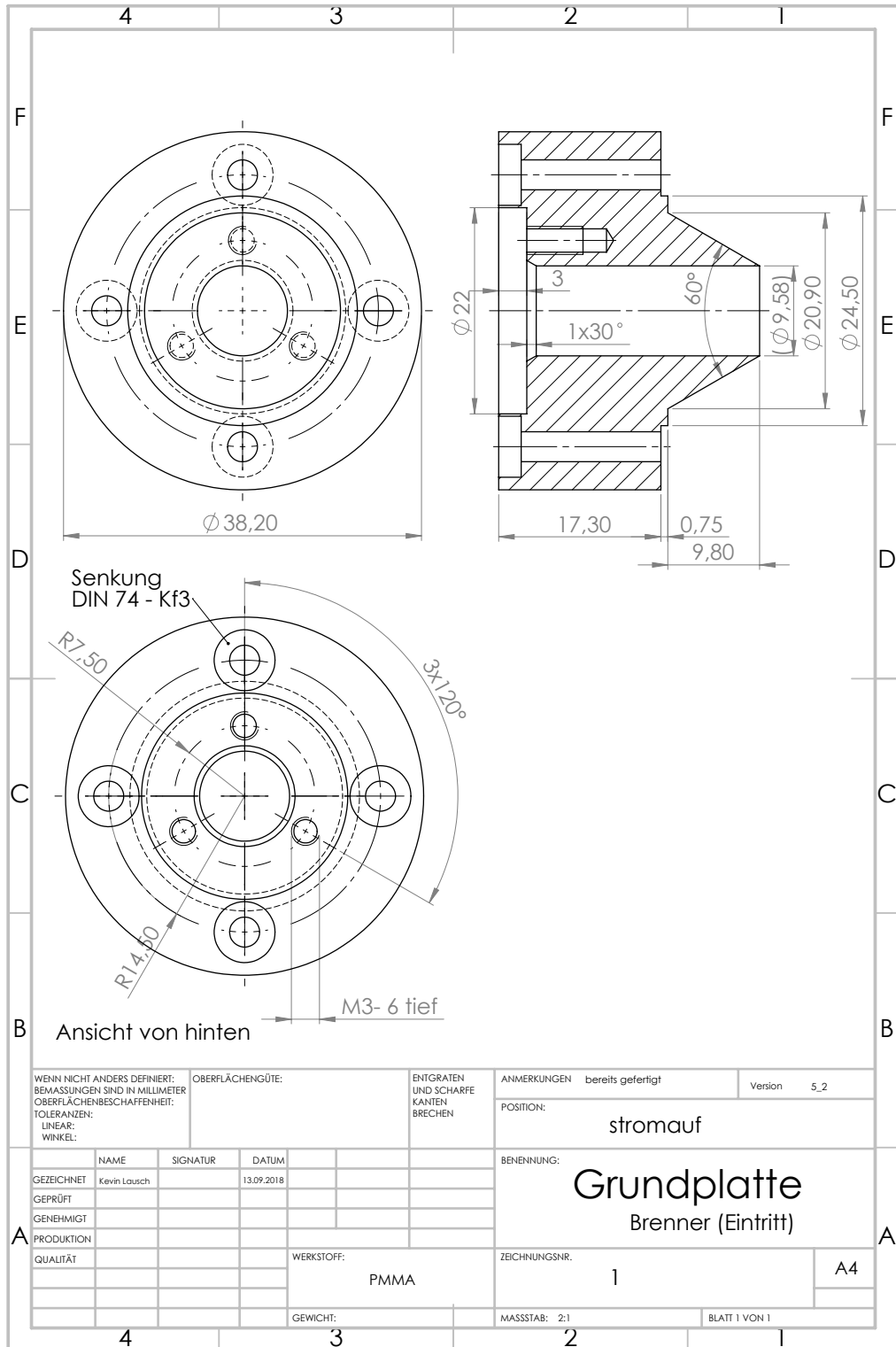


Figure A.1: Technical drawing of the upstream swirler component, including the frustum of a cone and the axial orifice

Appendix A Technical Drawings

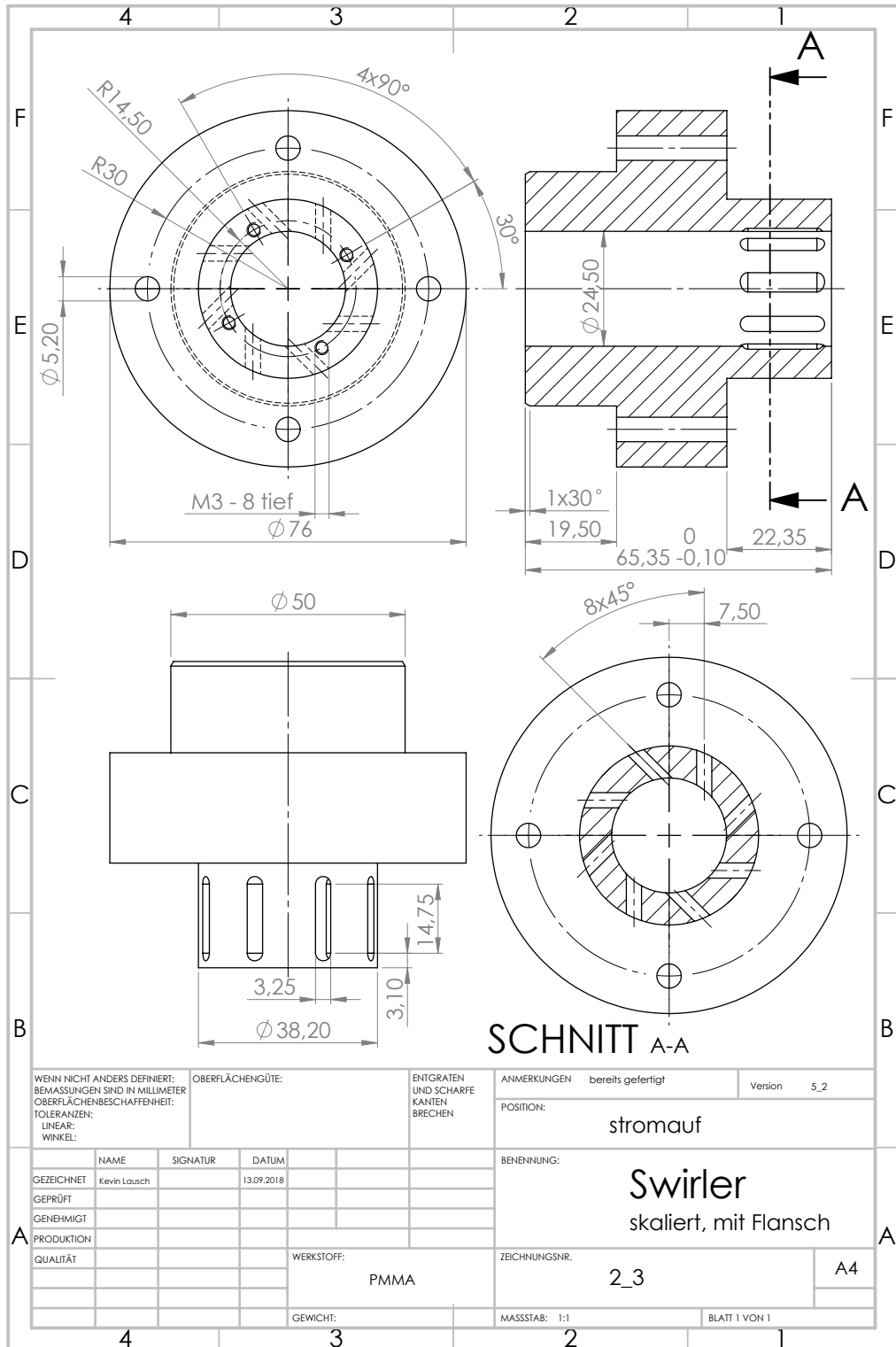


Figure A.2: Technical drawing of the downstream swirler component, including the eccentric vanes and the mixing tube

Appendix A Technical Drawings

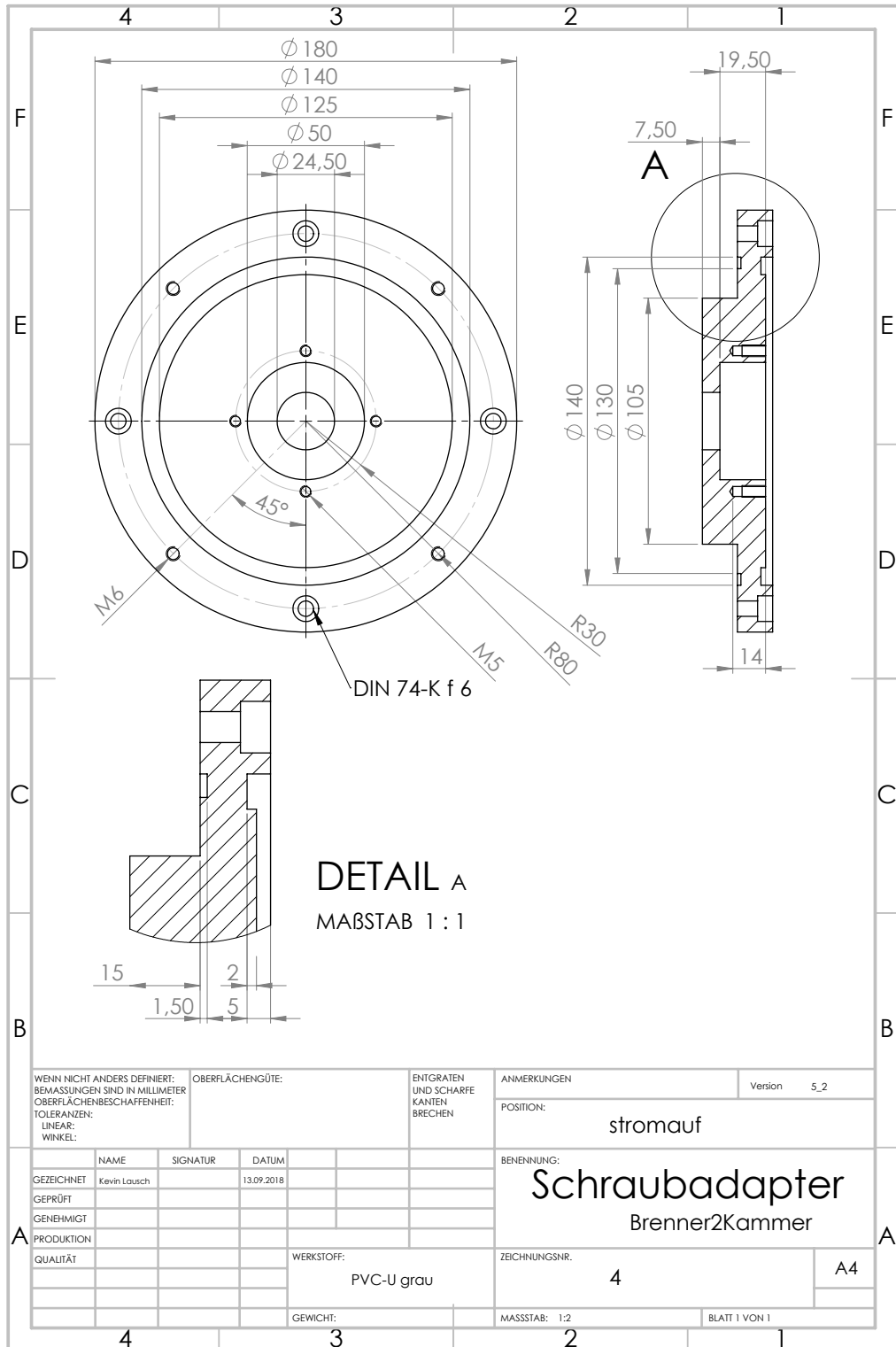


Figure A.3: Technical drawing of the removable, central swirler adapter for the test rig at the HFI water laboratory

Appendix A Technical Drawings

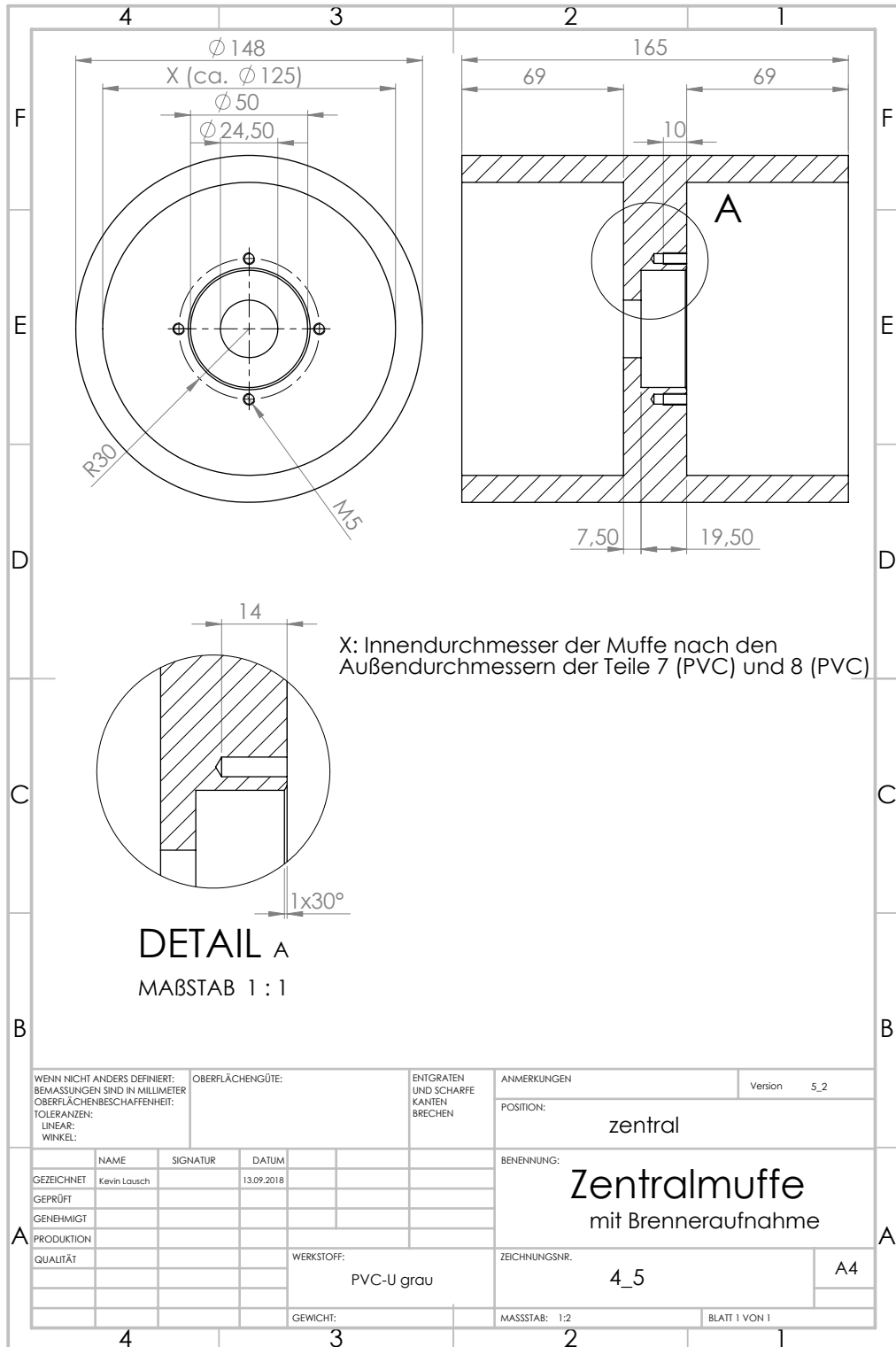


Figure A.4: Technical drawing of the central socket, used for the phantom at the facilities of the PTB

Appendix A Technical Drawings

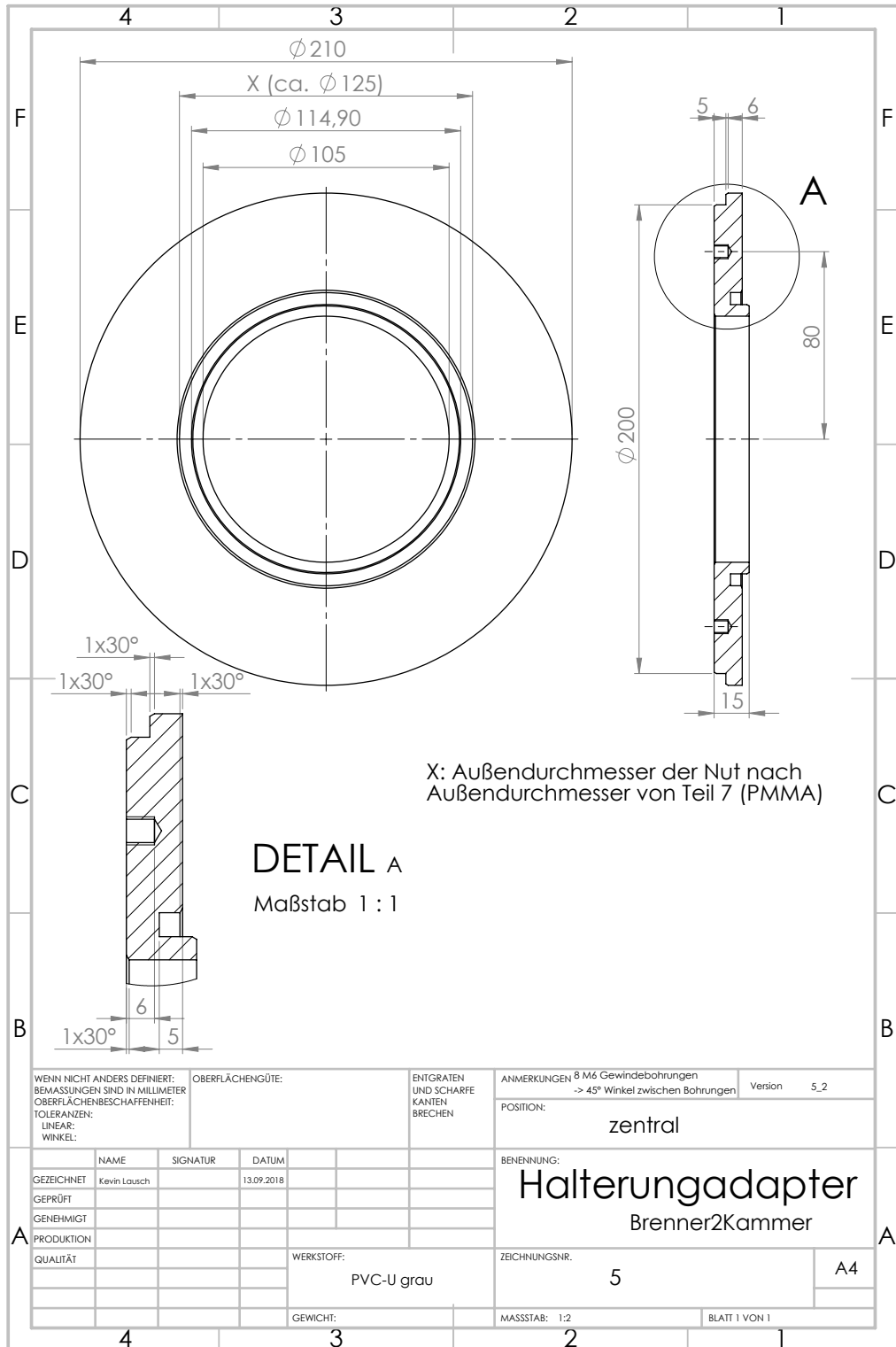


Figure A.5: Technical drawing of the central mounting adapter for the test rig at the HFI water laboratory

Appendix A Technical Drawings

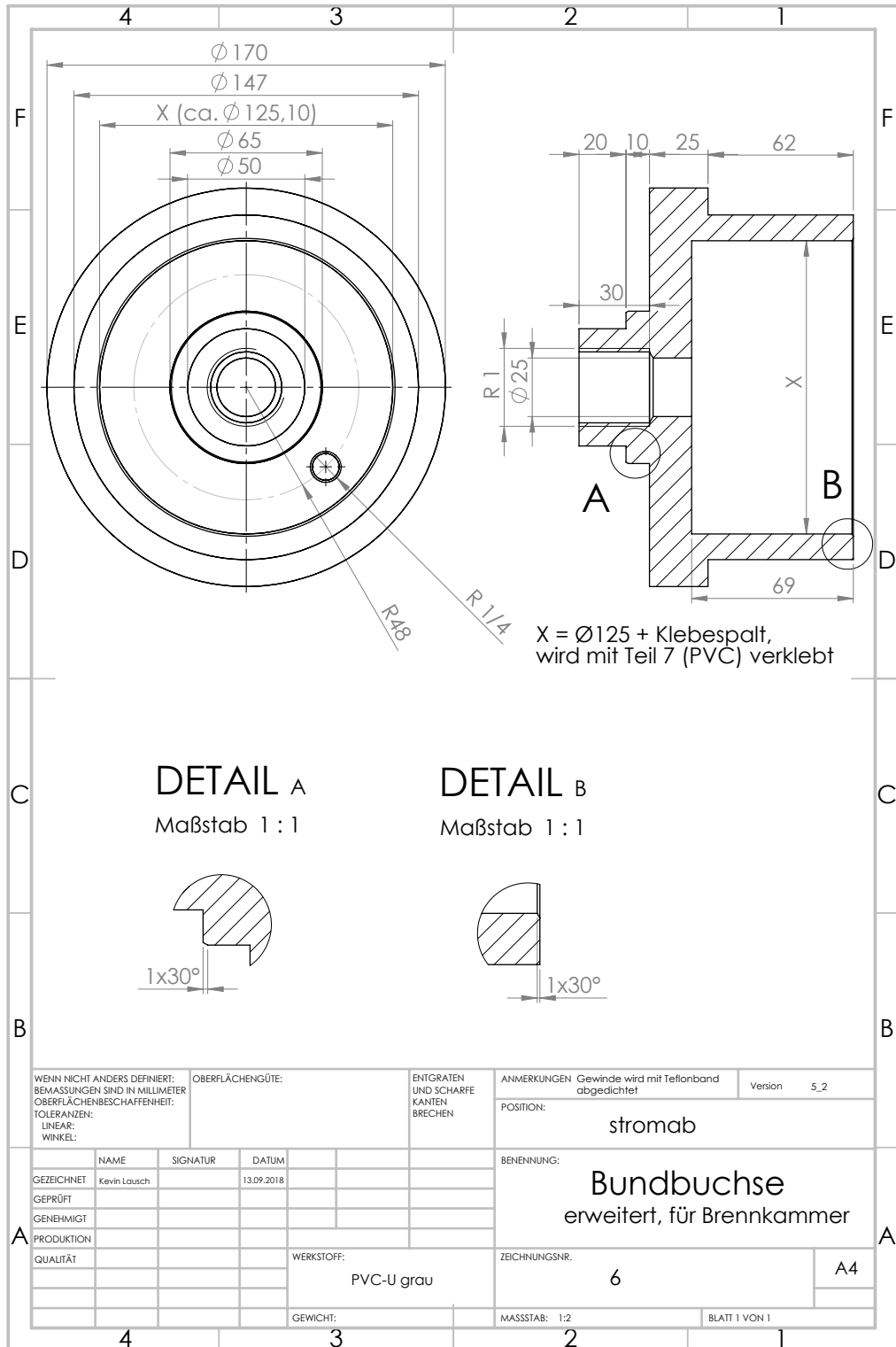


Figure A.6: Technical drawing of the downstream pipe adapter, used for both test rigs

Appendix A Technical Drawings

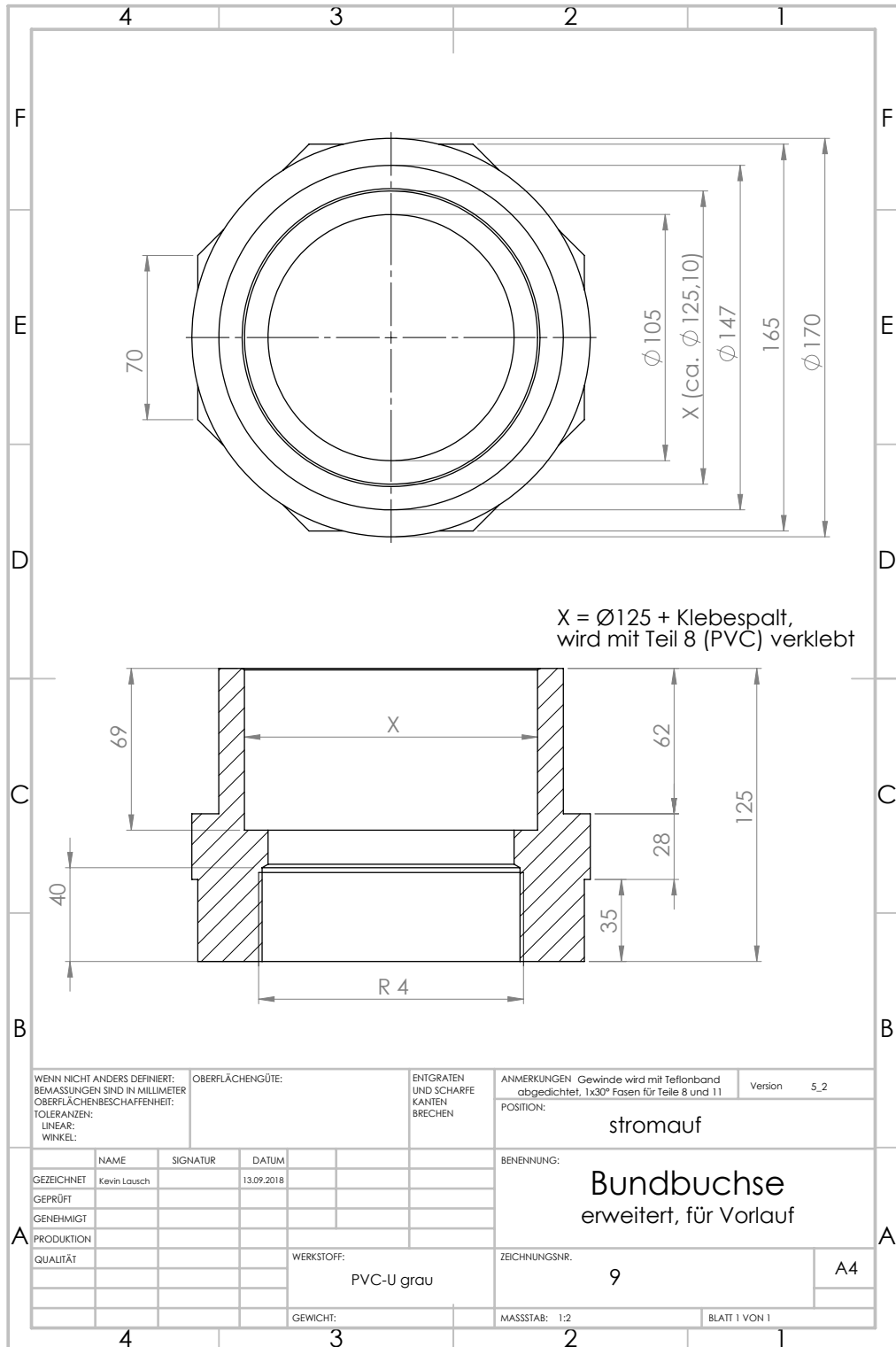


Figure A.7: Technical drawing of the upstream pipe adapter, used for both test rigs

Appendix A Technical Drawings

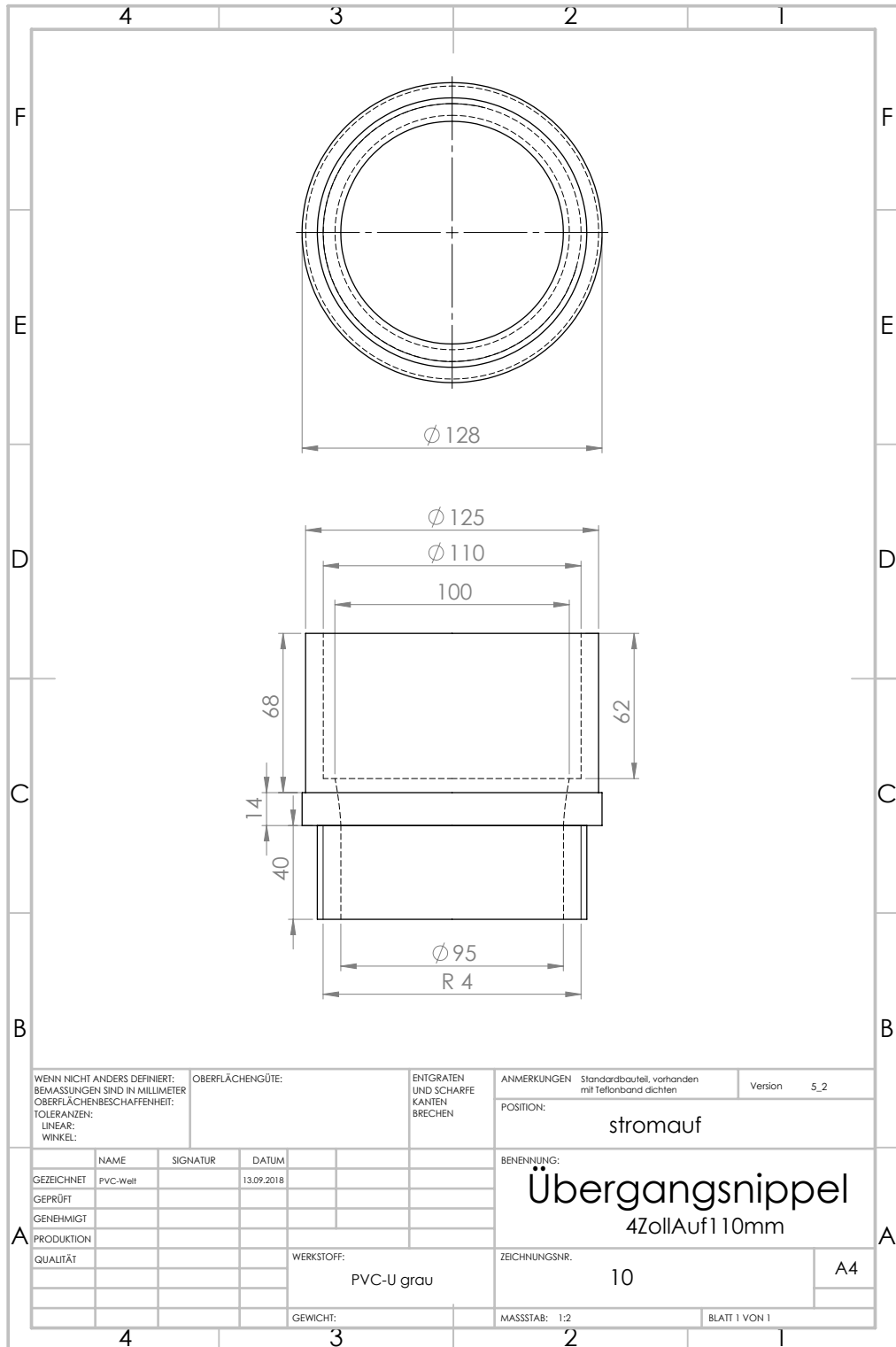


Figure A.8: Technical drawing of the upstream transition nipple, used for both test rigs

Appendix A Technical Drawings

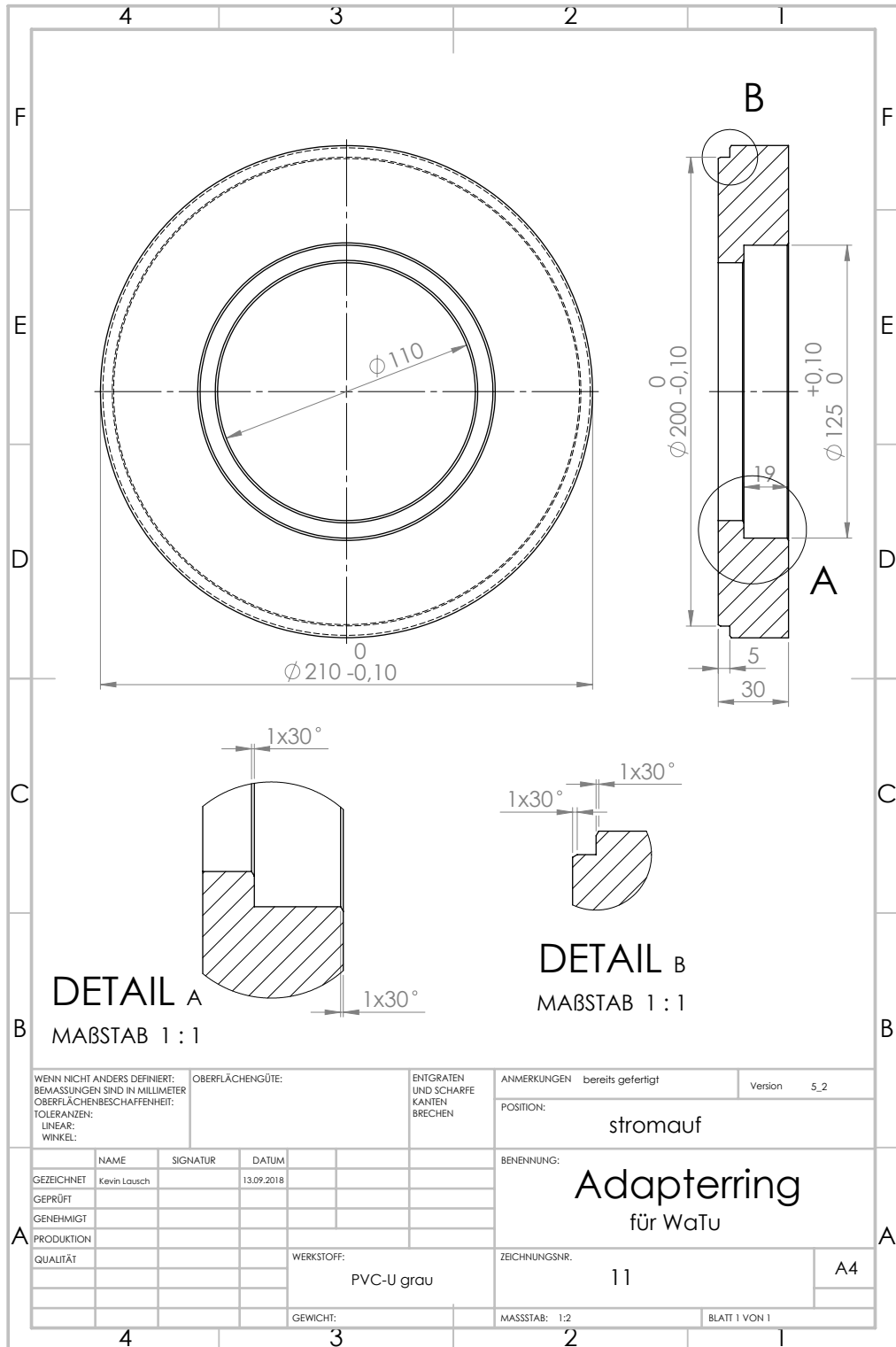


Figure A.9: Technical drawing of the upstream mounting adapter for the test rig at the HFI water laboratory

Appendix A Technical Drawings

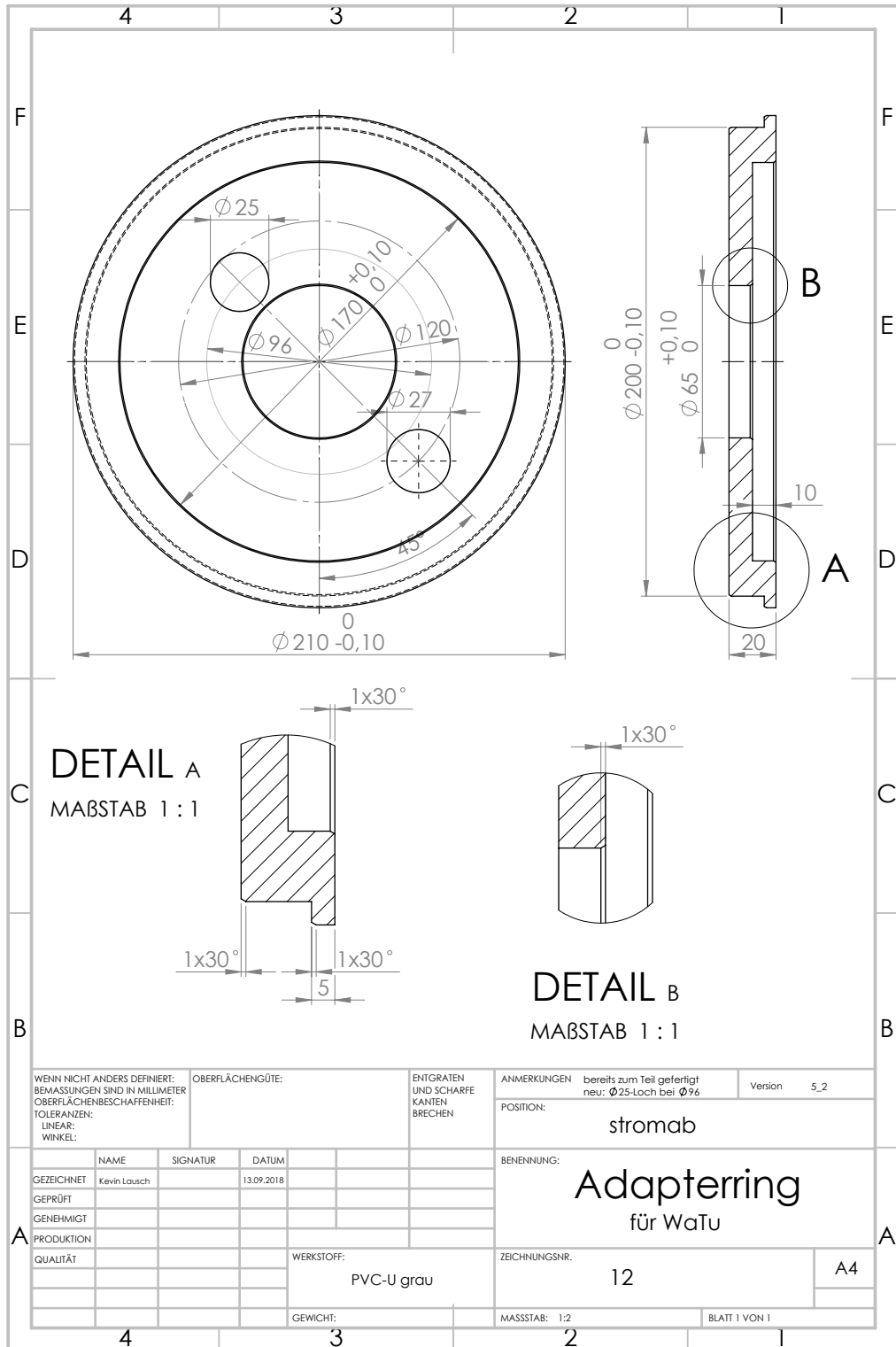


Figure A.10: Technical drawing of the downstream mounting adapter for the test rig at the HFI water laboratory

Appendix A Technical Drawings

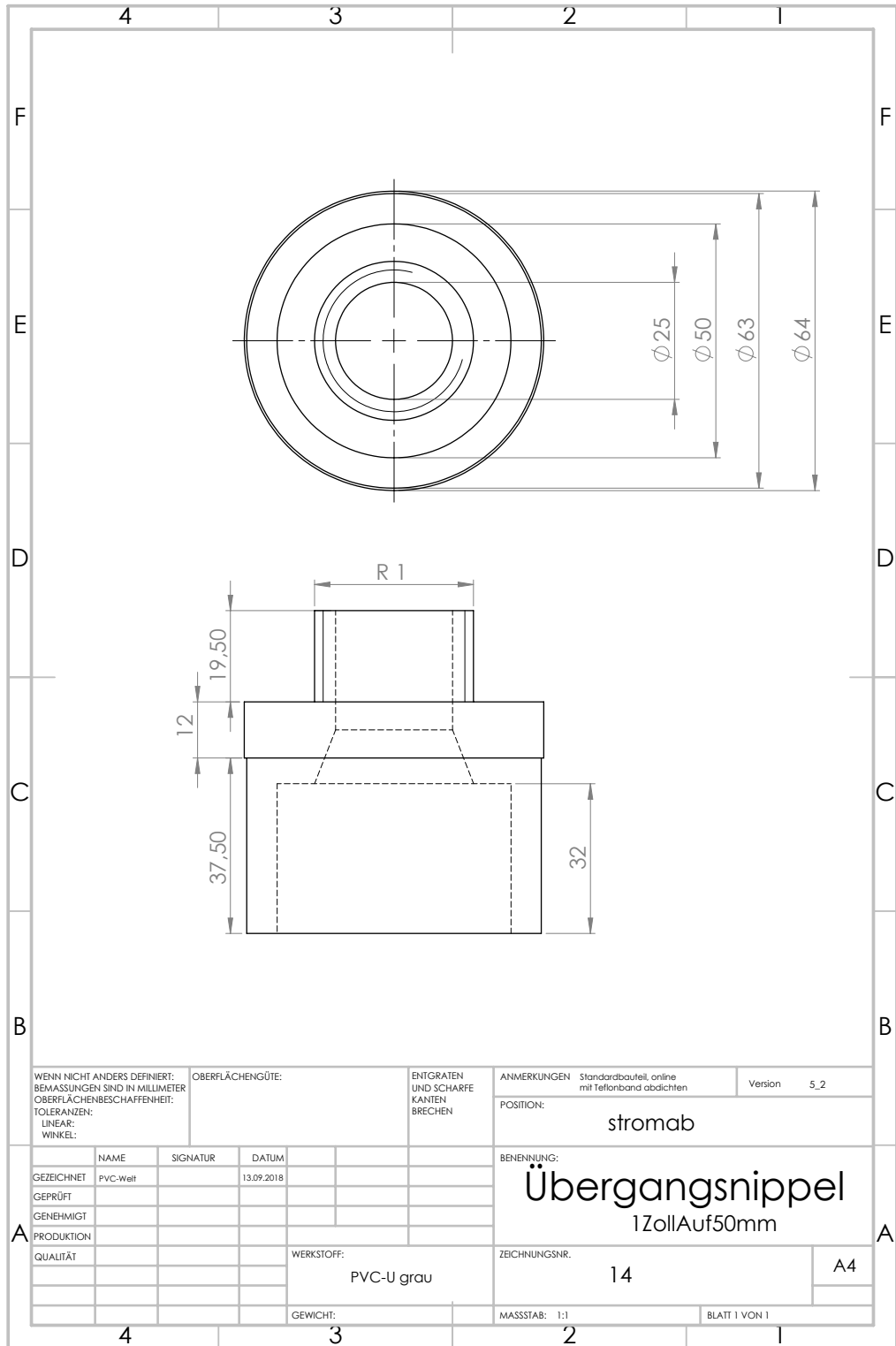


Figure A.11: Technical drawing of the downstream transition nipple, used for both test rigs

Appendix A Technical Drawings

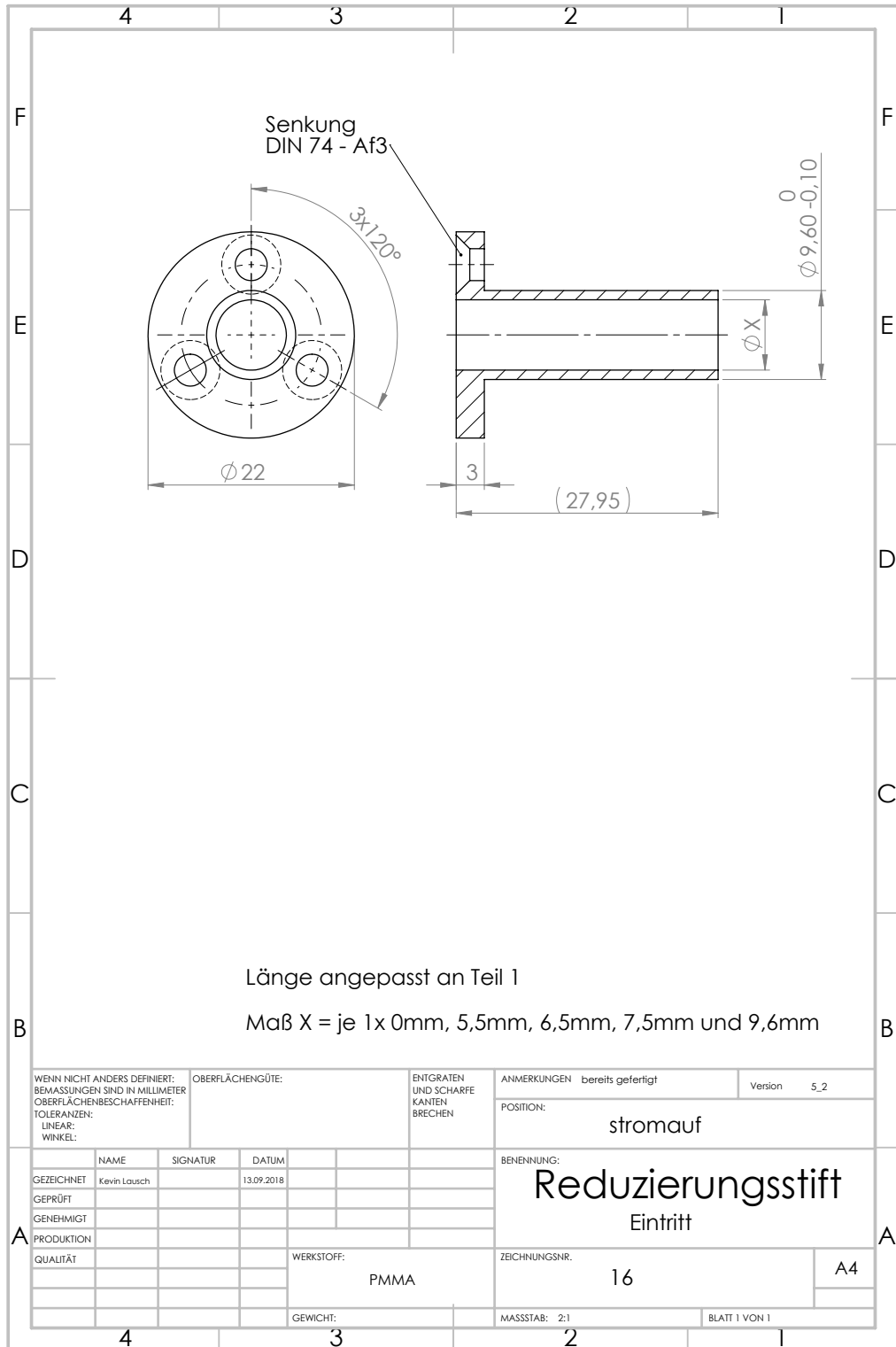


Figure A.12: Technical drawing of an exemplary axial orifice inset

Appendix A Technical Drawings

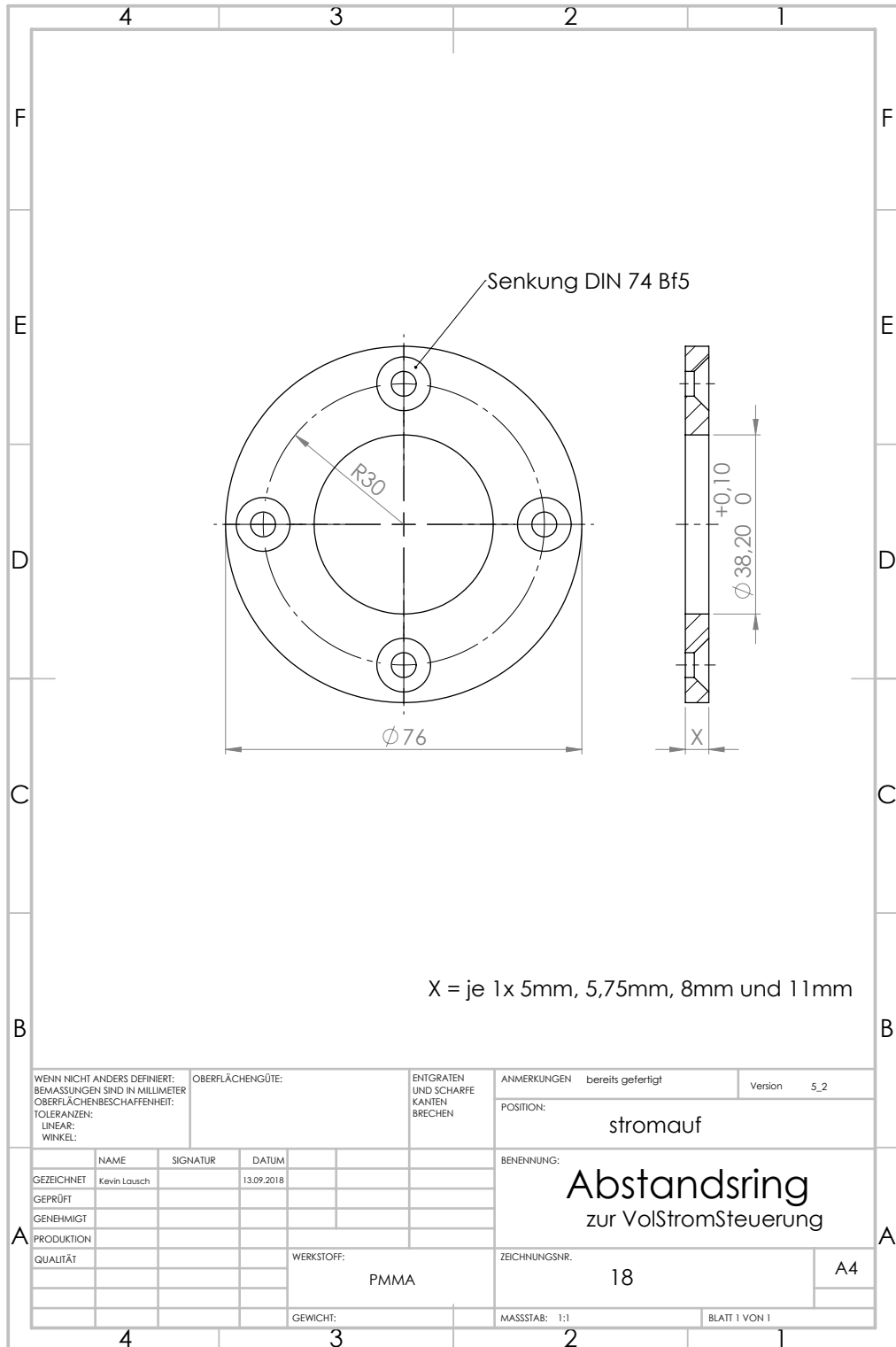


Figure A.13: Technical drawing of an exemplary blocking ring

Appendix A Technical Drawings

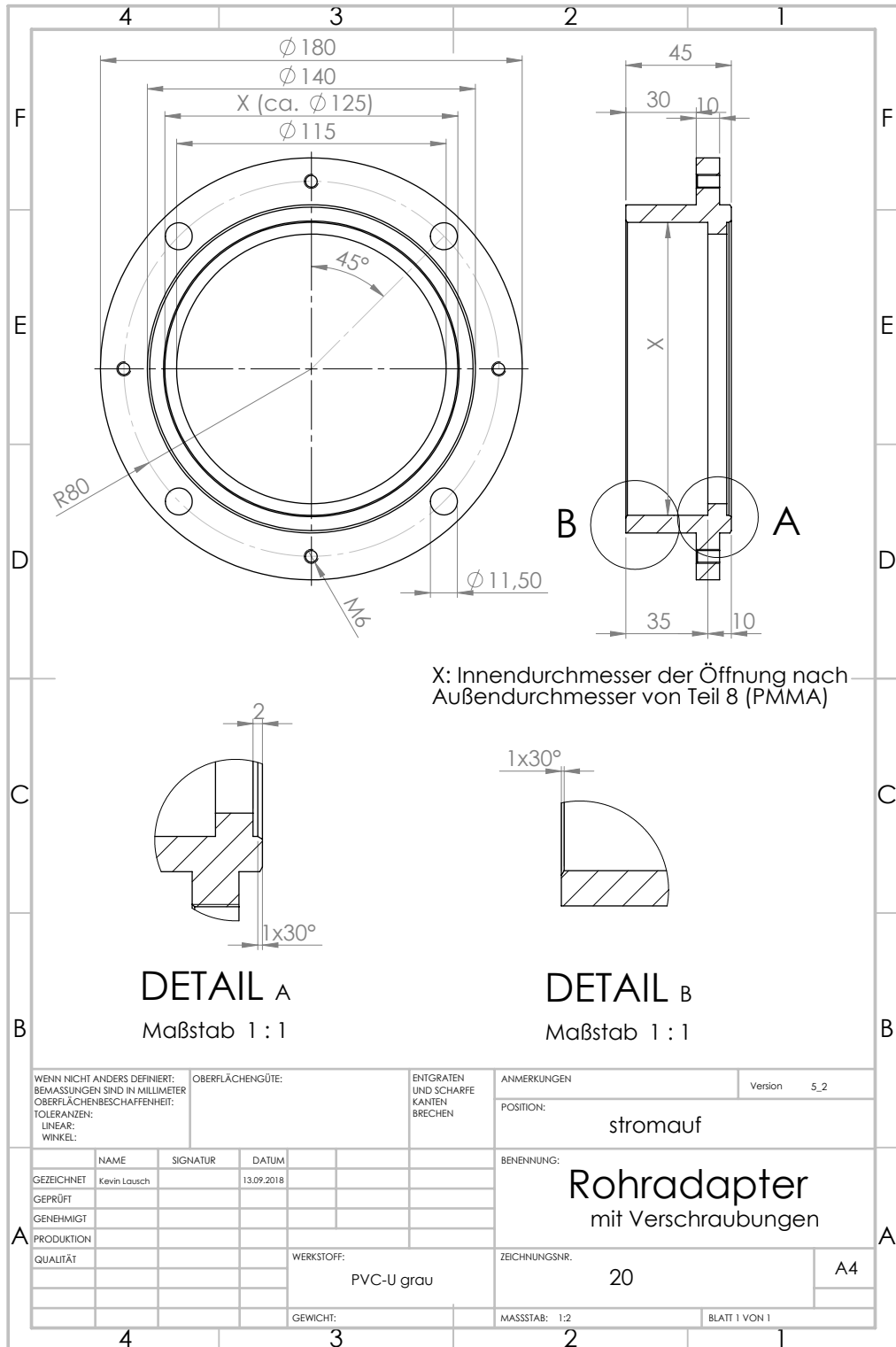


Figure A.14: Technical drawing of the removable, central pipe adapter for the test rig at the HFI water laboratory

# **Appendix B**

## **Illustrations of the Test Rigs**

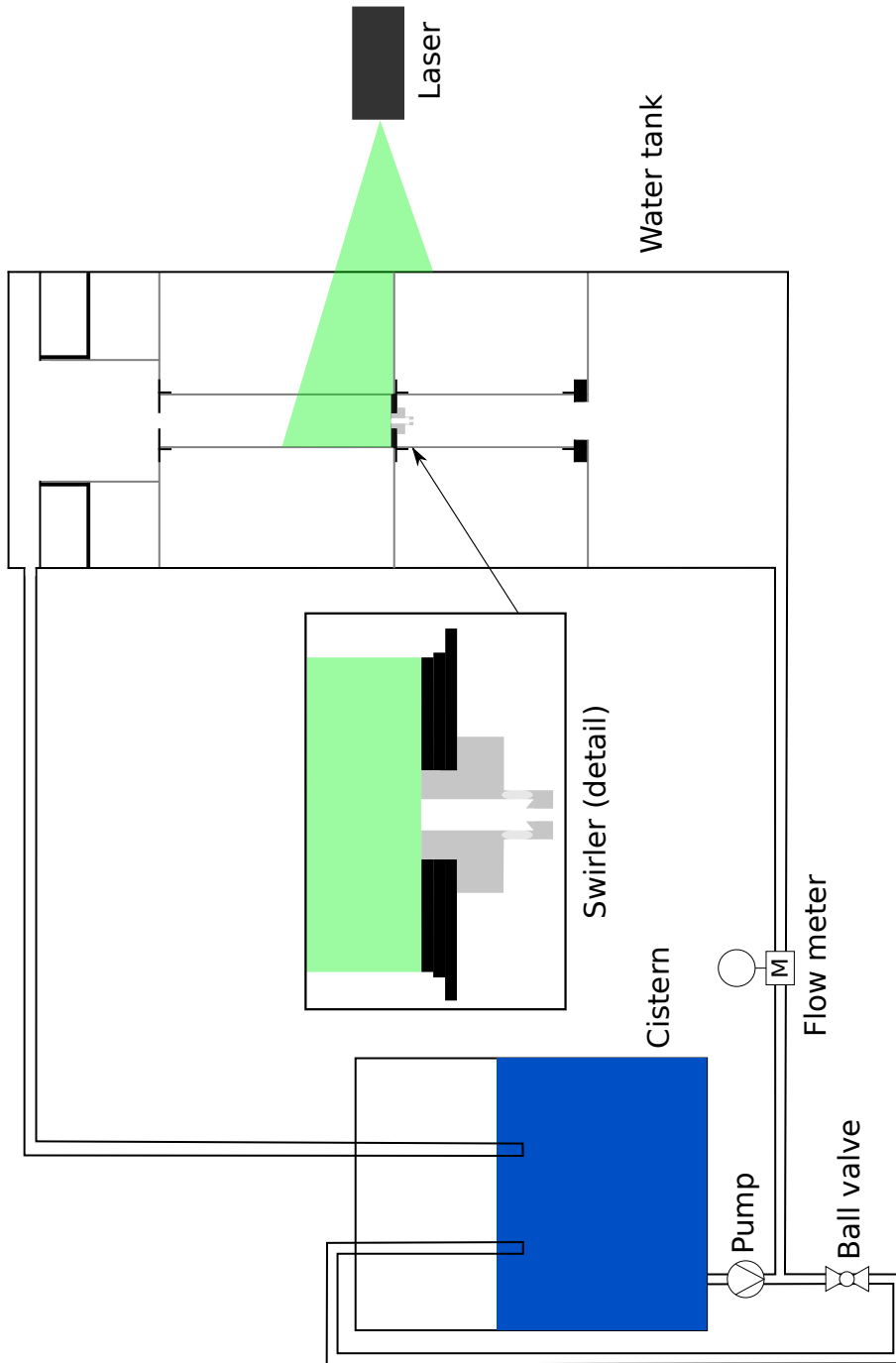


Figure B.1: Simplified illustration of the test rig at the HFI water laboratory

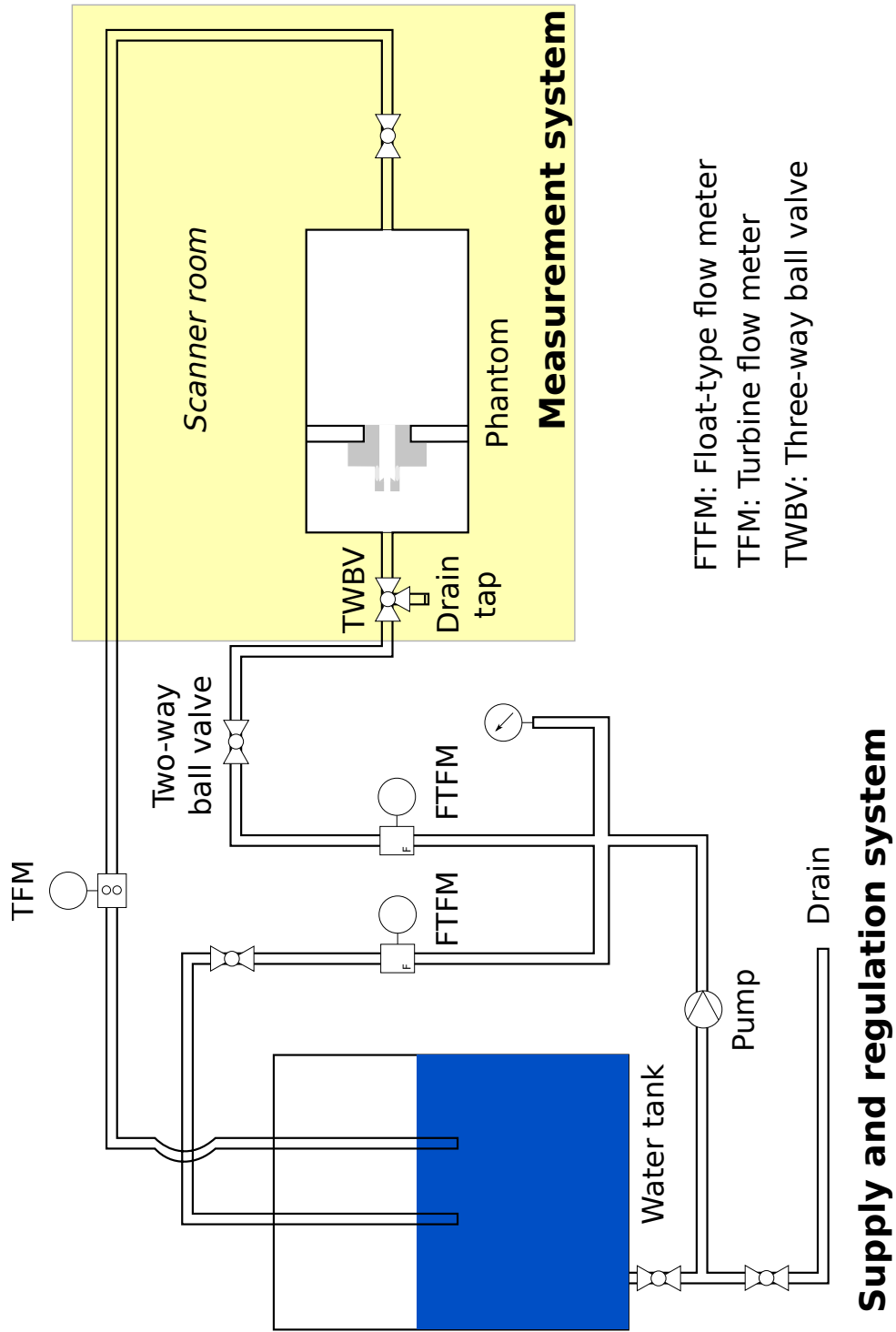


Figure B.2: Simplified illustration of the test rig at the facilities of the PTB

# **Appendix C**

## **Additional MRV parameters**

	dj0_br575_20000, axial velocity, coronal plane	dj0_br575_20000, axial velocity, transverse plane	dj0_br575_20000, transverse velocity, coronal plane	dj0_br575_20000, transverse velocity, transverse plane
TE in ms	4.91	5.05	4.98	5.05
2 TR in ms	15	16	15	16
Matrix Size	512 × 160	512 × 160	512 × 160	512 × 160
Flip angle	12°	12°	12°	12°
TA in min	approx. 42	approx. 42	approx. 42	approx. 42
Bandwidth in $\frac{\text{Hz}}{\text{px}}$	440	440	440	440

Table C.1: MRV acquisition parameters for the axial and transverse velocity fields of the swirling flow without injector jet

	dj96_br575_20000, axial velocity, coronal plane	dj96_br575_20000, axial velocity, transverse plane	dj96_br575_20000, transverse velocity, coronal plane	dj96_br575_20000, transverse velocity, transverse plane
TE in ms	4.91	4.87	4.98	4.91
2 TR in ms	16	15	16	16
Matrix Size	512 × 160	512 × 160	512 × 160	512 × 160
Flip angle	12°	12°	12°	12°
TA in min	approx. 42	approx. 5	approx. 42	approx. 1
Bandwidth in $\frac{\text{Hz}}{\text{px}}$	440	440	440	440

Table C.2: MRV acquisition parameters for the axial and transverse velocity fields of the swirling flow with injector jet

	dj96_brInf_10000, axial velocity, coronal plane	dj96_brInf_10000, axial velocity, transverse plane	dj96_brInf_10000, transverse velocity, coronal plane
TE in ms	4.87	5.04	4.87
2 TR in ms	15	16	15
Matrix Size	512 × 160	512 × 160	512 × 160
Flip angle	12°	12°	12°
TA in min	approx. 42	approx. 4	approx. 42
Bandwidth in $\frac{\text{Hz}}{\text{px}}$	440	440	440

Table C.3: MRV acquisition parameters for the axial and transverse velocity fields of the sole injector jet

	dj0_br575_20000, through-plane velocity, coronal plane	dj96_br575_20000, through-plane velocity, coronal plane
TE in ms	4.87	4.87
2 TR in ms	15	15
Matrix Size	512 × 160	512 × 160
Flip angle	12°	12°
TA in min	approx. 42	approx. 42
Bandwidth in $\frac{\text{Hz}}{\text{px}}$	440	440

Table C.4: MRV acquisition parameters for the through-plane velocity fields of the swirling flow with and without injector jet

	dj0_br575_20000, axial velocity, 12 planes with differing angles of rotation $\phi$	dj0_br575_20000, radial velocity, 12 planes with differing angles of rotation $\phi$	dj0_br575_20000, azimuthal velocity, 12 planes with differing angles of rotation $\phi$
TE in ms	4.91	4.98	4.87
2 TR in ms	15	15	15
Matrix Size	512 × 160	512 × 160	512 × 160
Flip angle	12°	12°	12°
TA in min	approx. 50	approx. 51	approx. 50
Bandwidth in $\frac{\text{Hz}}{\text{px}}$	440	440	440

Table C.5: MRV acquisition parameters for the three velocity component fields used for the global LSA base flow

